Modelling tyre noise for unpleasantness evaluation

Bharath Anantharamaiah

▶ **To cite this version:**

Bharath Anantharamaiah. Modelling tyre noise for unpleasantness evaluation. Acoustics [physics.class-ph]. INSA de Lyon, 2022. English. NNT : 2022ISAL0081 . tel-04149401

HAL Id: tel-04149401
https://theses.hal.science/tel-04149401

Submitted on 3 Jul 2023

HAL is a multi-disciplinary open access archive for the deposit and dissemination of scientific research documents, whether they are published or not. The documents may come from teaching and research institutions in France or abroad, or from public or private research centers.

L'archive ouverte pluridisciplinaire **HAL**, est destinée au dépôt et à la diffusion de documents scientifiques de niveau recherche, publiés ou non, émanant des établissements d'enseignement et de recherche français ou étrangers, des laboratoires publics ou privés.

N°d'ordre NNT : 2022ISAL0081

THESE de DOCTORAT DE L'INSA LYON
membre de l'Université de Lyon

École Doctorale ED 162
MEGA (Mécanique, Energétique, Génie Civil, Acoustique)

Spécialité/ discipline de doctorat : Acoustique

Soutenue publiquement le 04/10/2022, par :
Bharath Anantharamaiah

Modelling Tyre Noise for Unpleasantness Evaluation

Devant le jury composé de :

Totaro, Nicolas, Professeur, INSA Lyon	Président.e
Garcia, Juan, Docteur, Applus IDIADA	Rapporteur
Lopez Arteaga, Ines, Professor, Eindhoven Univ. Of Technology	Examinatrice
Kropp, Wolfgang, Professeur, Chalmers Univ. of Technology	Examinateur
Totaro, Nicolas, Professeur, INSA Lyon	Examinateur
Parizet, Etienne, Professeur, INSA Lyon	Directeur de thèse

Cette thèse est accessible à l'adresse : https://theses.insa-lyon.fr/publication/2022ISAL0081/these.pdf
© [B. Anantharamaiah], [2022], INSA Lyon, tous droits réservés

Cette thèse est accessible à l'adresse : https://theses.insa-lyon.fr/publication/2022ISAL0081/these.pdf
© [B. Anantharamaiah], [2022], INSA Lyon, tous droits réservés

Département FEDORA – INSA Lyon - Ecoles Doctorales

SIGLE	ECOLE DOCTORALE	NOM ET COORDONNEES DU RESPONSABLE
CHIMIE	**CHIMIE DE LYON** **https://www.edchimie-lyon.fr** Sec. : Renée EL MELHEM Bât. Blaise PASCAL, 3e étage secretariat@edchimie-lyon.fr	**M. Stéphane DANIELE** C2P2-CPE LYON-UMR 5265 Bâtiment F308, BP 2077 43 Boulevard du 11 novembre 1918 69616 Villeurbanne **directeur@edchimie-lyon.fr**
E.E.A.	**ÉLECTRONIQUE, ÉLECTROTECHNIQUE, AUTOMATIQUE** **https://edeea.universite-lyon.fr** Sec. : Stéphanie CAUVIN Bâtiment Direction INSA Lyon Tél : 04.72.43.71.70 secretariat.edeea@insa-lyon.fr	**M. Philippe DELACHARTRE** INSA LYON Laboratoire CREATIS Bâtiment Blaise Pascal, 7 avenue Jean Capelle 69621 Villeurbanne CEDEX Tél : 04.72.43.88.63 **philippe.delachartre@insa-lyon.fr**
E2M2	**ÉVOLUTION, ÉCOSYSTÈME, MICROBIOLOGIE, MODÉLISATION** **http://e2m2.universite-lyon.fr** Sec. : Bénédicte LANZA Bât. Atrium, UCB Lyon 1 Tél : 04.72.44.83.62 secretariat.e2m2@univ-lyon1.fr	**Mme Sandrine CHARLES** Université Claude Bernard Lyon 1 UFR Biosciences Bâtiment Mendel 43, boulevard du 11 Novembre 1918 69622 Villeurbanne CEDEX **sandrine.charles@univ-lyon1.fr**
EDISS	**INTERDISCIPLINAIRE SCIENCES-SANTÉ** **http://ediss.universite-lyon.fr** Sec. : Bénédicte LANZA Bât. Atrium, UCB Lyon 1 Tél : 04.72.44.83.62 secretariat.ediss@univ-lyon1.fr	**Mme Sylvie RICARD-BLUM** Institut de Chimie et Biochimie Moléculaires et Supramoléculaires (ICBMS) - UMR 5246 CNRS - Université Lyon 1 Bâtiment Raulin - 2ème étage Nord 43 Boulevard du 11 novembre 1918 69622 Villeurbanne Cedex Tél : +33(0)4 72 44 82 32 **sylvie.ricard-blum@univ-lyon1.fr**
INFOMATHS	**INFORMATIQUE ET MATHÉMATIQUES** **http://edinfomaths.universite-lyon.fr** Sec. : Renée EL MELHEM Bât. Blaise PASCAL, 3e étage Tél : 04.72.43.80.46 infomaths@univ-lyon1.fr	**M. Hamamache KHEDDOUCI** Université Claude Bernard Lyon 1 Bât. Nautibus 43, Boulevard du 11 novembre 1918 69 622 Villeurbanne Cedex France Tél : 04.72.44.83.69 **hamamache.kheddouci@univ-lyon1.fr**
Matériaux	**MATÉRIAUX DE LYON** **http://ed34.universite-lyon.fr** Sec. : Yann DE ORDENANA Tél : 04.72.18.62.44 yann.de-ordenana@ec-lyon.fr	**M. Stéphane BENAYOUN** Ecole Centrale de Lyon Laboratoire LTDS 36 avenue Guy de Collongue 69134 Ecully CEDEX Tél : 04.72.18.64.37 **stephane.benayoun@ec-lyon.fr**
MEGA	**MÉCANIQUE, ÉNERGÉTIQUE, GÉNIE CIVIL, ACOUSTIQUE** **http://edmega.universite-lyon.fr** Sec. : Stéphanie CAUVIN Tél : 04.72.43.71.70 Bâtiment Direction INSA Lyon mega@insa-lyon.fr	**M. Jocelyn BONJOUR** INSA Lyon Laboratoire CETHIL Bâtiment Sadi-Carnot 9, rue de la Physique 69621 Villeurbanne CEDEX **jocelyn.bonjour@insa-lyon.fr**
ScSo	**ScSo*** **https://edsciencessociales.universite-lyon.fr** Sec. : Mélina FAVETON INSA : J.Y. TOUSSAINT Tél : 04.78.69.77.79 melina.faveton@univ-lyon2.fr	**M. Christian MONTES** Université Lumière Lyon 2 86 Rue Pasteur 69365 Lyon CEDEX 07 **christian.montes@univ-lyon2.fr**

*ScSo : Histoire, Géographie, Aménagement, Urbanisme, Archéologie, Science politique, Sociologie, Anthropologie

Cette thèse est accessible à l'adresse : https://theses.insa-lyon.fr/publication/2022ISAL0081/these.pdf
© [B. Anantharamaiah], [2022], INSA Lyon, tous droits réservés

Cette thèse est accessible à l'adresse : https://theses.insa-lyon.fr/publication/2022ISAL0081/these.pdf
© [B. Anantharamaiah], [2022], INSA Lyon, tous droits réservés

Acknowledgments

The author gratefully acknowledges the European Commission for its support of the Marie Sklodowska Curie program through the ETN PBNv2 project (GA721615).
The author is deeply grateful to INSA Lyon team, my Ph.D. supervisor Prof. Etienne Parizet, Prof. Antoni Jerome, Dr. Nicolas Totaro, my colleagues Mr. Giorgio Pulverenti and Mr. Emmanuel Dabankah at INSA Lyon and other consortium colleagues.
The author thanks Applus IDIADA group, especially Dr. Juan J. Garcia for his internal supervision and Mr. Francesc Xavier Montane, Mr. Joan Puig, Mr. Roger Mateu Cabre and Ms. Ines Lama Borrajo for their constant support.
The author would also like to express his gratitude to Dr. Angels Aragones, Dr. Tomas Bouda, Mr. Angel Sanchez, Mr. Jordi Arbiol, Mr. Cristobal Garcia, Mr. Carlos Fidalgo, Mr. Felix Gonzalez, Mr. Onno Olaf de Boer, Mr. Pierre Thibaudeau, Mr. Imanol Laraudogoitia, Mr. Jaume Sonet, Mr. Alphonso Vera, Mr. Ruben Fabregat, Mr. Oriol Calvo and all the colleagues of Design Engineering, NVH and Vehicle dynamics department at Applus IDIADA for their support during the work.
Swami Mangalanathananda and Swami Raghuramananda of Ramakrishna Mission, Bengaluru have left a strong impact on the author's emotional strength and mindfulness, for which the author is immensely grateful.
Prof. K. Gopalakrishna and Prof. K. Ramanarasimha are acknowledged here for the ignition they induced in the author's career to pursue engineering based studies.
The author acknowledges the support from friends - Natalia Kaminsaka, Anusha Srihari Arva, Piotr Balik, Karthik Suresh and Shishir Mysore during the course of the work.

Cette thèse est accessible à l'adresse : https://theses.insa-lyon.fr/publication/2022ISAL0081/these.pdf
© [B. Anantharamaiah], [2022], INSA Lyon, tous droits réservés

Cette thèse est accessible à l'adresse : https://theses.insa-lyon.fr/publication/2022ISAL0081/these.pdf
© [B. Anantharamaiah], [2022], INSA Lyon, tous droits réservés

Dedicated to my parents and sister who have been my strength during the course of my studies.

ನನ್ನ ಈ ಸಂಶೋಧನೆಯನ್ನು ಮೈಸೂರು ಸಂಸ್ಥಾನಕ್ಕೆ, ಅವರು ಬೆಳೆಸಿದ ಅನೇಕ ತಂತ್ರಜ್ಞರಿಗೆ ಹಾಗು ವಾಸ್ತುಶಿಲ್ಪಿಕಾರರಿಗೆ ಮುಡಿಪಾಗಿ ಇಡಲು ಇಚ್ಛಿಸುತ್ತೇನೆ. ಇಡೀ ಭಾರತ ಕಂಡ ಅತ್ಯದ್ಭುತ ಹಾಗು ಧೀಮಂತ ಅಭಿಯಂತರರಾದ ಸರ್ ಎಂ. ವಿಶ್ವೇಶ್ವರಯ್ಯನವರು ನನಗೆ ಸದಾ ಸ್ಫೂರ್ತಿಯಾಗಿರುತ್ತಾರೆ. ಮೈಸೂರು ರಾಜಮನೆತನ ಇಲ್ಲದಿದ್ದಲ್ಲಿ ಈಗ ಕಂಡಿರುವ ಏಳಿಗೆ ಹಾಗು ಸರ್ ಎಂ. ವಿ ಮತ್ತು ಸರ್ ಮಿರ್ಜಾ ಇಸ್ಮಾಯಿಲ್ ಅಂತವರ ಕೊಡುಗೆಗಳನ್ನು ಬಹುಶಃ ಬೆಂಗಳೂರು ಮತ್ತು ಕರ್ನಾಟಕ ರಾಜ್ಯ ಕಂಡಿರುತ್ತಿರಲಿಲ್ಲ.

स्वगृहे पूज्यते पितरः, स्वग्रामे पूज्यते प्रभुः,
स्वराज्ये पूज्यते राजा, विद्वान् सर्वत्र पूज्यते।

Parents are respected in their house, a God/leader is respected in a community/group, a king is respected in his kingdom, but a learned one is respected everywhere.
- Chanakya, philosopher, economist and a political advisor, 375 - 283 B.C.E

Learn everything that is good from others but bring it in, and in your own way to absorb it; do not become others. You cannot believe in God until you believe in yourself.
- Swami Vivekananda, monk and a philosopher, 19. century

Cette thèse est accessible à l'adresse : https://theses.insa-lyon.fr/publication/2022ISAL0081/these.pdf
© [B. Anantharamaiah], [2022], INSA Lyon, tous droits réservés

Cette thèse est accessible à l'adresse : https://theses.insa-lyon.fr/publication/2022ISAL0081/these.pdf
© [B. Anantharamaiah], [2022], INSA Lyon, tous droits réservés

Résumé

Dans une automobile, le bruit est généré par divers composants tels que le moteur, la transmission, l'échappement, les pneus, l'aérodynamique, etc. Tous ces bruits contribuent collectivement au bruit de passage (PBN) et participent à la gêne sonore en milieu urbain.
Les véhicules électriques ont radicalement modifié la situation. Dans ces voitures, le bruit du moteur est presque inexistant. Le bruit aérodynamique étant très faible à basse vitesse (moins de 70 km/h), les pneus sont la principale source de désagrément en milieu urbain. Bien que plusieurs travaux aient été menés sur le bruit des pneus, il n'existe aucune étude déterministe sur sa conception efficace, en particulier sur sa perception acoustique en ce qui concerne son caractère désagréable.
Pour relever ce défi, l'objectif principal de ce travail est d'explorer les facteurs qui influencent le bruit généré par les pneus, en particulier son caractère désagréable, afin d'améliorer la perception acoustique d'une voiture à basse vitesse. Le principal résultat de ce travail est le développement d'un outil de simulation ou d'éléments finis (FE) qui permet de prédire le bruit généré par les pneus et la perception de son caractère désagréable. Cela permet de tirer parti du bruit des pneus pour améliorer la sécurité des piétons, en particulier lorsqu'il provient d'un véhicule qui passe à une vitesse relativement faible.
Le processus de développement du modèle FE du pneu présenté dans ce travail comprend la caractérisation du caoutchouc du pneu et des matériaux des couches. Ces propriétés sont utilisées dans les simulations pour modéliser le comportement statique et dynamique du pneu. Ces simulations permettent de déterminer les fonctions de transfert du bruit (NTF), et donc les réponses impulsionnelles (IR), dues à l'impact sur les bandes de roulement au niveau de l'aire de contact pneu/route. Les forces de roulement sur chaque bande de roulement d'un pneu roulant sont déterminées et convoluées avec les réponses impulsionnelles correspondantes. Celles-ci sont ensuite concaténées pour développer le bruit de roulement du pneu pour différentes pressions de gonflage et vitesses de roulement. La puissance spectrale moyenne des bandes d'un tiers d'octave des fichiers audio/bruit générés sont corrélées avec celles des tests. Enfin, les fichiers audios du bruit de roulement simulé et des tests sont soumis à des tests d'écoute pour évaluer leur caractère désagréable. Les résultats ont confirmé la bonne fiabilité et sensibilité de l'outil FE développé dans ce travail pour le changement du caractère désagréable du bruit dû aux variations de la vitesse des pneus. Cependant, ils n'ont pas été concluants pour les différentes pressions de gonflage du pneu.

Mots clés: bruit des pneumatiques, pass-by noise (PBN), psychoacoustique des bruit des pneumatiques, Simulation en éléments finis (FE) des bruits des pneumatiques, véhicules électriques (EVs).

Cette thèse est accessible à l'adresse : https://theses.insa-lyon.fr/publication/2022ISAL0081/these.pdf
© [B. Anantharamaiah], [2022], INSA Lyon, tous droits réservés

Cette thèse est accessible à l'adresse : https://theses.insa-lyon.fr/publication/2022ISAL0081/these.pdf
© [B. Anantharamaiah], [2022], INSA Lyon, tous droits réservés

Abstract

Noise in an automotive is generated from various components such as engines, transmission, exhaust, tyres, aerodynamics, etc. All these noises collectively contribute to the pass-by noise (PBN) and contribute to noise annoyance in urban environments.
Electric vehicles have drastically modified the situation. In such cars, engine noise is nearly non-existent. As wind noise is very low at low speeds (below 70 km/h), tyres are the prominent source of unpleasantness in urban environments. Although several investigations have been made on tyre noise, there exist no deterministic studies over its efficient design, especially on its acoustic perception with respect to its unpleasantness.
For addressing this challenge, the main aim of the current work is to explore the factors that influence the noise generated by tyres, especially its unpleasantness, in order to enhance the perception of a car noise at low speeds. The major outcome of this work is to develop a simulation or finite element (FE) tool that allows the prediction of generated tyre noise and perception of its unpleasantness. This creates a pathway to leverage tyre noise for the enhancement of pedestrian safety, especially from a vehicle passing by at relatively low speeds.
The tyre FE model development process presented in this work includes tyre rubber and plies material characterisation. These properties are used in simulations to model tyre static and dynamic behaviour. From these simulations the noise transfer functions (NTFs), and thus impulse responses (IRs), due to impact on treads at tyre-road contact patch, are determined. Rolling forces on each tread of a rolling tyre are determined and convolved with corresponding impulse responses. Further, these are concatenated to develop tyre rolling noise for various tyre inflation pressures and rolling speeds. The average spectral power of the one-third octave bands of generated noise/audio files are correlated with those of tests. Finally, both test and simulated rolling audio files are subjected to listening tests to grade their unpleasantness. Results confirmed good reliability and sensitivity in the FE tool developed in this work for the change in unpleasantness in the noise due to variations in the tyre speeds. However, the same stood inconclusive for various inflation pressures of the tyre.

Keywords: Tyre noise, pass-by noise (PBN), tyre noise psychoacoustics, tyre noise FE simulation, electric vehicles (EVs)

Cette thèse est accessible à l'adresse : https://theses.insa-lyon.fr/publication/2022ISAL0081/these.pdf
© [B. Anantharamaiah], [2022], INSA Lyon, tous droits réservés

Cette thèse est accessible à l'adresse : https://theses.insa-lyon.fr/publication/2022ISAL0081/these.pdf
© [B. Anantharamaiah], [2022], INSA Lyon, tous droits réservés

Contents

Cette thèse est accessible à l'adresse : https://theses.insa-lyon.fr/publication/2022ISAL0081/these.pdf
© [B. Anantharamaiah], [2022], INSA Lyon, tous droits réservés

Cette thèse est accessible à l'adresse : https://theses.insa-lyon.fr/publication/2022ISAL0081/these.pdf
© [B. Anantharamaiah], [2022], INSA Lyon, tous droits réservés

Cette thèse est accessible à l'adresse : https://theses.insa-lyon.fr/publication/2022ISAL0081/these.pdf
© [B. Anantharamaiah], [2022], INSA Lyon, tous droits réservés

Cette thèse est accessible à l'adresse : https://theses.insa-lyon.fr/publication/2022ISAL0081/these.pdf
© [B. Anantharamaiah], [2022], INSA Lyon, tous droits réservés

List of Abbreviations

ABC: Absorbing boundary condition
BE: Boundary element
BEM: Boundary element method
ca.: Circa
dB: Decibel
DoE: Design of experiments
DMA: Dynamic mechanical analysis
EU: European Union
EV: Electric vehicle
FE: Finite element
FEM: Finite element method
FFT: Fast-Fourier transform
GM: Generalised Maxwell (model)
HyRoNE: Hybrid rolling noise estimation
IFE: Infinte element
IFFT: Inverse fast-Fourier transform
IN: Impact noise
IR: Impulse response
JND: Just noticeable differences
kph: Kilometer per hour
LHS: Latin hypercube sampling
LVA: Laboratoire Vibrations Acoustique de l'INSA Lyon
mm: millimeter
NTF: Noise transfer function
PBN: Pass-by noise
PDE: Partial differential equation
PI: Point inertance
PML: Perfectly matched layer
PSD: Power spectral density
RMS: Root mean square
SPERoN: Statistical physical explanation of rolling noise
SPL: Sound pressure level
SRC: Sommerfeld radiation condition
SSM: Static stiffness measurement
TI: Transfer inertance
WFEM: Waveguide finite element method

Cette thèse est accessible à l'adresse : https://theses.insa-lyon.fr/publication/2022ISAL0081/these.pdf
© [B. Anantharamaiah], [2022], INSA Lyon, tous droits réservés

Cette thèse est accessible à l'adresse : https://theses.insa-lyon.fr/publication/2022ISAL0081/these.pdf
© [B. Anantharamaiah], [2022], INSA Lyon, tous droits réservés

Introduction

A machine functions on the core principle of utilisation of energy and its dissipation in either the same or different forms. From energy perspective, an automotive or a car is no different from a machine. A car is powered by various sources such as gasoline, diesel, electric or other forms and dissipates energy in the form of motion, noise, heat etc. Noise from a car is subjected to perception from one's frame of reference, i.e. a car can be noisy for a person outside the car (or a pedestrian) and can be pleasant for a passenger inside the car at the same time and vice versa. The noise perceived by pedestrians is collectively called *exterior* noise or *Pass-by Noise* (PBN) and the noise perceived by a passenger inside a car is called *interior* noise. Exterior noise or PBN is collectively due to the engine, tyre-road interaction, exhaust noise, etc. The noise from air-conditioning (a/c) ducts, wind, tyres, etc. contribute to vehicle interior as well as exterior noise. Figure 1 shows various types of noise generated from a car, categorised by the source.

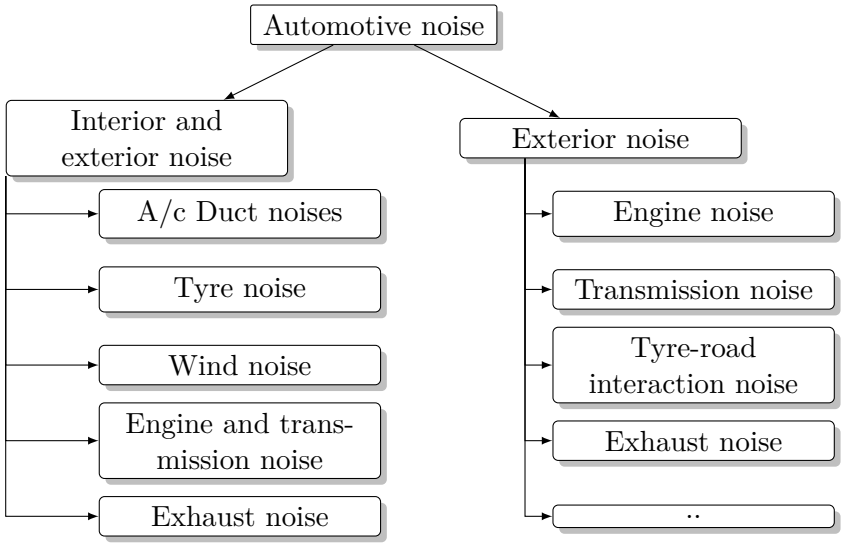

Figure 1: Types of vehicle noise.

Focusing on PBN, it was found that, for commercial passenger vehicles with a diesel or gasoline engine for instance, the engine (including exhaust), transmission and tyre noise contributed to a total of 85 dB (A-weighted), of which tyre-road interaction and the engine contribute to 41% and 42% of the overall noise, respectively [1]. Furthermore, it was observed that these percentages are not constant and changed with the speed of the car. At lower speeds, it was found that the engine noise exceeds the tyre-road interaction noise and vice versa at higher speeds [1].

Cette thèse est accessible à l'adresse : https://theses.insa-lyon.fr/publication/2022ISAL0081/these.pdf
© [B. Anantharamaiah], [2022], INSA Lyon, tous droits réservés

Upon extending the investigation further, it was observed that on increasing the mass of the tyre (by adding more rubber in the carcass of the tyre), the noise generated decreased by 5 dB approximately [2]. Apart from this investigation, Sandberg et. al [1] identified various tread patterns that yielded quiet summer and winter tyres. Based on these existing investigations, it can be seen that understanding the mechanism of noise generation from tyre-road interaction is a challenging task and is a domain that still needs to be vastly explored.

Motivation

With the set up of new and stringent EU regulations for permissible PBN from a car (UN/ECE R51.03), the automotive manufacturers are obliged to focus on the reduction in noise of their products. From the currently permitted (EU) PBN levels of a car, there is a proposal to reduce PBN at least by 3 dB by the year 2022 [3]. The permissible values of current and future PBN limits are shown in Table 1.

Table 1: Current and prospective permissible PBN limits for various categories of vehicles [3]. PMR refers to power-to-mass ratio (kW/kg) of a vehicle, P_n refers to its engine rated power (kW) and M refers to its mass (kg or ton).

Vehicle category	Condition	Limit (dB(A))		
		Phase 1 2016	Phase 2 2020	Phase 3 2024
M1	PMR $\leq$ 120	72	70	68
	120 $<$ PMR $\leq$ 160	73	71	69
	PMR $>$ 160	75	73	71
	PMR $>$ 200, $\leq$ 4 seats R-point height $<$ 450 mm	75	74	72
M2	M $\leq$ 2500 kg	72	70	69
	2500 kg $<$ M $\leq$ 3500 kg	74	72	71
	M $>$ 3500 kg ; $P_n \leq$ 135 kW	75	73	72
	M $>$ 3500 kg ; $P_n >$ 135 kW	75	74	72
M3	$P_n \leq$ 150 kW	76	74	73
	150 kW $< P_n \leq$ 250 kW	78	77	76
	$P_n >$ 250 kW	80	78	77
N1	M $\leq$ 2500 kg	72	71	69
	M $>$ 2500 kg	74	73	71
N2	$P_n \leq$ 135 kW	77	75	74
	$P_n >$ 135 kW	78	76	75
N3	$P_n \leq$ 150 kW	79	77	76
	150 kW $< P_n \leq$ 250 kW	81	79	77
	$P_n >$ 250 kW	82	81	79

With the incorporation of these regulations, newer cars would emerge out quieter not only at high speeds, but also at low speeds. This, however, poses a problem in city limits where the average car speed is around 30 kph to 50 kph. Since a car becomes noiseless, it remains stealthy for a pedestrian, thereby making them vulnerable to accidents. Furthermore, with the new generation electric vehicles (EVs) that use quiet electric motors, noise levels from them can be overlooked because tyre noise is considerably low at low speeds. The question that challenges and motivates this research is - can there be a car that is quieter at high speeds, such as an EV, yet detectable (but not annoying) at low speeds?
However, if this developmental process is followed based on the existing conventional methods, it will demand enormous economical and manufacturing potential only to arrive at an optimum

Cette thèse est accessible à l'adresse : https://theses.insa-lyon.fr/publication/2022ISAL0081/these.pdf
© [B. Anantharamaiah], [2022], INSA Lyon, tous droits réservés

functional tyre. In order to catch up with the pace of current tyre research and development process, it is absolutely necessary to digitise and discretise a tyre using commercially existing numerical softwares and perform the required developmental works. This method offers quicker and efficient solution than testing the tyre on prototypes. Additionally, if a tyre model is digitised, it can be further implemented not only in noise modelling but also for the analysis of tyre wear, thermal analyses etc. Also, once a digitisation methodology is successfully developed, it can be implemented for other tyre models and types, e.g. composite wheels etc.
In this work, the possibility of developing a tyre using numerical methods to understand the tyre parameters that influence its noise perception is studied. In this work, the tyre FE model is found to accurately model the tyre static and dynamic behaviour. Although, the model fairly predicts the noise of the tyre in the static condition, the correlation between the tyre rolling noise from tests and simulation, especially for the case of tyre rolling speeds is good. With this methodology, the tyre researchers can now rely on numerical models for the tyre research and development for faster results. The tyre manufacturers can now not only aim for a reduction in cost and time for their tyre product life cycle but also target for early market release, especially raising the overall tyre requirement standards in the market.

Research goal and objective

The locus of this work is to understand the material and structural factors contributing to tyre noise generation, its propagation and perception. As a first step, a comprehensive understanding of the tyre structure and its materials is necessary before diving into the domain of tyre noise.
One of the challenges in tyre numerical modelling is to obtain precise material properties of tyre components, i.e. rubbers, belts and plies. In this work, material properties have not been shared by the collaborating tyre manufacturer due to confidentiality. Hence, the first milestone is to estimate these, especially rubber hyperelasticities and viscoelasticities based on characteristic responses of the tyre. Tyre static responses are used to characterise rubber and ply hyperelasticities with the help of design of experiments (DoE) technique and a simplified tyre numerical model that is developed and employed throughout this work. Upon estimating these, tyre static responses from simulations are correlated with that from tests and the influence of these over tyre modal behaviour is studied.
With respect to tyre noise measurement up to 1 kHz in hemi-anechoic chamber, the tyre is loaded with a solid block to replicate the real-time tyre boundary condition as in case of a stationary car. This tyre is excited at several points *closer* to the tyre-road contact patch (and not at the contact patch due to complexity in the setup, which is described later). The corresponding point inertances (PI) in the modal test and the noise transfer functions (NTFs) between a microphone (placed at a pre-determined location) and the impacted treads in noise tests are measured.
On the simulation side, rubber viscoelasticities are determined using a theoretical loss-angle vs rubber hyperelasticity relationship that has been established in a confidential research carried out at IDIADA technical center. These properties, coupled with the rubber hyperelasticity, are used to model the tyre dynamic behaviour up to 1 kHz. In this process, the PIs and the NTF of the tyre (at a node which is at a distance corresponding to the microphone in tests) are determined by impacting the same treads that were impacted in the test. The results from simulation and test are compared with each other. Once it is made sure that these curves correlate with each other adequately, the impacts are then made over the tyre treads that are close to the contact patch in the FE model. The NTFs due to these impacts are determined and these are transformed into impulse responses (IR) using inverse fast-Fourier transform (IFFT) technique.
Next, the rolling forces on each tread are determined using simulations. These are convolved with the determined IRs to obtain the rolling IRs of each tread. As a penultimate step, these convolved responses are concatenated according to tread randomisation pattern which leads us

Cette thèse est accessible à l'adresse : https://theses.insa-lyon.fr/publication/2022ISAL0081/these.pdf
© [B. Anantharamaiah], [2022], INSA Lyon, tous droits réservés

to tyre rolling noise. Such noise files are developed for various tyre inflation pressures and rolling speeds, whose spectral power of one-third octave bands are correlated with the corresponding audio files from rolling tyre measurements.
Ultimately, both sets of audio files, i.e. simulated and measured, are used in listening tests in which 28 participants grade the unpleasantness in the noise signals. A statistical comparison of these gradings provides an insight on the efficiency of the developed numerical model to predict minor variations in tyre rolling noise with varying tyre pressures and rolling speeds. This developed model will act as a foundation to check if such tyre noise variations can be modelled numerically. Further, considering several design and operating complexities, the same model will offer a possibility to study the influence of tyre design on tyre rolling noise for the enhancement of pedestrian safety.

Outline of the research

This work is a multi-domain research. Hence, the chapters of the report have to be separated accordingly.
Chapter 1 provides insight into tyre modelling process. It provides information about tyre design, such as modelling in numerical solvers, definition of associated material properties along with existing techniques.
Chapter 2 discusses various tyre noise generation and propagation mechanisms. These include mechanical and aerodynamic mechanisms which can be segregated based on the frequency range of interest. It also shares information about the methods used in modelling noise propagation, especially boundary element (BE) and infinite element (IFE) methods.
Chapter 3 illustrates the methodology of hyperelasticity charaterisation that is used for the estimation of rubber and ply hyperelastic properties. It shares information on the development of a simplified and innovative tyre finite element (FE) model, its capability to predict static and dynamic responses and finally the establishment of a reliable noise propagation model.
Chapter 4 focuses on the viscoelasticity characterisation process of tyre rubbers and dynamic modelling of tyre up to 1 kHz. In this chapter, the influence of tyre internal pressure on tyre NTF is discussed.
Chapter 5 explains the methodology used for the modelling of tyre rolling noise from the NTFs determined from a statically loaded tyre. In this chapter, a psychoacoustic relationship, in terms of unpleasantness, is established between the rolling noise of a tyre and its inflation pressures and rolling speeds.
Finally, chapter 6 presents the results obtained and future developments that could be made for the tyre numerical model that is developed.

Cette thèse est accessible à l'adresse : https://theses.insa-lyon.fr/publication/2022ISAL0081/these.pdf
© [B. Anantharamaiah], [2022], INSA Lyon, tous droits réservés

1

Tyre construction and modelling

In this chapter, a fundamental background on understanding a tyre, its components and structure is provided. Since this work involves modelling of tyre noise, a thorough insight into existing tyre modelling techniques is provided along with their pros and cons. Following the discussion, a suitable method for this work is decided.

1.1 Pneumatic tyre - a complex structure

A tyre is a very complex structure than what it initially appears to be. A good tyre design is very important for the passenger ride comfort since the load of the car body acts directly on it. Design of modern tyres has seen constant evolution in terms techniques and materials, especially rubbers. Hence, the tyre structural design and associated materials need to be understood elaborately. A general construction of a *radial* tyre is shown in Figure 1.1.

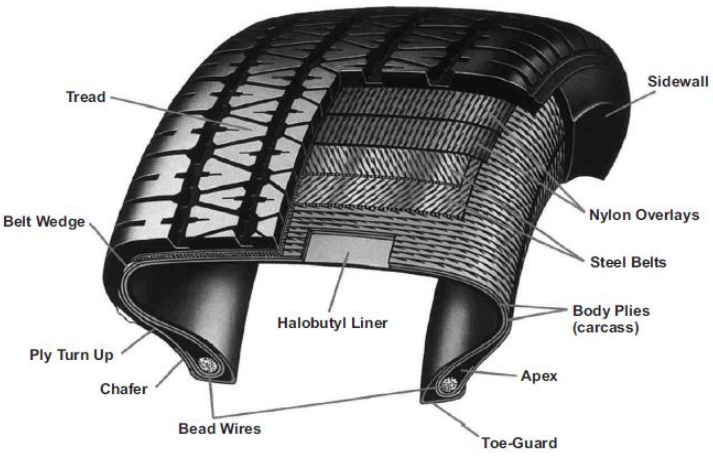

Figure 1.1: Parts of a pneumatic tyre. Taken from [4] as an example.

Treads form the outermost component of a tyre. Treads function as a contact between a road and the tyre at every instant of time providing traction for a vehicle. They also siphon away any materials, such as water, sand etc. to ensure that there is a constant grip of the tyre on the road. *Beads* form an important part of the tyre that ensures that the tyre fits firmly on a rim while also acting as a sealant in tubeless tyres. The layer below treads is collectively called the *carcass*. A tyre carcass consists of several reinforcements namely - *nylon overlays*, *steel belts* and *body plies*. Nylon overlays, also called ply caps, help in retaining the shape of the tyre radially against any centrifugal forces during high speed rolling. Steel belts offer protection for the tyre

Cette thèse est accessible à l'adresse : https://theses.insa-lyon.fr/publication/2022ISAL0081/these.pdf
© [B. Anantharamaiah], [2022], INSA Lyon, tous droits réservés

carcass against any damage due to wear and tear of the tyre. Body plies wrap the inner layers of the tyre from bead to bead thus offering an overall strength to the tyre skeleton. Based on the orientation of these plies, tyres can be classified mainly into two types:

- *Radial ply tyres* or simply radial tyres: In this type of tyres, plies orient radially from bead to bead and
- *Non-radial ply tyres*: In this type of tyres, plies either extend diagonally from bead to bead or can inter-twine at various angles.

Figure 1.2 shows radial and non radial tyre configurations. For more information about ply orientations, their advantages and disadvantages, the reader is referred to [4]. In this work, radial tyre configuration is explicitly considered. The *liner*, made of compounds of Butyl, forms the lowest layer of the tyre which holds the compressed air inside the tyre torus and assists in the tyre manufacturing process.

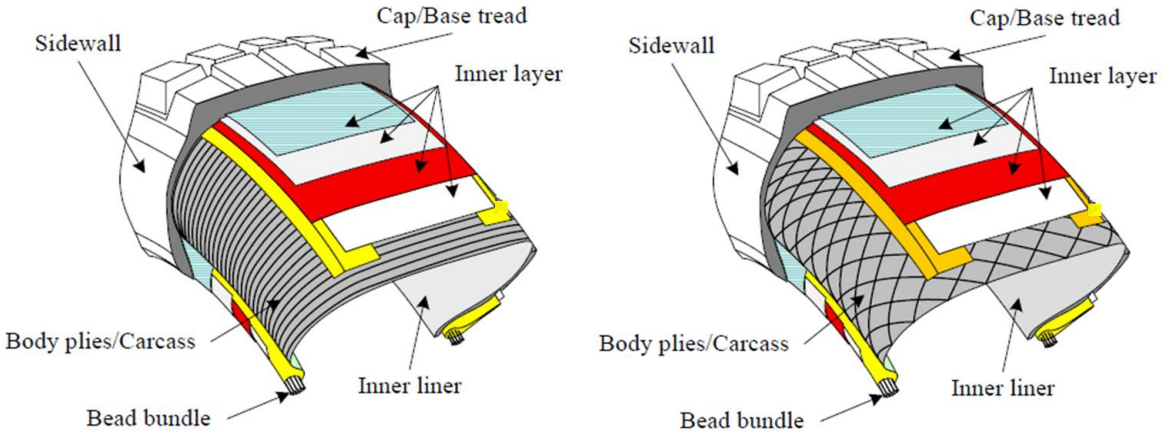

Figure 1.2: Types of tyre based on ply orientation. (a) Radial ply tyre and (b) Non-radial ply tyre. Taken from [5].

1.2 Standard designation of a tyre

The standard designation of a tyre is based on various parameters, such as the tyre section width W, tyre section height H, ply orientation etc. An illustration of these terms is shown in Figure 1.3. Additionally, a tyre is identified by its *aspect ratio*, defined as the ratio of section height to width

$$\text{Aspect ratio} = \frac{H}{W}. \tag{1.1}$$

Tyre used in this work has a designation of 205/55R16, where:

- 205: section width of the tyre in mm.
- 55: aspect ratio H/W in %.
- R: denotes that the specimen used is a radial tyre and
- 16: rim diameter.

Cette thèse est accessible à l'adresse : https://theses.insa-lyon.fr/publication/2022ISAL0081/these.pdf
© [B. Anantharamaiah], [2022], INSA Lyon, tous droits réservés

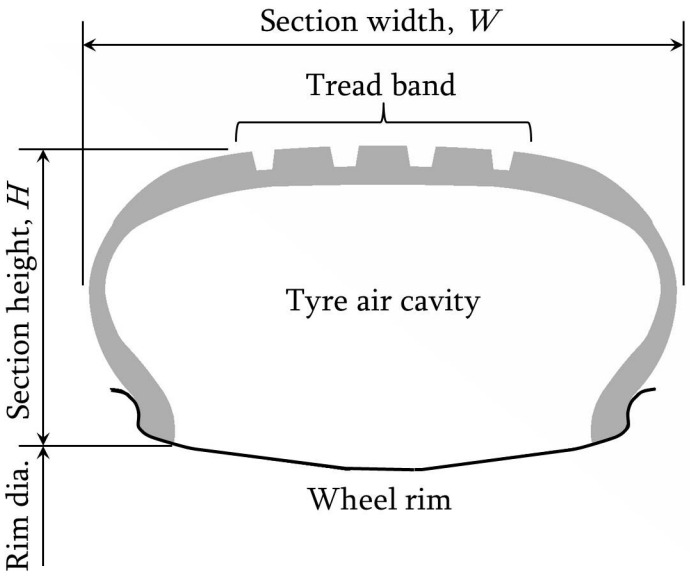

Figure 1.3: An illustration of the standard tyre designation.

1.3 Tyre materials and properties

Since a tyre is a sandwich of several components, it can be imagined as a cladding of various materials serving numerous purposes. The tyre components considered in this work can be distinguished into four categories based on the materials used, namely -

- Steel bead and reinforcements;
- Plies described by the Marlow model;
- Rubber described using the Yeoh model and
- Apex and chafer modelled using the Mooney-Rivlin model.

The above mentioned material types, except for bead and reinforcements, are variants of *hyperelasticity*.

1.3.1 Hyperelastic material models

From the basics of theory of continuum mechanics, the deformation gradient $\mathbf{F}$ and its Jacobian J are defined as [6]

$$F_{ij} = \delta_{ij} + \frac{\partial u_i}{\partial x_j}, \tag{1.2}$$

$$J = \det(\mathbf{F}), \tag{1.3}$$

where u_i is the deformation element subjected to a displacement field $u_i(x_k)$. The left Cauchy-Green deformation tensor $\mathbf{B}$ is defined as [6]

$$\mathbf{B} = \mathbf{F}.\mathbf{F}^T, \tag{1.4}$$

Cette thèse est accessible à l'adresse : https://theses.insa-lyon.fr/publication/2022ISAL0081/these.pdf
© [B. Anantharamaiah], [2022], INSA Lyon, tous droits réservés

comprising the set of invariants defined for incompressible materials as [7, 8]

$$\begin{aligned} \bar{I_1} &= \frac{B_{kk}}{J^{2/3}}, \\ \bar{I_2} &= \frac{1}{2}\left(\bar{I_1}^2 - \frac{B_{ik}B_{ki}}{J^{4/3}}\right), \\ \bar{I_3} &= \det\mathbf{B}, \end{aligned} \tag{1.5}$$

where

$$J = \sqrt{\det\mathbf{B}}. \tag{1.6}$$

The principle stretches for tensor $\mathbf{B}$ can be defined as

$$\lambda_1 = \sqrt{e_1},\ \lambda_2 = \sqrt{e_2} \text{ and } \lambda_3 = \sqrt{e_3}, \tag{1.7}$$

where e_1, e_2 and e_3 denote the three Eigenvalues of $\mathbf{B}$. Now, tensor $\mathbf{B}$ can be expressed as [6]

$$\mathbf{B} = \lambda_1^2\mathbf{b}^{(1)} \otimes \mathbf{b}^{(1)} + \lambda_2^2\mathbf{b}^{(2)} \otimes \mathbf{b}^{(2)} + \lambda_1^3\mathbf{b}^{(3)} \otimes \mathbf{b}^{(3)}, \tag{1.8}$$

where $\mathbf{b}^{(1)}$, $\mathbf{b}^{(2)}$ and $\mathbf{b}^{(3)}$ denote the unit Eigen vectors of $\mathbf{B}$ and operator $\otimes$ denotes their tensor multiplication. Various types of stresses in the body are given by [6]

$$n_i\sigma_{ij} = \lim_{dA\to 0}\frac{dP_j^{\mathbf{n}}}{dA}, \tag{1.9}$$

$$\boldsymbol{\tau} = J\boldsymbol{\sigma},\ \tau_{ij} = J\sigma_{ij}, \tag{1.10}$$

$$\mathbf{S} = J\mathbf{F}^{-1}.\boldsymbol{\sigma},\ S_{ij} = JF_{ik}^{-1}\sigma_{kj}, \tag{1.11}$$

$$\sum = J\mathbf{F}^{-1}.\boldsymbol{\sigma}.\mathbf{F}^{-T},\ \sum_{ij} = JF_{ik}^{-1}\sigma_{kl}F_{jl}^{-1}, \tag{1.12}$$

where Equations 1.9, 1.10, 1.11 and 1.12 represent the Cauchy true, the Kirchhoff, the first Piola-Kirchhoff and the second Piola-Kirchhoff stress tensors, respectively. The strain in hyperelastic materials is measured in terms of Strain energy density functions (W), given by [9]

$$W = W(\mathbf{F}) = W(\lambda_1, \lambda_2, \lambda_3) = W(I_1, I_2, I_3). \tag{1.13}$$

The stress in the body is calculated by

$$\sigma = \frac{2}{j}.\mathbf{B}.\frac{\partial W}{\partial \mathrm{B}} = \frac{1}{j}.\frac{\partial W}{\mathbf{F}}.\mathbf{F}^T, \tag{1.14}$$

where j is the component of Jacobian (refer Equation 1.6). An equivalent representation of Equation 1.13 is given by [9, 10]

$$W = \sum_{i+j=1}^{N} C_{ij}(I_1 - 3)^j + \sum_{i=1}^{N}\frac{1}{D_i}(J_{el} - 1)^{2i}, \tag{1.15}$$

where C_{ij}, D_i represent the temperature dependent material parameters, respectively and J_{el} represents the elastic volumetric strain. Equations 1.13 and 1.15 form the root equation for various material models used in tyres.

Marlow model

In the Marlow hyperelastic material model, the strain energy potential is independent of the second invariant. This is a simple model for which the strain energy density can be determined

Cette thèse est accessible à l'adresse : https://theses.insa-lyon.fr/publication/2022ISAL0081/these.pdf
© [B. Anantharamaiah], [2022], INSA Lyon, tous droits réservés

as [8]

$$W = \int_0^{\lambda_T - 1} \sigma(\varepsilon) d\varepsilon, \tag{1.16}$$

where $\sigma(\varepsilon)$ is the nominal uniaxial stress and λ_T respresents the uniaxial stretch. In this work, the Marlow hyperelasticity model is used to define the plies of the tyre.

Mooney-Rivlin model

Equation 1.15 is the most simplified form to define hyperelasticity and it manifests in various forms depending on the values of the number of coefficients N. The Mooney-Rivlin is a hyperelastic model where the strain density potential is a function of the first and the second strain invariants. Although this case has various forms [10], the most general form is derived when N bears the value of 1 and is represented as [10]

$$W = C_{10}(I_1 - 3) + C_{01}(I_2 - 3) + \frac{1}{D}(J_{el} - 1)^2. \tag{1.17}$$

The Mooney-Rivlin material model is used to define the tyre chafer and apex regions (refer Figure 1.1).

Yeoh model

The Yeoh model is a variant of Equation 1.15, in which the strain density function is dependent only on the first invariant of the strain and is defined as [11]

$$W = \sum_{i=1}^{N} C_{i0}(I_1 - 3)^j, \tag{1.18}$$

and the value of N is ideally infinite [11]. However, the higher the value of N, the higher is the computational time, since a large number of coefficients are added into the equation. The prescribed value of N is 3 for which there is higher accuracy in the results for large strain problems compared to equivalent models [12]. In this work, the Yeoh model is used for modelling all the other rubber components of the tyre that are not modelled either using Mooney-Rivlin or Marlow models.

1.3.2 Viscoelastic material model - Prony series

A material that has elasticity accompanied by the influence of viscosity is considered to be viscoelastic. A generalised description of viscoelasticity is described by a Maxwell element as shown in Figure 1.4.

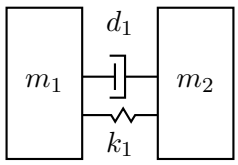

Figure 1.4: Spring-mass damper system to define a general viscoelastic material model.

In Figure 1.4, the spring defines the linear elastic model that can be expressed in terms of the standard Hook's law as

$$\boldsymbol{\sigma} = E.\boldsymbol{\varepsilon}, \tag{1.19}$$

Cette thèse est accessible à l'adresse : https://theses.insa-lyon.fr/publication/2022ISAL0081/these.pdf
© [B. Anantharamaiah], [2022], INSA Lyon, tous droits réservés

and the dashpot represents a viscous component that is defined from the basics of physics as

$$\boldsymbol{\sigma} = \eta . \frac{\partial \boldsymbol{\varepsilon}}{dt}, \tag{1.20}$$

where η is the viscous damping coefficient. Since viscoelasticity is time dependent, properties of a material are determined by two methods:

- Creep test: This is the test in which the material is made to undergo non-stop strain growth by applying a constant tensile force or stress. The material behaviour during the creep test can be described as [13]

$$\boldsymbol{\varepsilon}(t) = J(t)\boldsymbol{\sigma}_0, \tag{1.21}$$

  where $J(t)$ is the creep compliance function. It defines the quantity of material flow for applied instantaneous stress.

- Relaxation test: This is a test in which material strain is constant and the material undergoes gradual reduction in stress. The constitutive equation for describing the relaxation test is defined as [13]

$$\boldsymbol{\sigma}(t) = Y(t)\boldsymbol{\varepsilon}_0, \tag{1.22}$$

  where $Y(t)$ is defined as the relaxation function. For more information about these tests, the reader is refered to [14].

The relaxation function can be further determined from various series [14, 15]. In the current work, *Prony* series is used to model the relaxation function and is defined as [13]

$$Y(t) = E_0(1 - \sum_{i=1}^{n} p_i(1 - e^{-t/\tau_i})), \tag{1.23}$$

where p_i is defined as the Prony constant (i=1,2,...), τ_i is the Prony retardation constant (i= 1,2,..) and E_0 is the instantaneous material modulus. For further information about Prony series, the reader is refered to [13, 15, 14]. In the current work, all rubber materials are defined using hyperelasticity with viscoelasticity (as Prony series/parameters).

1.4 Existing tyre FE modelling techniques

Tyre modelling for its numerical analysis has been constantly upgraded over time. During the cradle stages of tyre analysis, the 2D models were used to model the tyres. Thanks to the advancements in numerical modelling, these 2D models were upgraded and today, complex 3D tyre models with detailed tread profiles are possible to be modelled. Figure 1.5 shows various tyre models available in the numerical FE world.

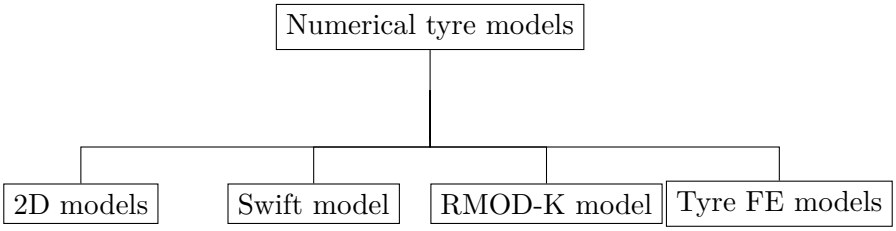

Figure 1.5: Currently existing numerical tyre models.

Cette thèse est accessible à l'adresse : https://theses.insa-lyon.fr/publication/2022ISAL0081/these.pdf
© [B. Anantharamaiah], [2022], INSA Lyon, tous droits réservés

1.4.1 2D tyre models

2D tyre models again have evolved over time according to the needs and requirements of the design process. Different varieties of 2D tyre models can be seen in Figure 1.6. The *point contact* and the *roller contact model* shown in Figure 1.6 consider only a single point of contact between the road and the tyre interface. Although it is very simple to calculate the interaction forces by these models, they will experience severe accelerations during cleat excitation. Hence these models cannot predict noise in high frequency domains [16]. (More information about high, low and mid frequency ranges during the tyre-road interaction are discussed in section 2.1.4).

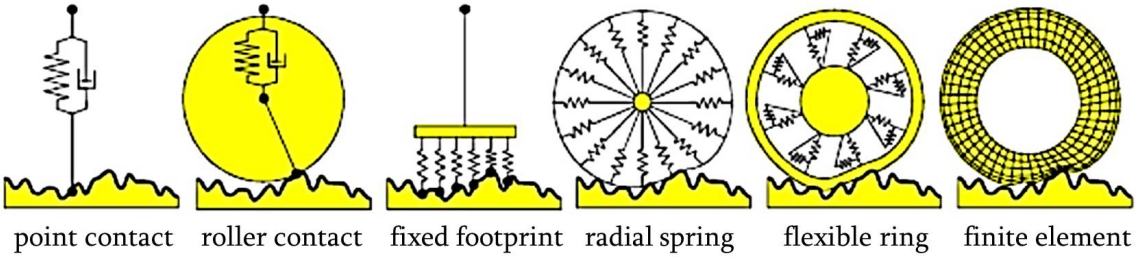

Figure 1.6: Various 2D tyre numerical models [17].

Fixed footprint model measures the irregularity over the surface by averaging the elevation measured by all the points considered along the foot print length. However, the irregularity is measured as the area beneath a flat surface rather than the tyre radius, i.e. this model cannot be used for the case of dynamic rolling of a tyre. In the models discussed till now, the mass of the tyre is concentrated at the centre and the tyre is free to go out of contact from the road surface [18]. *Radial* and *flexible ring model* use multiple spring systems pivoted at the centre of the wheel to measure the irregularities of the surface. The radial ring model consists of the carcass and the ply stiffness modelled as the spring stiffness [19]. The flexible ring model considers an additional elastic beam on its circumference that bears the carcass and the ply stiffness [20]. These models however, cannot incorporate tread profiles and other intricate details. Finite element is certainly an alternative to all these simplified models. This is because, from the fundamentals of finite element method (FEM), the higher the number of interaction points (nodes) at the tyre-road interface, the higher is the accuracy in the prediction of tyre behaviour.

1.4.2 Swift tyre model

Swift tyre model is an amalgamation of various concepts for the calculation of tyre forces and dynamics, namely:

- Magic tyre formula: that calculates the tyre forces and moments based on slip conditions;
- different contact slip equations, namely - longitudinal slip, side slip, turn slip and camber. For more information about these equations, the reader is referred to [21];
- Rigid ring: the tyre is modelled as two different rigid bodies coupled by springs and dampers. A free body description of the model is shown in Figure 1.7.
- Mechanism to overcome the road irregularities. For more information about design and construction of this mechanism, the reader is referred to [22].

The swift tyre model needs more data to be consolidated in order to define two rings of the tyre. Apart from this, the reliability of noise measurement is only up to 100 Hz [23]. Due to these reasons, swift tyre model is not considered in the current work.

Cette thèse est accessible à l'adresse : https://theses.insa-lyon.fr/publication/2022ISAL0081/these.pdf
© [B. Anantharamaiah], [2022], INSA Lyon, tous droits réservés

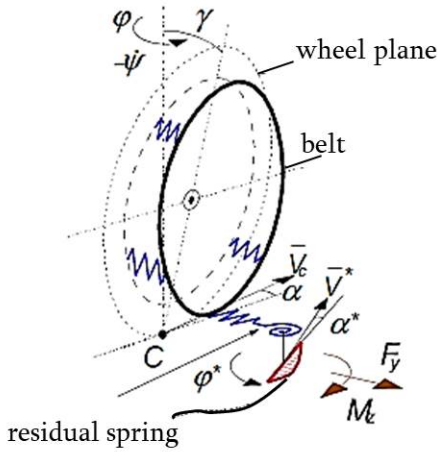

Figure 1.7: Functional swift tyre model. Image taken from [23].

1.4.3 RMOD-K model

RMOD-K model for a tyre is based on multibody dynamics in which tyre is modelled using a system of codes that define tangential contact and slip condition [24]. A representation of the above discussed models is shown in Figure 1.8. Based on the physics of the problem (refer Figure 1.8), available RMOD-K models can be classified into three types [24]:

- Steady state model in which the tyre is not discretized and only the tyre-road contact area is be determined;
- Models with contact area discretization that are used to calculate the static load and contact area shape without considering any rotation of the tyre and
- Models with discretization of the circumferential area that can be used to calculate transient forces and contact areas.

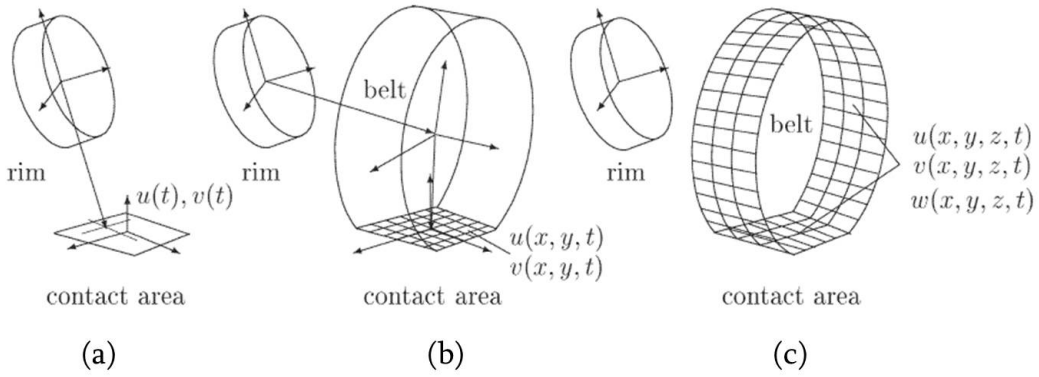

Figure 1.8: Various RMOD-K tyre models - (a) steady state model, (b) contact area discretization model and (c) transient model. Image taken from [24].

These models, however, do not include any information regarding tread depth, tread width etc. and hence cannot describe the exact phenomenon of tyre-road interaction. In order to overcome this drawback, an RMOD-K model with belt was designed as shown in Figure 1.9. This however has other disadvantage, i.e. the belt has to be modelled without considering other components of the tyre. Although the models described need low computational effort, they cannot predict

Cette thèse est accessible à l'adresse : https://theses.insa-lyon.fr/publication/2022ISAL0081/these.pdf
© [B. Anantharamaiah], [2022], INSA Lyon, tous droits réservés

noise due to tyre-road interaction in high frequency ranges [24]. Hence, due to these limitations, RMOD-K models cannot be used in the current work.

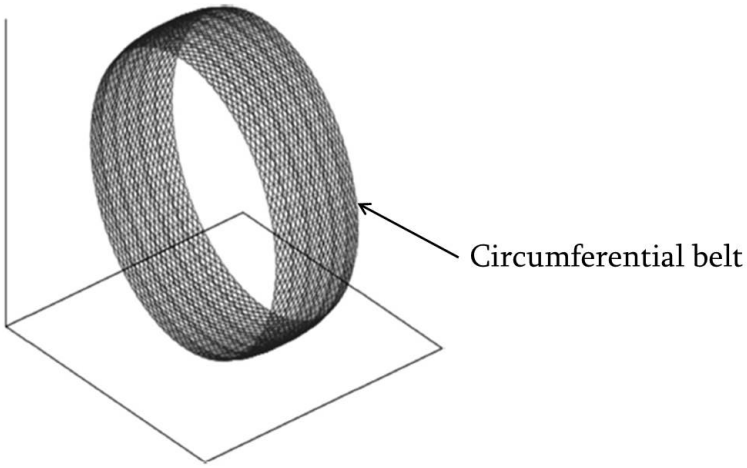

Figure 1.9: RMOD-K belt model. Image taken from [25].

1.4.4 Tyre FE models

With the advancement in numerical methods, FE modelling technique has proved to be an alternative to predict the performance of real world problems as every problem is modelled in the form of partial differential equations (PDEs) [26]. Before discussing about tyre FE models, it is necessary to get familiarised about various types of FE modelling procedures used in tyre modelling domain.
FEM discretizes a body (Ω_s) into smaller fragments generating nodes and elements, (refer Figure 1.10) and provides a systematic methodology for a computer program to arrive at a solution.

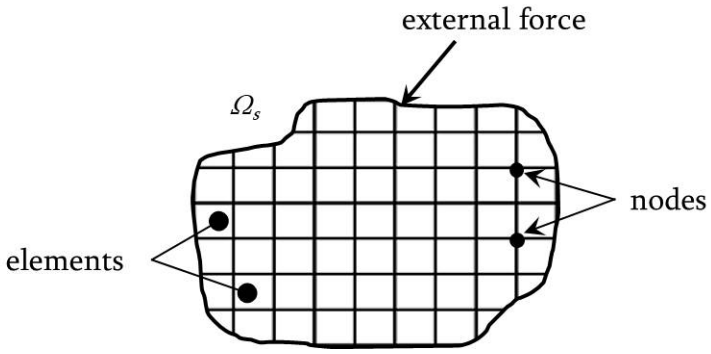

Figure 1.10: A sample surface discretized by FEs.

Any second order non-homogeneous physical system in equilibrium under d'Alembert's principle can be represented using an ordinary differential equation (ODE) as

$$\mathbf{M}\ddot{\boldsymbol{u}}(t) + \mathbf{C}\dot{\boldsymbol{u}}(t) + \mathbf{K}\boldsymbol{u}(t) = \mathbf{p}(t), \tag{1.24}$$

where $\mathbf{M}$, $\mathbf{C}$ and $\mathbf{K}$ are the mass, the damping and the stiffness matrices of the bodies in the system, respectively, $\mathbf{p}(t)$ is the instantaneous force acting on the bodies and $\boldsymbol{u}$ represents the displacements of the nodes of the elements. This is the basic modus operandi of an FEM. In Equation 1.24, it can be observed that the equation is a function of time, and the displacement

Cette thèse est accessible à l'adresse : https://theses.insa-lyon.fr/publication/2022ISAL0081/these.pdf
© [B. Anantharamaiah], [2022], INSA Lyon, tous droits réservés

$\boldsymbol{u}$ has to be calculated by time integration methods, which shall be discussed now. For more explicit information about theory behind the explanation, the reader is referred to [26].

Implicit method

In this method, element displacements are calculated for the time $t+\triangle t$ (where t represents the time step and $\triangle t$ represents the time increment) by approximating the derivatives as [26]

$$\dot{\boldsymbol{u}}(t+\triangle t) = \dot{\boldsymbol{u}}(t) + \frac{\triangle t}{2}\ddot{\boldsymbol{u}}(t) + \frac{\triangle t}{2}\ddot{\boldsymbol{u}}(t+\triangle t), \tag{1.25}$$

$$\dot{\boldsymbol{u}}(t+\triangle t) = \dot{\boldsymbol{u}}(t)\triangle t + \frac{\triangle t^2}{3}\ddot{\boldsymbol{u}}(t) + \frac{\triangle t^2}{6}\ddot{\boldsymbol{u}}(t+\triangle t). \tag{1.26}$$

Upon inserting Equations 1.25 and 1.26 in Equation 1.24 and simplifying, the equation of equilibrium can be expressed as

$$\left(\frac{6}{\triangle t^2}\mathbf{M} + \frac{3}{\triangle t}\mathbf{C} + \mathbf{K}\right)\boldsymbol{u}(t+\triangle t) = \mathbf{p}(t+\triangle t) + \mathbf{M}\left(\frac{6}{\triangle t^2}\boldsymbol{u}(t) + \frac{6}{\triangle t}\dot{\boldsymbol{u}}(t) + 2\ddot{\boldsymbol{u}}(t)\right) \tag{1.27}$$

The solution for the above equation is obtained by various iterative procedures. However, the computational effort increases with the increasing number of steps and hence, the implicit methodology is prescribed or preferable for the calculation of static problems. The sole advantage of the implicit algorithm is its numerical stability [26]. Many commercial software packages, e.g. Nastran, Optistruct, Abaqus etc. support implicit algorithm.

Explicit method

In explicit method, solver multiplies the state vector with mass matrices to iterate over from t to $t+\triangle t$, thus eliminating the calculation of solution at each step. This property makes the explicit method faster compared to the implicit method. With respect to numerical stability, the system of equation is stable if and only if the critical time step ($\triangle t_{crit}$) is smaller than the transit time of material waves through the smallest element of the FE model; this condition is described by the Courant criteria [26],

$$\triangle t < \triangle t_{crit} \approx (\frac{L_{crit}}{\mathrm{c}}), \tag{1.28}$$

where L_{crit} is the minimum element length of the discretized model and c is the maximum wave speed in the material, defined by

$$\mathrm{c} = \sqrt{\frac{\mathrm{E}}{\rho}}, \tag{1.29}$$

where E is the Young's modulus and ρ is the density of the material. Few commercially available solvers that support explicit algorithm are Pam-Crash, LS-Dyna, Abaqus/explicit etc. With currently available methodology, tyre-road FE modelling can be briefly categorised into three main types as shown in Figure 1.11. A general procedure for modelling tyres include:

- mounting;
- inflation;
- loading;
- testing.

Mounting involves assembling the rim and the tyre in the model. This means that the rotation of the rim by its axis also rotates the tyre. Upon mounting, the cavity inside the tyre torus

Cette thèse est accessible à l'adresse : https://theses.insa-lyon.fr/publication/2022ISAL0081/these.pdf
© [B. Anantharamaiah], [2022], INSA Lyon, tous droits réservés

is inflated by applying appropriate pressure. Loading of the tyre involves applying necessary (static) boundary conditions for studying the relevant tyre characteristics. Finally, further tests, such as rolling or impact tests are made on this loaded tyre. However, this procedure alters itself for different kinds of modelling techniques which shall be discussed now.

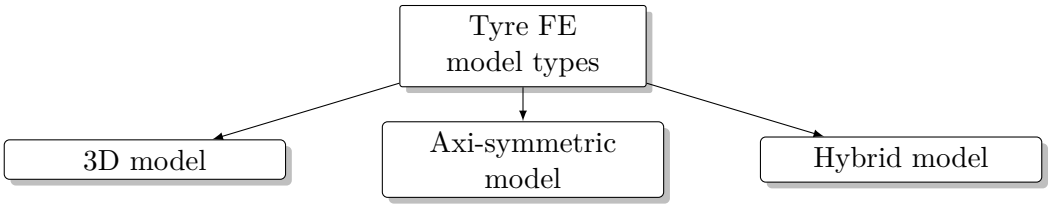

Figure 1.11: Existing tyre FE modelling techniques.

To model tyres using FE technique, researchers in past have considered several approaches. 3D modelling of tyres involves discretization of a solid tyre model using FE elements. In the past, few researchers [27, 28, 29] have used 3D FE models of tyre for analysing its performance. In these works, the general idea is to model a tyre using both implicit and explicit methods. Since mounting, inflation and loading steps do not involve advanced FE calculation, these process can be performed using implicit algorithm. The testing step is modelled using explicit method since the rolling of the tyre on a surface involves contact analysis which takes longer convergence times.
Axi-symmetric model (or just axi-model) is an alternative methodology to model the first three steps, i.e. mounting, inflation and loading [30, 31, 32]. It considers a 2D cross-section of a tyre and creates a 3D model by revolving the same to the required number of mesh densities along the vector of revolution. A typical procedure is illustrated in Figure 1.12.

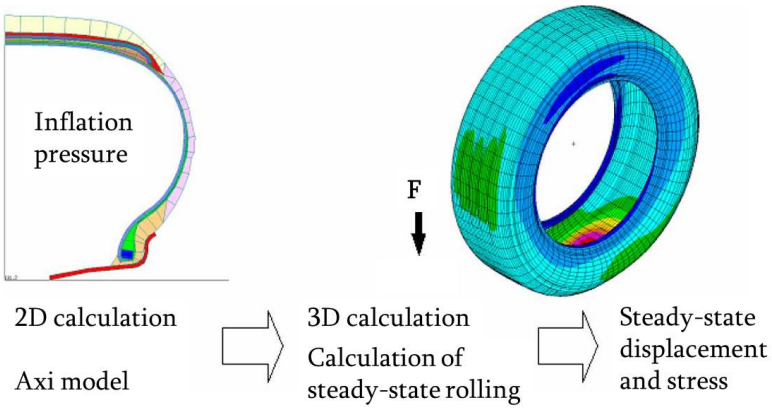

Figure 1.12: Modelling a full tyre from its axi-model. Image taken from [31].

For extensive evidence on the usage of axi-model in developing tyre numerical models, reader is refered to [31, 30, 32, 33]. Although this obviates the research community to use tyre axi-model in their work, the main drawback of this technique is that the axi-cross-section is incapable of modelling tread geometries. This is because the tread profiles are not uniform along the normal vector of axi-model revolution.
To overcome this drawback, in the year 2013, Korunovic et. al [34] modelled a tyre carcass and repeated cyclic pattern of tread using axi-modelling, independently. The two geometries were then coupled to form an actual model of a tyre and the model was a mixed Eulerian-Lagrangian* approach. The methodology is represented in Figure 1.13. This methodology can

*In Lagrangian method, the mesh rotates with the tyre surface. However in Eulerian approach, the mesh remains stationery while only the material inside the mesh rotates. This is achieved by varying the mass flow rate inside the mesh

Cette thèse est accessible à l'adresse : https://theses.insa-lyon.fr/publication/2022ISAL0081/these.pdf
© [B. Anantharamaiah], [2022], INSA Lyon, tous droits réservés

be categorised as a hybrid approach, as it does not compromise with the complexities of the tyre, yet simplifies the process of tyre modelling. Hybrid technique is useful because a tread profile can be separately developed by scanning the real tyre profile. This can be tied over the 3D tyre model that is generated by revolving the axi-model of the tyre cross-section. Hence in this work, hybrid modelling technique is used to develop the tyre FE model.

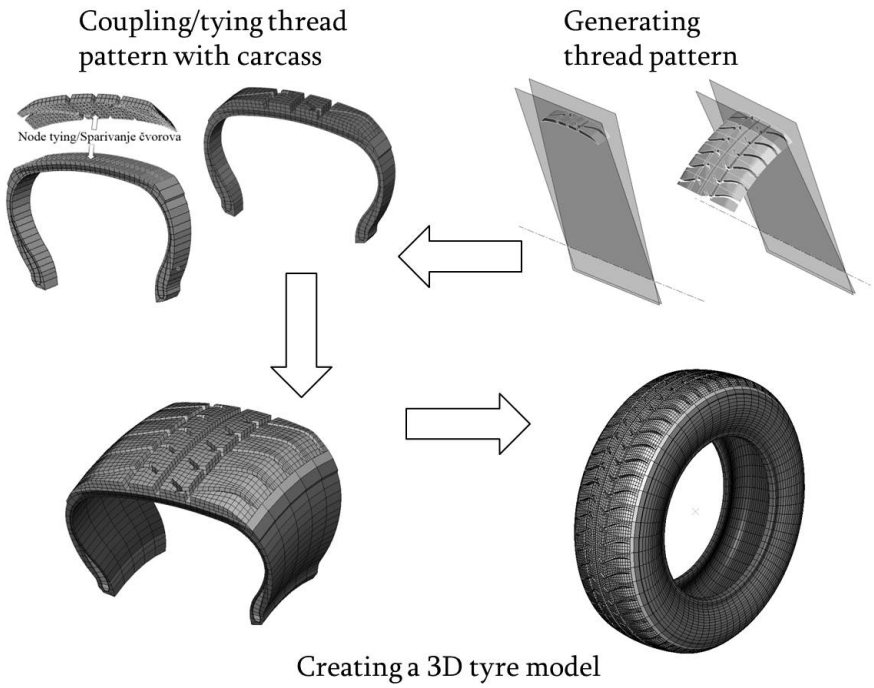

Figure 1.13: Modelling a hybrid tyre using axi-model. Image taken from [34].

Cette thèse est accessible à l'adresse : https://theses.insa-lyon.fr/publication/2022ISAL0081/these.pdf
© [B. Anantharamaiah], [2022], INSA Lyon, tous droits réservés

2

Tyre-road interaction, noise wave propagation and psychoacoustics

A tyre is a component that bears the complete weight of a car and transfers it to the ground. Also, it acts as a component that damps out any road imperfections to offer a comfortable ride. The previous chapter emphasized on the structure of a pneumatic tyre, its components, materials and numerical modelling. This chapter focuses on factors leading to tyre-road interaction, noise generation, propagation and perception.
When a tyre rolls over the surface of a road, tyre acts as an agent to dampen the transient loads that are generated at the tyre-road contact area. The mutual interaction between the tyre tread and road surface creates an impact at the leading end of the tyre. The interface where this interaction occurs, known as contact patch, generates the tyre-road *interaction noise*. Apart from tread impact, several other reasons such as tread release at the trailing end, air flow through the treads and resonances, contribute to tyre *aerodynamic noise*. Both these types of noise collectively contribute to tyre *rolling* noise. Since tyre aerodynamic noise mechanisms are out of scope of this work, no special emphasis is laid on them.
The generated tyre noise is propagated and perceived differently by different individuals. In this chapter, various noise generation and propagation mechanisms that come into play due to the effect of tyre-road interactions are studied. The relevant psychoacoustic and emotional measures associated with the perception of such noises are also discussed.

2.1 Tyre-road noise mechanisms

Treads are components that are designed to ensure constant grip or traction between a tyre and a road surface. They siphon away materials that restrict contact between the interface of the tyre and the road. Their design however, comes at the cost of noise. Various causes that generate noise from a tyre, especially tread can be categorised as:

1. Generation mechanism
    - Mechanical interaction
        - Impact mechanisms - due to transient loads at tyre-road interface
        - Friction mechanisms - due to contact at the tyre-road interface
    - Aerodynamic mechanism
        - Air pumping - at the vicinity of leading and trailing edges
        - Helmholtz resonance - inside the tread pattern cavities
2. Amplification mechanism

Cette thèse est accessible à l'adresse : https://theses.insa-lyon.fr/publication/2022ISAL0081/these.pdf
© [B. Anantharamaiah], [2022], INSA Lyon, tous droits réservés

- Horn effect - due to amplification of contact noise generated at the leading edge
- Air resonance - inside the tread channels.

2.1.1 Mechanical interaction

As the name suggests, noise is generated due to physical interaction between the tyre tread and the road. Mechanical interaction can be of two types, namely - impact mechanism and friction mechanism.

Impact mechanism

Impact mechanism can be observed when the tread and the tyre texture *hammer* against the road surface. With the periodic hammering of treads, there are radial and tangential vibrations generated over tread profile which generates noise. These vibrations are also transferred on to the sidewall regions in the lateral directions that leads to noise due to *running deflection*. It is observed from the previous works that a smooth road surface facilitates the tread noise while the noise due to running deflection is predominantly observed when the tyre rolls over an uneven surface [1].
The impact effect, also known as *reverse impact* effect, is seen in the trailing region of the tyre due to the *hovering* of treads. A representation of impact and the reverse impact mechanism along with their effect on tread vibrations is shown in Figure 2.1. Noise generated due to the impact at the leading edge of the tyre is lower than 1 kHz and at the tyre trailing edge, it is greater than 1 kHz [35].

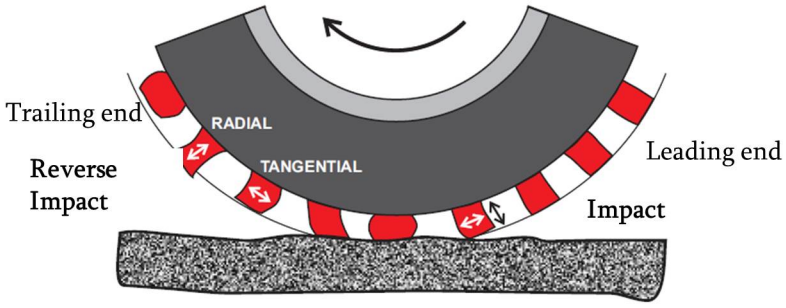

Figure 2.1: Impact and reverse impact tyre-road interaction mechanisms. Image taken from [36].

The running deflection, that leads to sidewall vibration and noise, is shown in Figure 2.2. This mechanism is observed due to the bulging of sidewall region of a tyre between its leading and trailing ends of the contact patch. The running deflection noise is mainly dominated by the design of tyre tread, belt and carcass components [1]. External factors that influence this phenomenon are tyre inflation pressure [37], vehicle loads [1, 35] and road surface texture [1].

Friction mechanism

Friction is a common phenomenon when a tyre interacts with a road surface. However, this friction also contributes to noise generation at the interface. The noise generated due to the friction mechanism can be categorised into two kinds:

- Stick-slip and
- Stick-snap.

Cette thèse est accessible à l'adresse : https://theses.insa-lyon.fr/publication/2022ISAL0081/these.pdf
© [B. Anantharamaiah], [2022], INSA Lyon, tous droits réservés

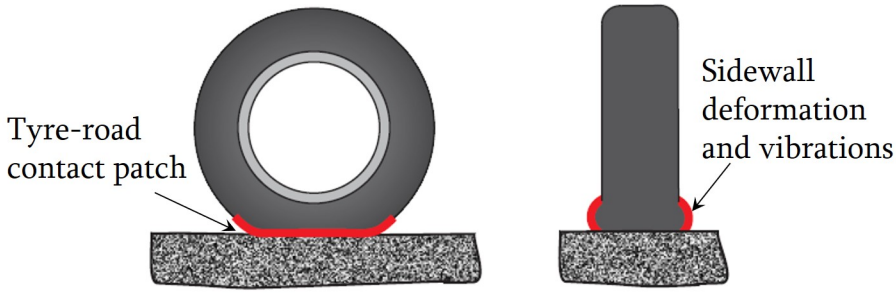

Figure 2.2: Running deflection - a phenomena that leads to vibrations and noise from tyre sidewall. Image taken from [36].

Tyre noise is generated due to the shearing effect of treads, as is the case in both these mechanisms. *Stick-slip* occurs due to the lack of sufficient (negative) friction at the tyre-road interface where the alternative rows of tread stick and slip or *scrub* over the road surface. This is due to instantaneous increase in the tangential forces over the tread surface, e.g. during braking or acceleration of a car. *Stick-snap* is a temperature dependent phenomenon in which noise is generated due to the adhesion of the tyre over the road surface. There are mainly two cases under which stick-snap phenomenon can be observed, namely - (a) when the road surface is hotter than the tread surface and (b) when the tread surface is hotter than the road surface, especially during a roll over an icy road. Due to the temperature gradient, surfaces adhere with each other, generating noise due to hovering.

2.1.2 Aerodynamic mechanism

Aerodynamic mechanism arises due to air turbulence at the vicinity of a rotating tyre. Air flow around a tyre can create rotational and translational turbulence (refer Figure 2.3a) which contribute combinedly to two different noise mechanisms.

Air pumping

Air pumping phenomena happens at the leading and the trailing end of a rotating tyre. At the leading end, tread and grooves instantaneously compress and trap air around the tyre interface. At the trailing end, the air that is trapped between tyre-road interface, gets expanded due to instantaneous increase in volume. This phenomenon of compression and expansion of trapped air is a source of noise from the tyre due to air pumping during its rolling. A depiction of air pumping phenomenon is shown in Figure 2.3b.
Mathematical expression to represent this instantaneous variation in the volume of air around the tyre interface using monopole* theory is given by [1]

$$V' = 4\pi.R^2.R', \tag{2.1}$$

where V' is the derivative of instantaneous volume change in air around tyre interface, R represents the radius of tyre and R' is the first derivative of the radius of tyre. The sound pressure generated due to this mechanism is given by [1]

$$p = \rho V''/4\pi r, \tag{2.2}$$

where ρ is the air density and r represents distance between the source and the receiver.

*A monopole is a point source from where wave disturbances originate and propagate radially.

Cette thèse est accessible à l'adresse : https://theses.insa-lyon.fr/publication/2022ISAL0081/these.pdf
© [B. Anantharamaiah], [2022], INSA Lyon, tous droits réservés

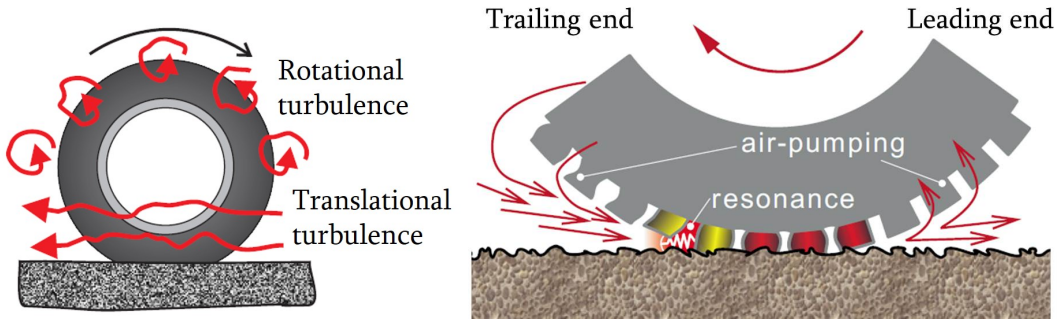

(a) (b)

Figure 2.3: Types of aerodynamic noise generation mechanisms. (a) Air flow turbulence around a rotating tyre Image taken from [36] and (b) Air pumping and Helmholtz resonance mechanism. Image taken from [38]..

Helmholtz resonance

Helmholtz resonance is a phenomenon of vibrations in a spring-mass system. At the interface of the trailing edge, treads and air in the vicinity (of treads) act as a stiffened spring and a mass system, respectively. With time, the mass of the entrapped air increases, thus increasing the mass of the system. Since resonance frequency is a function of spring stiffness and mass variations, the *tonality* or *tonal burst* of the system increases. This increases the overall amplitude of the noise wave generated [1]. A depiction of Helmholtz resonance is shown in Figure 2.3b.

2.1.3 Amplification mechanism

It is seen that the tyres noise is generated, not only by mere mechanical and aerodynamic mechanisms, but also through amplification mechanisms. Amplification mechanisms can be classified mainly into two types namely - horn effect and pipe resonances. Amplification is a far field phenomenon. Hence, the noise perceived due to the amplification (explicitly) is dependent on the distance between the source and the receiver. The effect of amplification is also dependent on tread pattern (for pipe resonance effect) and road surface properties since the road absorptivity also influences the pressure levels of the noise [39].
Since the current work mainly focuses on noise due to mechanical excitation at the tyre-road interface, amplification mechanisms are out of scope from further discussions. However, the reader is referred to [1, 36] for information on horn and pipe resonance effects.

2.1.4 Speed exponents

Although there are several noise generation mechanisms associated with different locations on a rolling tyre, not all occur at the same time but at specific rolling speeds and noise spectrum. There exists an empirical expression to calibrate different types of tyre-road noise generation mechanisms and their corresponding sound levels which is given by [38, 1]

$$L_p = k * A * log(V)[\text{dB}], \tag{2.3}$$

where V and A are the vehicle speed and speed coefficient, respectively. Values of A are dependent on the tyre and road combinations. k represents the speed exponent for noise generation mechanisms which bears a value as tabulated in Figure 2.4 [38].

Cette thèse est accessible à l'adresse : https://theses.insa-lyon.fr/publication/2022ISAL0081/these.pdf
© [B. Anantharamaiah], [2022], INSA Lyon, tous droits réservés

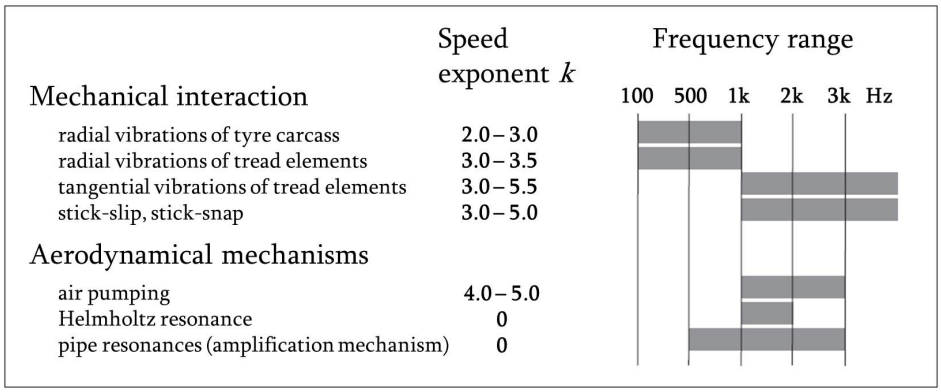

Figure 2.4: Various tyre-road noise generation mechanisms and corresponding speed exponents k [36].

2.2 Tyre noise models

In the field of tyre noise analysis and synthesis, several researchers have attempted to model tyre noise using techniques that can be distinctly categorised into three forms as shown in Figure 2.5.

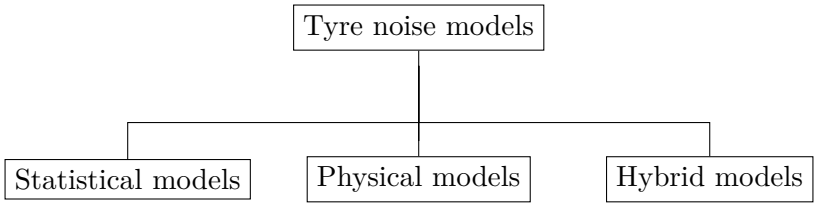

Figure 2.5: Categories of tyre noise modelling techniques.

Statistical models or non-deterministic models mainly use experiments and tests to determine tyre noise and have a zero usage of numerical tool for noise calculations. These models can therefore be effectively used to characterise road surface texture as well as PBN measurements. Few statistical models include Sandberg/Descornet model [1], TINO model [1], etc. Since these models rely mainly on measurements, they are not suitable for the current work, where the prime motive is FE tool development for tyre noise analysis.
Physical models or physics based models consider the development of an FEM or Boundary element method (BEM) or waveguide finite element method (WFEM) models. These models take into account the tyre dynamics and noise radiation. Section 2.3 offers details on methods used in these models and propagation of noise waves. A general physics based model setup is shown in Figure 2.6.

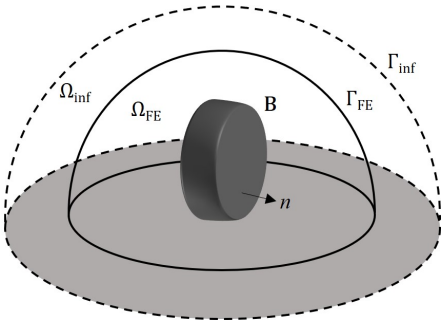

Figure 2.6: A setup of a general physics based acoustic model.

Cette thèse est accessible à l'adresse : https://theses.insa-lyon.fr/publication/2022ISAL0081/these.pdf
© [B. Anantharamaiah], [2022], INSA Lyon, tous droits réservés

In this figure, domain **B** denotes structural or tyre model, Ω_{FE} denotes the domain of discretisation of FEs and Γ_{FE}, the external bound of FEs up to which the effects of noise transmission is of particular interest from the simulation. Any sensor point in a test which is modelled as a microphone, must be included inside this bound. Term Ω_{inf} represents the domain of infinite elements. Its external *far-field* is bounded and denoted by Γ_{inf}. Beyond this limit, the effect of noise wave is not necessary to be calculated. The main purpose of Γ_{inf} is to make sure that the noise waves generating from the bound **B** are not reflected back, i.e. the source does not turn into a sink. However, these bounds and domains modify themselves with the usage of FEs or boundary elements (BEs).

In the past, many researchers have successfully used physics based models for tyre noise and PBN modelling. In the year 2008, Brinkmeyer et al. [40] presented the possibility of using FE for simulating tyre-road interaction noise up to 850 Hz with a possible note on increase in accuracy by discretising the model with smaller element size. Although this work included a deterministic tyre model, the behaviour of NTF was restricted only to simulations (without any validation from tests). The same FE model was verified for tyre-road noise generation for a tyre rolling over a drum [41]. Lafont et al. [42] modelled the contact patch of tyre-road interface with the help of monopoles and successfully generated noise velocity maps for different tyre speeds for PBN analysis. WFEM was used to model the tyre modal behaviour and noise radiation from this model with the help of FEs and infinite elements (IFEs). More description on IFEs is provided in Section 2.3.2. It was found that the contact patch was the prime contributor to noise generation beyond the frequency of 400 Hz - 2 kHz. WFEM has been found very effective in modelling the mode shapes of tyres for up to 800 Hz (although the possible prediction domain is up to 1.5 kHz) [43]. Nevertheless, there is still the lack of accuracy with the noise propagation domain since it has to be modelled using the FEs.

By the works considered from the mentioned researchers and few others [44, 45], it was found that, even though WFEM is a possible accurate modelling technique for tyre dynamics, the accuracy of noise propagation model still stalls up to a frequency limit of 500 - 800 Hz. Although Brinkmeyer et al. [40] was capable of extending this limit up to 850 Hz, the total number of elements considered for the simulation was of the order 1E4, which needs a lot of computational resources and time.

Furthermore, it was found that WFEM lacks the capability of predicting the accurate stiffness of tyre rubbers. Investigations revealed that this issue is due to the overestimation of sidewall stiffness [46]. This is because WFEM technique involves modelling of tyre geometry using only few nodal points, leading to higher stiffness accumulation per node during tyre inflation step in simulations. Hence, WFEM rules down the possibility of any kind of material and geometrical non-linearity which is an important factor when considering the noise perturbations generated due to stiffness of sidewall and/or the damping effects of rubber materials.

Alongside FEM and WFEM, BEM techniques were also used in parallel for tyre noise generation and propagation modelling. The main difference in modelling a setup using BEM is that the bounds and domains Ω_{FE}, Γ_{FE} and Ω_{inf} (refer Figure 2.6) are completely eliminated. The radiation of noise is modelled as a boundary value problem over the domain Γ_{FE} using Neumann or Direchlet or Robin boundary conditions. The reader is referred to Section 2.3 for more information on these. Approaches in the past also modelled a tyre with either FEM or WFEM, but the noise radiation using BEs instead of FEs or IFEs [47, 48]. However, one exception was that of a PBN test setup, that was modelled using BEM, in which the complete vehicle body was discretised using BEs [49]. Noise levels were compared between the simulation and tests for a car traveling at various gear levels. The results showed good agreement with the tests and segregated the overall noise of tyres from various components (exhaust, engine, etc.). In the year 2014, Wei et. al [50] developed an FE model of tyre using BEs of sensor points to predict the noise spectra of a rolling truck tyre. It was found that contact patch was the major contributor to tyre noise up to 1 kHz. The reader is referred to few other studies on tyre noise and noise

Cette thèse est accessible à l'adresse : https://theses.insa-lyon.fr/publication/2022ISAL0081/these.pdf
© [B. Anantharamaiah], [2022], INSA Lyon, tous droits réservés

measurements using BEM [47, 48].
In the past, BEM was considered as an expensive technique for the calculation of noise propagation problems. This is because, the standard BEMs used elements whose nodal values were calculated by direct method that involved storage of element matrices of the order $\mathcal{O}(N^2)$ [51, 52]. This increased the need for storage capacities. With the advent of fast multipole method (FMM) or fast multipole BEM (FMBEM), the order of element storage was redefined to an order of $\mathcal{O}(NlogN)$. Although this reduced the storage cost and increased the accuracy [53, 54], it was still time consuming with respect to frequency based analyses, which requires at least six elements per wavelength [55]. With the recent advancements in general modelling techniques, e.g. model order reduction techniques implemented along with latest BEM algorithms (e.g. energy BEMs (EBEM), Krylov subspace based BEMs and pre-corrected FFT model), the BEM problems use iterative procedures that converge the solution relatively faster [56, 57, 58].
Although these discussions prove that BEM is a possible method for modelling tyre noise propagation, it should be noted that BEM only calculates the solution of a problem as a boundary value and discards the contribution of noise propagation medium (e.g. air). This means that the input at a tyre **B** is reciprocated as an effect at an external far field Γ_{inf} governed by *Green's function* [52]. Also, in case of large models, BEM formulations need to be simplified or preconditioned to speed up calculations [59]. Due to these main disadvantages, FEM based physics model is considered in this work.
Hybrid models are an amalgamation of statistical and physical models - the force applied on the tyre or the physics of contact patch is studied in a physics model and the results of this are used as an input for a statistical model. Two important hybrid models are the HyRoNE (hybrid rolling noise estimation) and SPERoN (statistical physical explanation of rolling noise) [60]. Since hybrid models mainly focus on non-deterministic approach, these models are not of interest in this work. However, interested reader is referred to [60, 61] for more details on these models.

2.3 Noise wave propagation and physics based models

Noise propagates, in general, in gases and liquids as pressure waves. The constant of propagation, c, in a fluctuating medium is defined as

$$p = c^2 \rho. \tag{2.4}$$

In the above equation, p and ρ represent the pressure and density of a medium in which the acoustic wave propagates. This propagating wave is mathematically expressed as a hyperbolic partial differential equation (PDE) using *Euler's wave equation*. This is expressed as

$$\frac{\partial^2 p}{\partial t^2} = c^2 \Delta p, \tag{2.5}$$

where t represents the time of wave travel, and Δ, the scalar product of partial derivatives $(\nabla.\nabla)$. The value of p is estimated in a geometric domain Ω that can be bounded or unbounded as shown in Figure 2.7.
The Euler's equation of motion for such a system is given by [62]

$$\Delta p(x,t) = \frac{1}{c^2} \frac{\partial^2 p(x,t)}{\partial t^2}. \tag{2.6}$$

The homogeneous Helmholtz-equation can be deduced from Equation 2.6 by considering time-harmonic dependence of p given by

$$\Delta p(x,\omega) + k^2 p(x,\omega) = 0, \tag{2.7}$$

Cette thèse est accessible à l'adresse : https://theses.insa-lyon.fr/publication/2022ISAL0081/these.pdf
© [B. Anantharamaiah], [2022], INSA Lyon, tous droits réservés

where k denotes the wave-number and ω, the wave velocity. The above equation completely describes the linear time harmonic condition if either admittance/Robin boundary condition or Neumann boundary condition or Direchlet boundary condition is enforced. For more information about these boundary conditions and theoretical definitions, the reader is referred to [52].

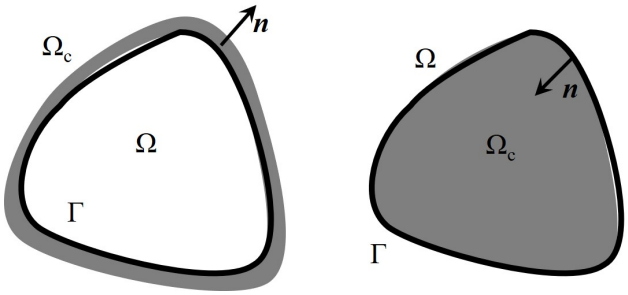

Figure 2.7: Definition of Ω, Ω_c, Γ and $\mathbf{n}$ for (a) interior problem and (b) exterior problem.

In general, the Helmholtz equation is analytically capable of handling basic geometries. But in case of complex geometries, FEM would be convenient. However, the same Helmholtz equation is used to develop the weak integral form which reads as [63],

$$\begin{gathered}\int_\Omega[\Delta p(x)+k^2p(x)]\chi(x)d\Omega= \\ \int_\Omega(\nabla\chi(x).\nabla p(x)-\chi(x)k^2p(x))d\Omega-sk\int_\Gamma\chi(x)(Yp(x)+u_s)d\Gamma=0,\quad\forall\chi(x)\in W(\Omega),\end{gathered} \tag{2.8}$$

where $\chi(x)$ is a generic test function, u_s is the known velocity at boundary Γ. Term s is defined as

$$s=i\rho_0 c, \tag{2.9}$$

where ρ_0 is the ambient density of the medium in which the pressure wave propagates. Equation 2.8 is called the *Galerkin equation*. By *discretising* the domain of a boundary, the FE mesh is generated and a trial function

$$p(x)=\sum_{l=1}^{N}\phi_l(x)p_l=\boldsymbol{\phi}^T(x)\boldsymbol{p}, \tag{2.10}$$

is introduced into Equation 2.8. In the above equation, p_l denotes discreet sound pressure at point x_l of the FE meshed region and ϕ_l is the l-th basis approximation function. On simplification, the governing law for FEM for acoustic wave propagation reads as

$$[-k^2\mathbf{M}-ik\mathbf{C}+\mathbf{K}]\mathbf{p}=\mathbf{f}, \tag{2.11}$$

where stiffness matrix $\mathbf{K}$ is defined as

$$k_{jl}\int_\Omega=\nabla\phi_j^{(p)}.\nabla\phi_l^{(p)}d\Omega, \tag{2.12}$$

the damping matrix $\mathbf{C}$, as

$$c_{jl}=\rho_0 c\int_\Gamma\phi_j^{(p)}\left(\sum_{j=1}^{N^{(Y)}}Y_j\phi_j^{(Y)}\right)\phi_l^{(p)}d\Gamma, \tag{2.13}$$

Cette thèse est accessible à l'adresse : https://theses.insa-lyon.fr/publication/2022ISAL0081/these.pdf
© [B. Anantharamaiah], [2022], INSA Lyon, tous droits réservés

the mass matrix $\mathbf{M}$, as

$$m_{jl} \int_{\Omega} = \phi_j^{(p)} \phi_l^{(p)} d\Omega. \tag{2.14}$$

The boundary vector $\mathbf{f}$ is given by

$$\mathbf{f} = sk\Theta \mathbf{u_s}, \tag{2.15}$$

where $\mathbf{u_s}$ is a vector and Θ is the boundary mass matrix given by

$$\theta_{jl} = \int_{\Gamma} \phi_j^{(p)} \phi_l^{(u_s)} d\Gamma. \tag{2.16}$$

These are the equations that a solver computes when a wave propagation model is discretised using FEs.

2.3.1 Sommerfeld radiation condition

In reality, any external noise generated from its source disperses/propagates into an infinite or unbounded domain. However, if this condition has to be imposed in a simulation, it is practically difficult. Hence, an unbounded domain is bounded by an imaginary domain to calculate such problems. An illustration of this is shown in Figures 2.8a and 2.8b. Apart from the general admittance or Neumann or impedance boundary conditions, the *Sommerfeld radiation condition* (SRC) is also imposed. This condition states that a source cannot be a sink, i.e. the noise generated from a source is always outgoing/scattering. This condition is represented mathematically as

$$\lim_{r \to +\infty} r^{\frac{d-1}{2}} \left(\frac{\partial u(r)}{\partial r} - iku(r)\right) = 0, \tag{2.17}$$

where u, r and d are wave velocity, radial coordinate and the spatial dimension, respectively. For a 1D case, d takes a value of 1 and hence Equation 2.17 reduces to

$$\lim_{r \to +\infty} \left(\frac{\partial u(r)}{\partial r} - iku\right) = 0. \tag{2.18}$$

An illustration of the above condition is shown in Figure 2.8c.

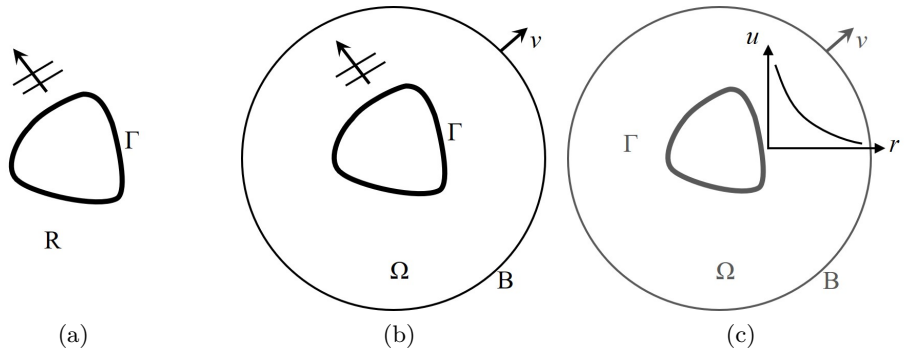

Figure 2.8: Replacing an (a) unbounded domain by a (b) bounded domain. Images taken from [52]. Subfigure (c) illustrates the Sommerfeld radiation condition for wave propagation.

2.3.2 Absorbing boundaries and infinite elements

Although SRC is induced in the numerical models of acoustic wave propagation, the incident waves do not attenuate at the external boundaries (refer Figure 2.8b) and must be numerically

Cette thèse est accessible à l'adresse : https://theses.insa-lyon.fr/publication/2022ISAL0081/these.pdf
© [B. Anantharamaiah], [2022], INSA Lyon, tous droits réservés

truncated. If not, these lead to reflections and/or *acoustic pollution* in the interior domain. In order to avoid this problem, absorbing boundaries are helpful.
Bayliss and Turkel proposed an *absorbing boundary condition* (ABC) by conditioning the scalar wave equation in three-dimensions in terms of Jth-order terms [64]

$$\left[\prod_{j=1}^{J}\left(\frac{1}{c}\frac{\partial}{\partial t}+\frac{\partial}{\partial r}+\frac{2j-1}{R}\right)\right]u=0 \quad \text{on } \mathbf{B}. \tag{2.19}$$

However, this technique could not be implemented in large sized problems since higher order J-th term was necessary and the computational time to solve the derivatives was high.
As a further development, an absorbing layer was designed encompassing the interior domain that dampened the incident waves using viscous and friction damping terms. This design is shown in Figure 2.9a.

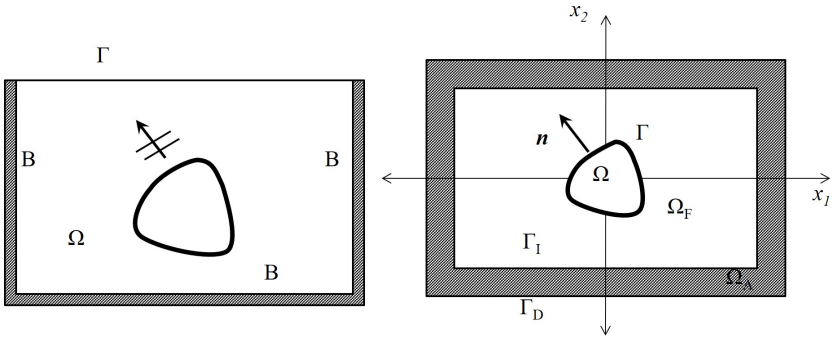

Figure 2.9: Absorbing boundaries. (a) Setup of an absorbing layer (image reference [52]) and (b) perfectly matched layer (image reference [52]).

The associated formulation of the layer to dampen a plane wave incident on it was developed as [65]

$$\frac{\partial^2 u}{\partial t^2}=c^2\frac{\partial^2 u}{\partial x^2}+\mu(x)\frac{\partial^3 u}{\partial x^2 t}-\nu(x)\frac{\partial u}{\partial t}, \tag{2.20}$$

where $\mu(x)$ and $\nu(x)$ are the viscous and friction damping terms.
The absorbing layer laid the foundation for *perfectly matched layer* (PML) as shown in Figure 2.9b. This was designed mainly to offer zero reflections in the interior domain Ω_{F} by decaying the incident waves *exponentially* between the domains Γ_{I} and Γ_{D}. In case the wave does not die out completely at Γ_{D}, it gets reflected back to Γ_{I} with higher exponential decay, thus getting attenuated and restricted to seep back into Ω_{F}. The governing set of decay expressions was derived by Berenger and Zhao et. al. The reader is referred to [66], [67] and [68] for a deeper understanding.
In terms of reducing the computational efforts, *infinite elements* (IFEs) are very beneficial. This is because, IFEs do not dissipate the energy in the incident waves but act as a catalyst to propagate them to far fields. By this technique, the need of onerous procedures of wave conditioning, truncation and discretisation can be eliminated. In terms of modelling, there exists no difference between the conventional FEs and the IFEs. However, the prime difference is the method in which the impedance is applied at a boundary far from the source which is given by

$$\frac{dp}{dr}=-ikp \quad \text{at } r=R. \tag{2.21}$$

Cette thèse est accessible à l'adresse : https://theses.insa-lyon.fr/publication/2022ISAL0081/these.pdf
© [B. Anantharamaiah], [2022], INSA Lyon, tous droits réservés

This means that SRC is taken into account at a point at a distance R as $R \to \infty$. The location of R is shown in Figure 2.10.

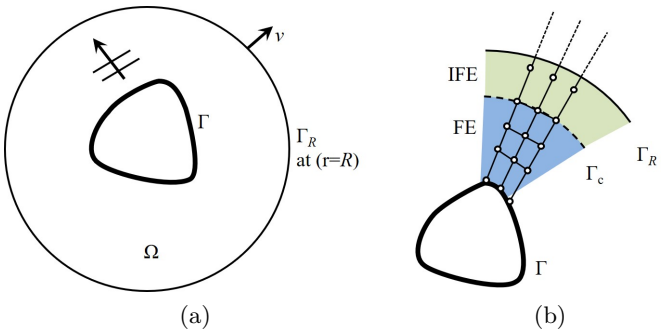

Figure 2.10: An IFE model. (a) IFE model boundary setup and (b) types of element discretisation in an IFE model. Images taken from [69].

For the above condition, the Galerkin equation (Equation 2.8) is reformulated as [69]

$$\begin{aligned} &\int_\Omega (\nabla\chi(r).\nabla p(r) - \chi(r)k^2 p(r))d\Omega - sk\int_\Gamma \chi(r)(Yp(r)+u_s)d\Gamma \\ &+ik\int_{\Gamma_r}\chi(r)p(r)d\Gamma_r = 0, \quad \forall\chi(r)\in W(\Omega). \end{aligned} \tag{2.22}$$

The nodal acoustic pressures are calculated using continuous trial solution [69]

$$p(x,\omega) = \sum_{\alpha=1}^{n} q_\alpha(\omega)\phi_\alpha(x,\omega), \tag{2.23}$$

where $\phi_\alpha(x,\omega)$ are the global shape functions where n defines the total number of nodes in the FE and IFE meshes. In case of radial problems, Equation 2.23 is evaluated using the interpolation functions as [69]

$$g_i(\theta) = \frac{\theta-\theta_j}{\theta_i-\theta_j}, \text{ and } g_j(\theta) = \frac{\theta-\theta_i}{\theta_j-\theta_i}, \tag{2.24}$$

where i and j represent the adjacent nodes in the IFE mesh domain as shown in Figure 2.11. For further information about the types and formulations of IFEs, the reader is referred to [52, 69].

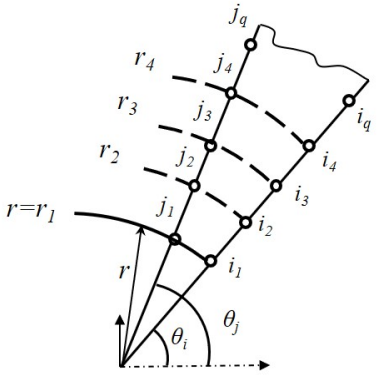

Figure 2.11: Infinite elements in radial dimension. Image taken from [69]

Cette thèse est accessible à l'adresse : https://theses.insa-lyon.fr/publication/2022ISAL0081/these.pdf
© [B. Anantharamaiah], [2022], INSA Lyon, tous droits réservés

2.4 Psychoacoustic and emotional measures

Once the simulated tyre noise is convolved for various cases (e.g. speeds, loads and inflation pressures), these audio files are subjected to perception or psychoacoustic studies. In the listening tests, listeners hear the generated and measured tyre rolling noise in an anechoic room using headsets and grade the audio attributes, especially their unpleasantness.
Psychoacoustical studies, particularly in designing acoustically comfortable and/or detectable product, is gaining importance recently due to various reasons, of which permissible noise regulations is one of them. A sound has various attributes in it and psychoacoustical studies tap these attributes to capitalise them for specific purposes based on the necessities. These attributes also influence the sound perception emotionally in terms of its subjective feeling. A detailed explanation on the processing of sounds by human ear to the brain for auditory perception is explained in [70]. Such psychoacoustical and emotional measures are introduced in this section briefly.
With respect to tyre noise psychoacoustics, very few contributions have been made in the past. This is because, this field is still in its cradle stages or industry specific needs have not yet surfaced. Also psychoacoustics has not yet been used for tyre noise because it is currently controlled by regulations only with respect to its emissions. However, as previously mentioned, with the implementation of EVs, it is necessary to make sure that a slow moving car makes minimum noise to ensure pedestrian safety. Since tyre-road interaction noise is the next source of noise from cars, it is worth investigating the psychoacoustic links to tyre noise. Most of the existing works on tyre noise psychoacosutics are experimental [71, 72, 73]. In terms of simulating the tyre noise, Hoffmann et. al [74, 75] and Forssen et. al [76] have synthesised tyre noise using SPERoN and HyRoNE models (hybrid models, refer Section 2.2). Since these are non-deterministic models, they cannot investigate the influence of tyre material properties, tread pattern etc. on tyre noise, which is necessary to generate variations in noise excitation patterns. Hence, a deterministic model needs to be studied for industrial applications in terms of tyre noise psychoacoustics.

2.4.1 Hearing area

Human hearing regime is bounded by two limits - threshold in quiet and threshold of pain. Threshold in quiet is the just audible level of a pure tone expressed as a function of frequency. This limit is not the same for all ages; it increases with the age of an individual, especially the high frequency regimes of the tone [77]. The threshold of pain is the maximum limit of a sound level that an individual can sustain. Beyond this limit, the individual will suffer from hearing loss. The human hearing regime and the thresholds in quiet and of pain are shown in Figure 2.12.

2.4.2 Masking

Masking is a phenomenon in which the threshold in quiet increases for a given audio tone due to the presence of either a broadband noise, narrow-band noise, other tones (pure tones or complex tones) or a combination of several. A simple example in daily-life situation is when the person speaking to another has to raise his voice in case the environment of interaction changes from a silent to a noisy one. Masking is not only observed in terms of frequency content but also for the duration for which an audio/noise signal is heard. This is called *temporal effect* of masking. A detailed description of various masking types and their effects is provided in [77].

Cette thèse est accessible à l'adresse : https://theses.insa-lyon.fr/publication/2022ISAL0081/these.pdf
© [B. Anantharamaiah], [2022], INSA Lyon, tous droits réservés

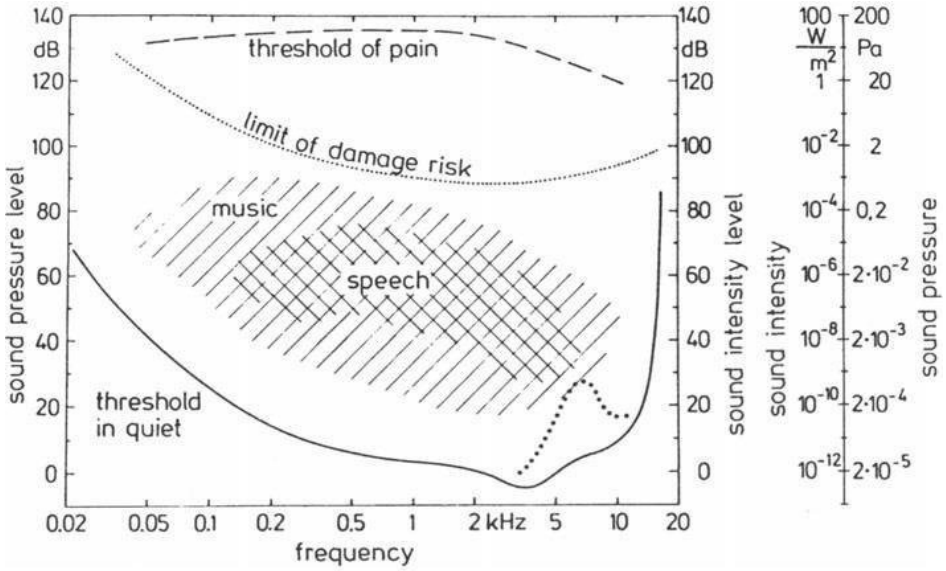

Figure 2.12: Human hearing regime. Image taken from [77] and according to [78].

2.4.3 Critical band rate

Critical Bands are necessary to describe the variations in hearing sensations. These bands consist of a set/bandwidth of frequencies that describe the frequency bandwidth of the "auditory filter" created by the cochlea of Human ear. A sample critical bandwidth as a function of frequency is shown in Figure 2.13a.
From this figure, it can be observed that the human ear can analyse a bandwidth of 100 Hz for an audio frequency up to 500 Hz. Beyond this frequency limit, the critical band varies by 0.2 times of the frequency of the audio. This variation can also be represented in terms of *how fast they vary* which is called *critical band rate* as shown in Figure 2.13b. In this figure, the band rate variations (in ordinate axis) are denoted by Bark which is a unit that corresponds to the loudness level for which a particular critical band plays an important role.

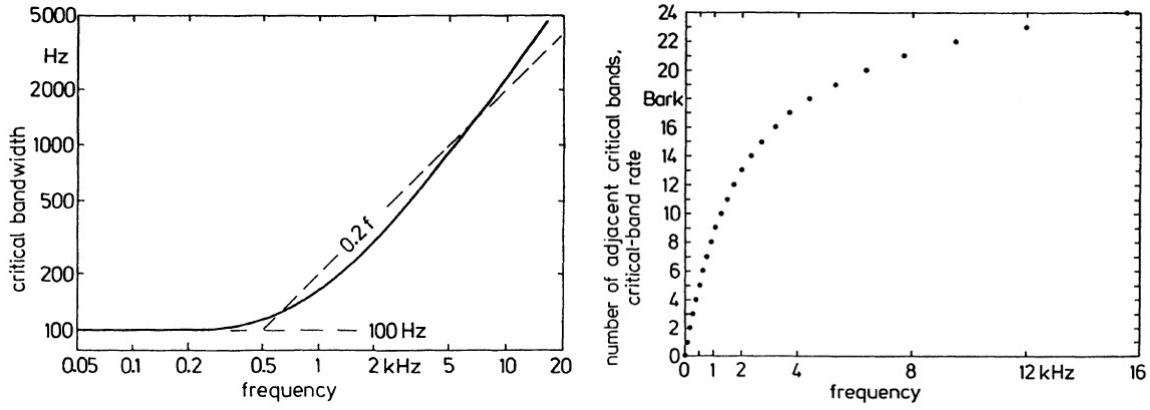

(a) (b)

Figure 2.13: Understanding (a) critical bands and (b) critical band rate. Images taken from [79].

Cette thèse est accessible à l'adresse : https://theses.insa-lyon.fr/publication/2022ISAL0081/these.pdf
© [B. Anantharamaiah], [2022], INSA Lyon, tous droits réservés

2.4.4 Loudness

Of all the properties of a set of tones, the easiest to identify and sort is loudness. The *loudness* level of a tone is defined as the *times by which* a 1 kHz reference tone sounds equally as loud as the same tone [77]. This comparison is made in decibel (dB) of sound pressure levels (SPL) of the tones and the unit is *Phon*. For such comparisons, 1 kHz tone is chosen as a standard. From comparison of loudness, an equal loudness contour was established as shown in Figure 2.14.
From this figure, it can be observed that a 60 dB SPL tone at 1 Hz sounds four times louder than the same tone of 40 dB SPL. Or the loudness of 60 dB SPL tone is 4 Phon. As a practice, not only the loudness of a tone is compared at 1 dB SPL but also other characteristics of the tone, such as pitch, fluctuation strength, roughness and other emotional measures [77].

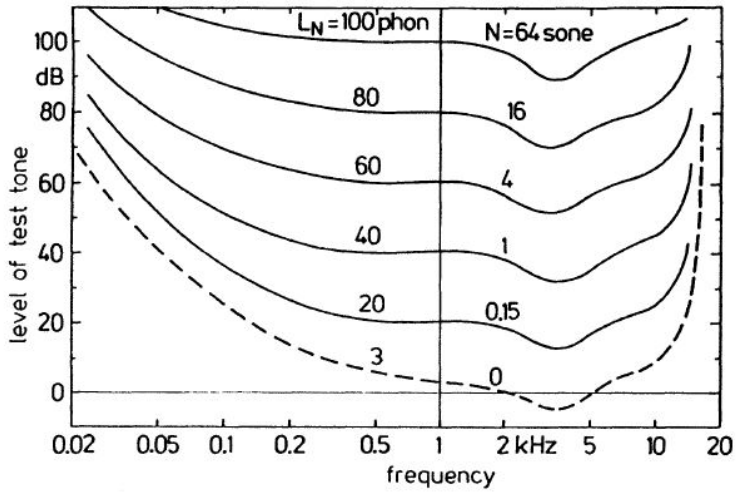

Figure 2.14: Equal loudness contour. Image taken from [77].

2.4.5 Pitch, sharpness and roughness

The *pitch* of a tone describes how high or low it is. A high tone has a high pitch and a low tone has a low pitch. The unit of pitch is *mel*. It is defined by a frequency of 1 kHz with 40 dB above the hearing threshold, producing a pitch of 1,000 mel [77].
Sharpness of a sound provides information about its frequency distribution in its envelope [77]. Sharpness mainly depends on the spectral content of the noise. Additionally for narrow band noise, the central frequency of the sound characterises its sharpness. Sounds with high sharpness are described as high-pitched or distinctive.
Roughness in a sound arises when closely spaced frequencies interfere with, envelope over and modulate each other. It is usually observed in amplitude and/or frequency modulations of signals with modulation frequencies between 15 to 300 Hz [77] and is expressed in *Asper*.
For more detailed information on pitch, sharpness and roughness for auditory perception, the reader is referred to [77].

2.4.6 Pleasantness and annoyance

Pleasantness of a sound can be positive or negative, i.e. a sound can be pleasant or unpleasant. Usually, the pleasantness of a sound is a combined function of loudness, sharpness, roughness and/or tonal components. One such model is described in [77].
Annoyance is contra-pleasantness which is mainly a function of SPL of an audio [80]. This type of attribute is associated with negative and/or aggressive emotions. For more details about the models of annoyance, the reader is referred to [77] in which the author describes the model

Cette thèse est accessible à l'adresse : https://theses.insa-lyon.fr/publication/2022ISAL0081/these.pdf
© [B. Anantharamaiah], [2022], INSA Lyon, tous droits réservés

considering loudness, sharpness, roughness and fluctuation strength of audio data.
In the past, extensive study on tyre noise psychoacoustics was performed by Hoffmann et. al [81]. In this work, it was observed that there was very small noticeable changes in the perception of tyre road noise for various cases. The only significant differences in the tyre noise were observed in terms of pitch and sharpness. However, the annoyance was rated in the inverse behaviour. Most important factor that influence the overall perception of the tyre rolling noise was found to be the loudness of the audio signal. Nevertheless, all these studies were carried out using the hybrid tyre noise models and not the physical ones (refer Section 2.2). However, in this work the annoyance of tyre rolling noise is graded using rolling noise synthesised from physical models that are modelled using FEs.

Cette thèse est accessible à l'adresse : https://theses.insa-lyon.fr/publication/2022ISAL0081/these.pdf
© [B. Anantharamaiah], [2022], INSA Lyon, tous droits réservés

Cette thèse est accessible à l'adresse : https://theses.insa-lyon.fr/publication/2022ISAL0081/these.pdf
© [B. Anantharamaiah], [2022], INSA Lyon, tous droits réservés

3

Calibration of tyre rubber hyperelasticity

Tyre structures are based on composite materials that constitute numerous layers, each making their own contribution to tyre mechanic and dynamic behaviour. In principle, the understanding of the partial contributions of individual layers requires knowledge of their mechanical properties. In the case of non-availability of such critical information, it is difficult to develop tyre FE models. The evolution of currently existing tyres has seen constant developments and upgradings in terms of its design and materials, especially rubbers. Although pneumatic tyres appear simple, their construction is a complex process. A sample rubber cross-section of a passenger car pneumatic tyre is shown in Figure 3.1. From this figure we can see that a tyre comprises not only of rubbers but also other materials, e.g. plies and belts that are made of steel and nylon. Each rubber of a tyre has individual contributions to the overall design, development and performance of the tyre, e.g. ease of construction, tyre stiffness, traction, noise etc.

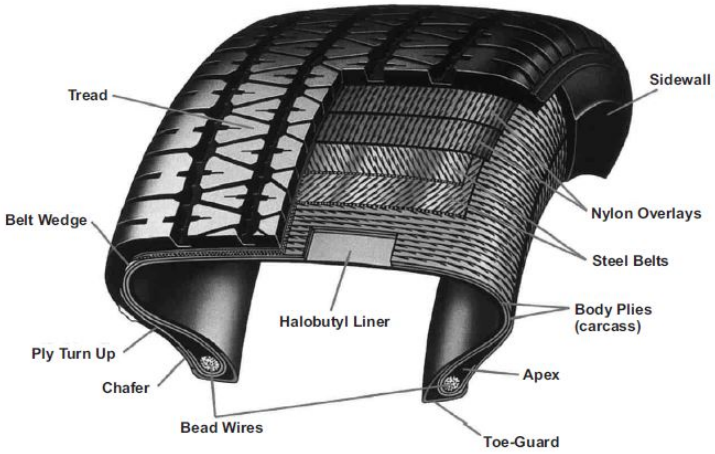

Figure 3.1: Parts of a pneumatic tyre. Taken from [4] as an example.

Although rubber manufacturers can provide the accurate material properties of constituent rubbers, i.e. the rubber hyperelasticities and viscoelasticities, these are mere theoretical values and restricted to their behaviour when isolated and tested prior to any curing process*. During the tyre manufacturing process, these individual rubbers are sandwiched and subjected to various temperatures and curing processes which will modify their behaviour. To estimate the correct behaviour of a tyre, this complication must be overcome, which is exactly the aim of the work that is discussed in this chapter. Here, the hyperelastic property of each individual rubber material

*Curing is the process of applying pressure to rubbers set in a tyre mold in order to *fine-shape* a tyre. This process also applies heat energy to stimulate the chemical reaction between rubber compounds and other materials.

Cette thèse est accessible à l'adresse : https://theses.insa-lyon.fr/publication/2022ISAL0081/these.pdf
© [B. Anantharamaiah], [2022], INSA Lyon, tous droits réservés

of tyre is characterised for modelling tyre static and modal behaviour using tyre characteristic responses from tests, FE modelling and DoE techniques. A brief description of DoE is provided in Appendix A SectionA.4

3.1 Tyre FE model simplification and characterisation

In order to develop a tyre FE model, this work employs the hybrid modelling technique. The development process using this technique is shown in Figure 1.13. Material models available for the rubbers associated are (refer Figure 3.1 for rubber regions):

- bead wire and belts defined as steel;
- carcass/body plies and nylon overlays modeled using the Marlow model;
- all rubbers (except apex and chafer) described by the Yeoh model and
- apex and chafer rubbers modeled using the Mooney-Rivlin model.

Relevant mathematical formulations of these models are discussed in Section 1.3.1. However, in this work, all tyre rubbers are modelled using the Mooney-Rivlin model given by

$$W = C_{i0}(I_1 - 3) + C_{0i}(I_1 - 3) + \frac{1}{D_i}(J_{el} - 1)^2. \tag{3.1}$$

This is because the terms (as seen in equation 3.1) necessary for the calculation of the strain energy density (and thus the material behaviour) are C_{10}, C_{01} and D_1. These terms can be expressed in terms of the Young's modulus of the material as [82]

$$C_{10} = 0.1333 * E, \tag{3.2}$$

$$C_{01} = 0.0333 * E, \tag{3.3}$$

and

$$D_1 = \frac{1}{50}(C_{10} + C_{01}), \tag{3.4}$$

in all of which the Young's modulus is determined by estimating the test curve fit coefficients as [82]

$$E = A.c_1 + A^2.c_2 + A^3.c_3. \tag{3.5}$$

In the above equation c_1, c_2 and c_3 are the constants of curve fitting, A and E represent the rubber hardness (represented using *shoreA* scale) or simply rubber hardness (corollary rubber hyperelasticity) and the Young's modulus, respectively. Using the above mentioned material characterisation procedure, the tyre cross-section is simplified from eleven rubbers to six rubbers. This simplification is based on the information obtained from the tyre collaborator (associated with the project) based on the dynamic mechanical analysis (DMA) of the dominant rubbers of the tyre. According to this, those rubbers that have the highest and the lowest degree of material influence (hyperelasticity and viscoelasticity) in the localised regions are given the highest priority. Other rubbers whose material behaviour lies between these limits are merged with the adjacent layers. In case of any conflict, rubber regions with comparatively smaller thickness and those rubbers that assist only during the tyre manufacturing are given lowest priority and are merged with their adjacent regions. This simplification leads to IDIADA axi-model. The difference between the simplified IDIADA axi-model and the initial axi-model is shown in Figure 3.2. With the change in constituent rubber volume, the mass of the FE tyre model also changes. This change of mass is compensated by proportionally altering the density of the tyre individual rubbers. Thus, the mass of the tyre FE model stands same as that of the real tyre with a value of 18 kg.
After having simplified the tyre FE model, the behaviour of individual rubber regions need to be characterised. This is achieved using the DoE technique. For this, each region of the tyre

Cette thèse est accessible à l'adresse : https://theses.insa-lyon.fr/publication/2022ISAL0081/these.pdf
© [B. Anantharamaiah], [2022], INSA Lyon, tous droits réservés

has to be named for parameterisation. The naming convention of the simplified IDIADA tyre geometry is as shown in Figure 3.3. Using this model as a reference in the DoE, the contribution of the material properties of individual rubbers/regions on the overall tyre static and dynamic behaviour is studied. For the static behaviour studies, the FE tyre model is inflated to 2.4 bar although the air is not modelled. In the dynamic behaviour study, the inflated tyre FE model is also modelled with air elements.

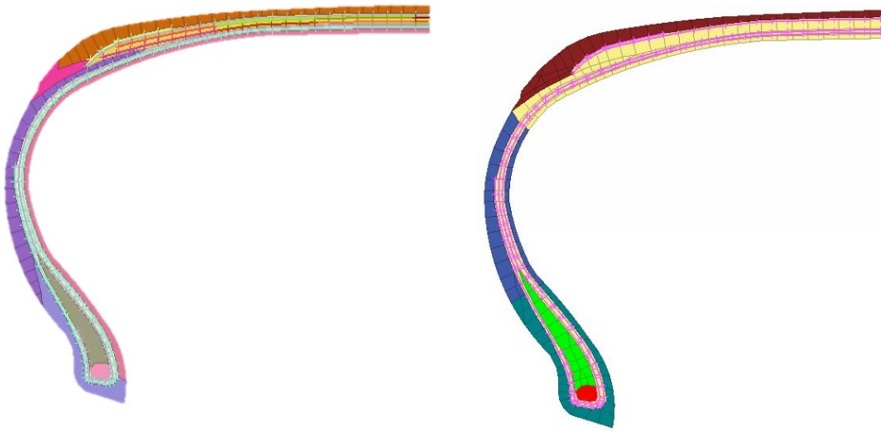

(a) (b)

Figure 3.2: 2D axisymmetric tyre models. (a) Currently exiting complex model and (b) simplified IDIADA tyre axi-model developed based on the prime functional regions of the tyre. The tread remains unchanged and hence not shown here.

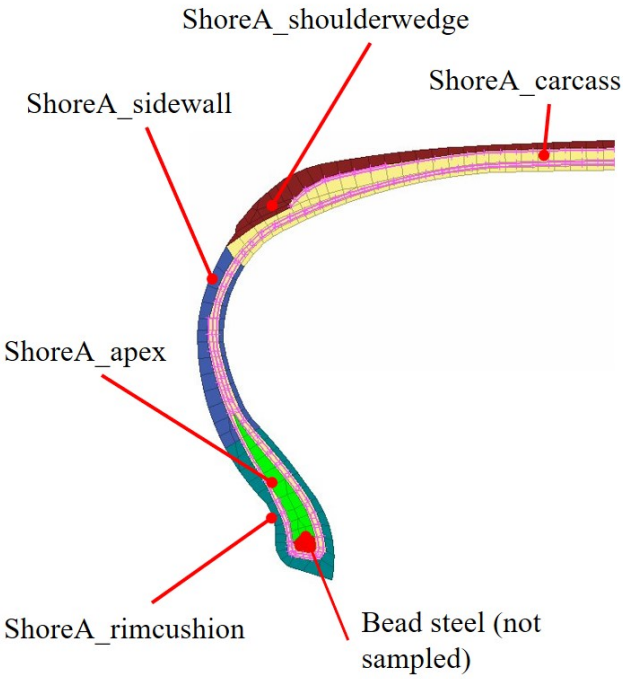

Figure 3.3: Simplified rubber regions based on their dominant local influence in the tyre geometry as realised from the DMA analysis from the tyre manufacturer.

Cette thèse est accessible à l'adresse : https://theses.insa-lyon.fr/publication/2022ISAL0081/these.pdf
© [B. Anantharamaiah], [2022], INSA Lyon, tous droits réservés

3.2 Static behaviour study

Static tyre behaviour is described by the radial, the longitudinal and the lateral stiffness of the tyre that are measured on a static stiffness measurement (SSM) machine as shown in Figure 3.4. As seen from this figure, the anvil applies a load on the tyre in radial, lateral and longitudinal directions (in separate tests) and tracks its own displacement correspondingly. The tyre inflation pressure is set to 2.4 bar. The static behaviour from the test is used as a reference to correlate the tyre stiffness in FE simulations.

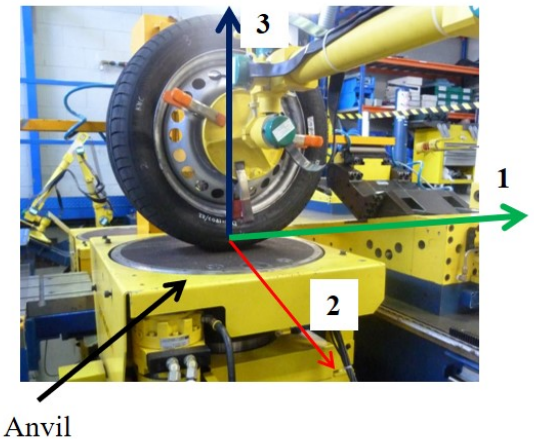

Figure 3.4: SSM test setup to measure the tyre static stiffness at IDIADA. Axes 3, 2 and 1 represent the radial, lateral and longitudinal directions of anvil movements with respect to the tyre, respectively.

DoE using the LHS technique is used to generate tyre FE models with random rubber hardness values. In each of these simulations, the stiffness of the FE model is correlated against the behaviour/stiffness measured on the SSM machine. For the DoE, the lower and upper limits of hardness values (expressed in terms of shoreA) for each rubber are the inputs for sampling and are shown in Table 3.1. These values are estimated by measuring the hardness using a shoreA hardness gauge. However, this does not lead to accurate values since many rubber regions are now simplified into one region that locally dominates the tyre response as shown in Figure 3.2. The plies hyperelasticity is sampled by scaling the reference behaviour. The model comprising of appropriate rubber stiffness is then obtained by optimisation of the resulting data obtained post DoE process.

Table 3.1: Upper and lower limit for sampling the hardness (in shoreAs) of the rubber regions. Optimised values of hardness (in shoreA) are normalised due to confidentiality.

Parameter	Rubber/ply name	Lower limit	Upper limit	Optimised value
ShoreA_sidewall	Sidewall	35	75	54.33
ShoreA_tread	Tread	35	90	55.0
ShoreA_apex	Apex	35	95	66.64
ShoreA_carcass	Carcass	35	75	55.0
ShoreA_shoulderwedge	Shoulderwedge	35	75	43.88
ShoreA_rimcushion	Rimcushion	35	80	58.33
Factor_cap_ply	Cap ply	0.2	2.0	1.29
Factor_carcass_ply	Carcass ply	0.2	2.0	1.83

Cette thèse est accessible à l'adresse : https://theses.insa-lyon.fr/publication/2022ISAL0081/these.pdf
© [B. Anantharamaiah], [2022], INSA Lyon, tous droits réservés

Figure 3.5a provides a comparison for the radial stiffness of the tyre between SSM test and FE simulations with the optimised values of rubber hardness. From this figure, it can be seen that there is a good agreement with the test and the simulation. Similarly, Figures 3.5b and 3.5c show good agreement between the test and the simulation results. The underestimation of the lateral stiffness as in Figure 3.5b can be rectified by a finer mesh model; this, however, comes at the cost of computational time. Nevertheless, the slope of the optimised and the test curves in this figure is identical and hence can be considered acceptable. In Figure 3.5c, there exists a small deviation in the simulation results post 1.5 kN load. This error is due to the inherent incapability of coarse FE mesh models to exhibit linearity of hyperelastic material at high strains.

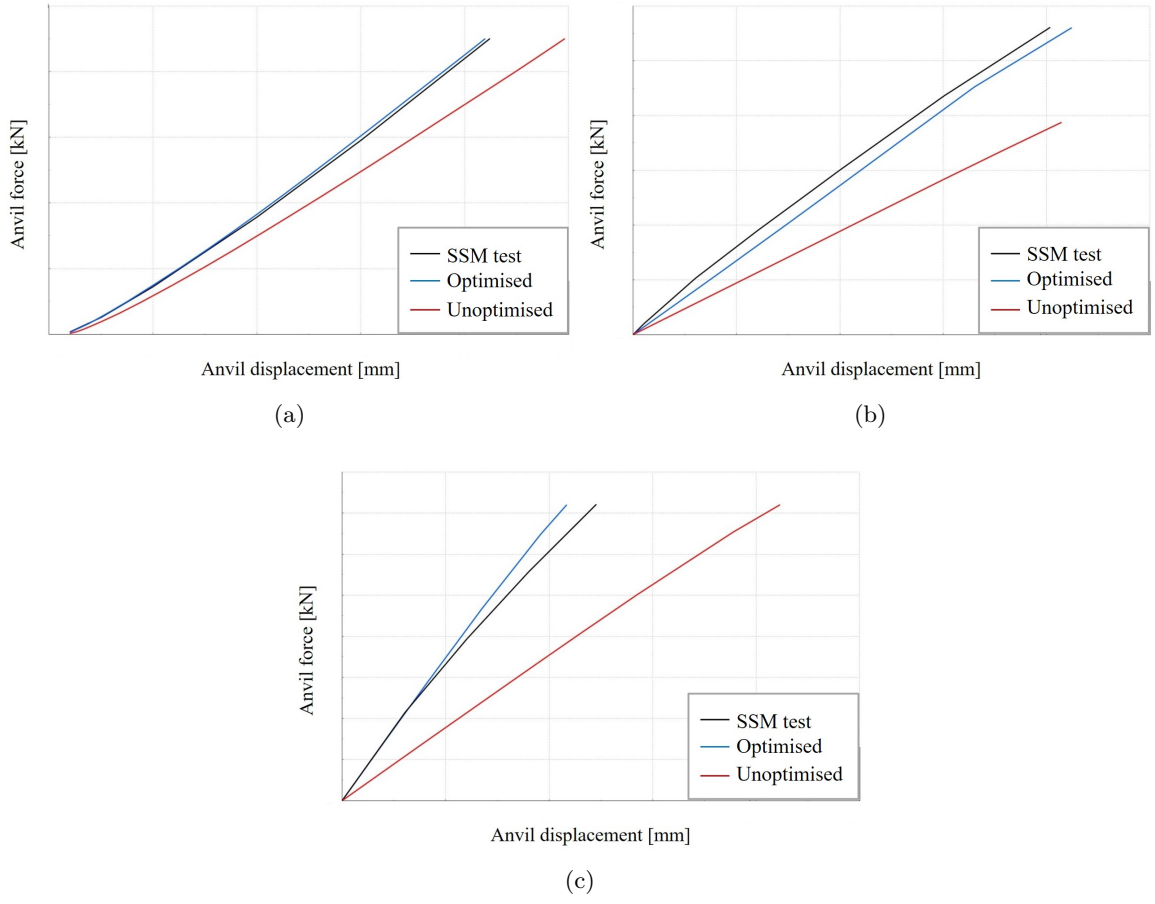

Figure 3.5: Comparison between an unoptimised and optimised model against the tyre response from SSM tests for (a) radial stiffness, (b) lateral stiffness and (c) longitudinal stiffness. The unoptimised model bears a hardness value of 50 (shoreA scale) for all the rubbers as reference. Axis scaling is omitted due to confidentiality.

Table 3.2 provides information about the error in the stiffness values as predicted by the FE models.

Table 3.2: Error (in %) in the tyre stiffness as predicted by the FE model.

Output parameter	Before optimisation	After optimisation
Radial stiffness	12.4	0.94
Lateral stiffness	36.81	6.5
Longitudinal stiffness	35.98	5.2

Cette thèse est accessible à l'adresse : https://theses.insa-lyon.fr/publication/2022ISAL0081/these.pdf
© [B. Anantharamaiah], [2022], INSA Lyon, tous droits réservés

The error is calculated as

$$Error = \text{abs}(A_{test} - A_{sim})/A_{test}, \tag{3.6}$$

where A_{test} and A_{sim} are the areas under the stiffness curves in the test and simulation (both optimised and unoptimized) in Figure 3.5. The errors in Table 3.2 lie in the acceptable limits and can be further reduced by using a fine mesh model during the DoE and optimisation process. However, this leads to a compromise in computational time. From the results, it can be concluded that the hyperelastic behaviour of the rubbers is well characterised for the FE tyre model developed. The similar characterisation procedure can be used to calibrate the viscoelastic properties of the rubbers regions which shall be discussed in the next chapter.
The prime advantage of this methodology is that the rubber materials are characterised (in the local regions of the tyre) based on the overall tyre behaviour, which is not the case in the conventional theoretical implementation of rubber materials in FE simulations.
The individual contribution of each rubber region can be understood from the correlation coefficients as shown in Table 3.3. From the same table, it can be seen that the carcass rubber hyperelasticity influences all the stiffness of the tyre dominantly. This is because the carcass rubber extends from the tyre bead to bead, thus constituting the main component per volume of the tyre. Major contribution towards longitudinal stiffness comes from the cap ply hyperelasticity (other than carcass rubber) since the first principal direction of the ply (refer Figure 3.1) is along the direction of the longitudinal load. The same reason applies for the influence of carcass ply hyperelasticity over the lateral stiffness.

Table 3.3: Correlation coefficients for tyre constituent rubbers vs. tyre stiffness as obtained from the DoE tool. These coefficients describe the relative strength between the input and output variables. The sign indicates the direction of this relationship.

		Input parameters (shoreAs of)							
		Sidewall	Apex	Tread	Carcass	Shoulder-wedge	Rim-cushion	Cap ply factor	Carcass ply factor
Output parameters	Radial stiffness	0.38	0.2	-0.04	0.66	0.36	-0.15	0.11	0.46
	Lateral stiffness	0.27	0.11	-0.13	0.52	0.21	-0.07	0.26	0.77
	Longitudinal stiffness	0.38	0.14	0.07	0.59	0.32	-0.09	0.58	0.24

3.2.1 Tyre modal testing and FE analysis

A good material definition is very important in FE analyses for predicting the dynamic behaviour of a tyre. In this terms, hyperelasticity of rubbers is a key property that regulates the frequencies of tyre Eigen modes. Since the focus in this chapter is on the hyperelastic property of tyre rubbers, its influence over Eigen frequencies of the tyre modes is studied.
In order to study the modal behaviour of the tyre, a free-free modal test setup is developed as shown in Figure 3.6a. As seen from this figure, the tyre is suspended using an elastic band to generate a near free-free condition during the test. The impact points are deployed with mono-axial accelerometers to measure point inertances. Transfer inertances are measured using tri-axial accelerometers along the circumference of the tyre. A close-up view of a set of tri-axial accelerometers at one of the measurement points on the tyre is shown in Figure 3.6b.
The tyre considered in this work has 350 tread points and this means that each tread is offset by approximately 1° from each other. Hence, each tread can be directly numbered based on its angle. An illustration of the tread numbering, the impact and the point inertance points is shown in Figure 3.7. Three points on the tyre are identified for impacting using a hammer with a metal tip. The impact is made only on these points in the direction normal to the tyre

Cette thèse est accessible à l'adresse : https://theses.insa-lyon.fr/publication/2022ISAL0081/these.pdf
© [B. Anantharamaiah], [2022], INSA Lyon, tous droits réservés

surface and the point inertances are measured using five monoaxial accelerometers. The tri-axial accelerometers are used to measure the accelerations at every alternative tread blocks by shifting their positions after each measurement. These measurements are made up to 270° of the tyre.

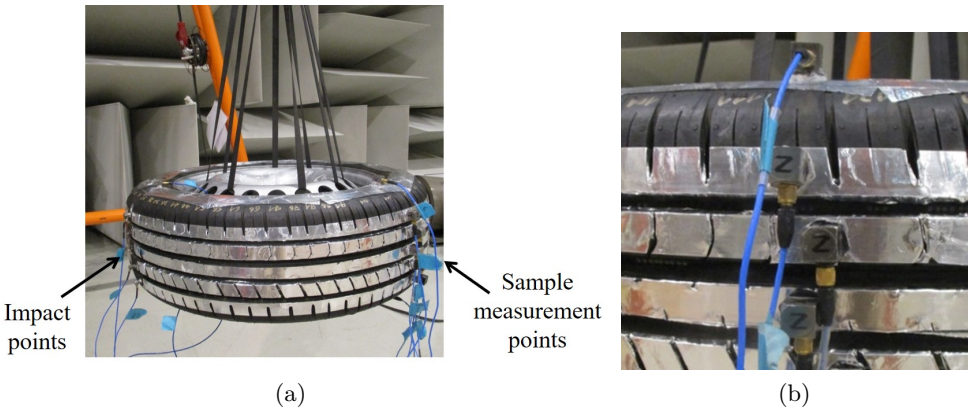

(a) (b)

Figure 3.6: Modal analysis test. (a) A free-free tyre test setup for modal analysis and (b) A sample measurement point on the tyre with tri-axial accelerometers.

Tyre tread numbering

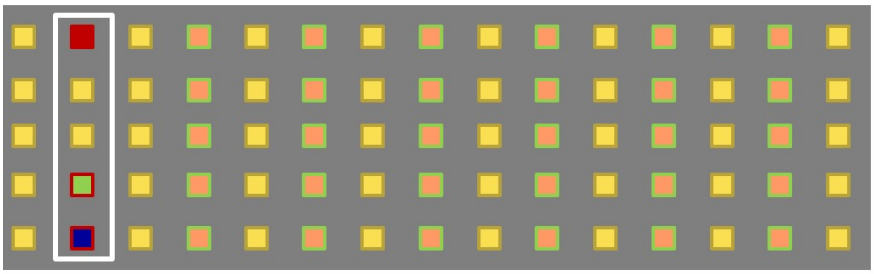

Impact and point inertance measurement points illustration

Point inertance and impact point no. 16

Point inertance and impact point no. 19

Point inertance and impact point no. 20

Dummy (tread) points

Transfer inertance (tread) points

Figure 3.7: An illustration of tread numbering, and identification of impact and measurement points on the tyre. The impact direction is normal to each individual impact point.

Cette thèse est accessible à l'adresse : https://theses.insa-lyon.fr/publication/2022ISAL0081/these.pdf
© [B. Anantharamaiah], [2022], INSA Lyon, tous droits réservés

A sample measurement of point inertances, along with coherence, is shown in Figure 3.8a. Coherence is an indicator of linear relationship between the input and output of the corresponding frequency response. Its value ranges between 0 to 1, with 0 and 1 being unreliable and reliable, respectively. By observing the coherence curve, it can be concluded that the tyre modes from the impact test can be distinguished well up to a frequency of 300 Hz, beyond which the modal density increases and their amplitude decreases. This leads to difficulty in determining the modal damping factor values beyond this frequency range, the use of which is discussed later in this chapter.
Similar to the DoE analysis that was used to estimate the values of rubber shoreAs, another DoE analysis is performed to understand the variations of tyre modal behaviour due to the variation of rubber hardness. However, the DoE study must be restricted to only those modes of the tyre that span up to a maximum of 300 Hz, since the mode shapes beyond this limit cannot be identified in tests with good reliability.

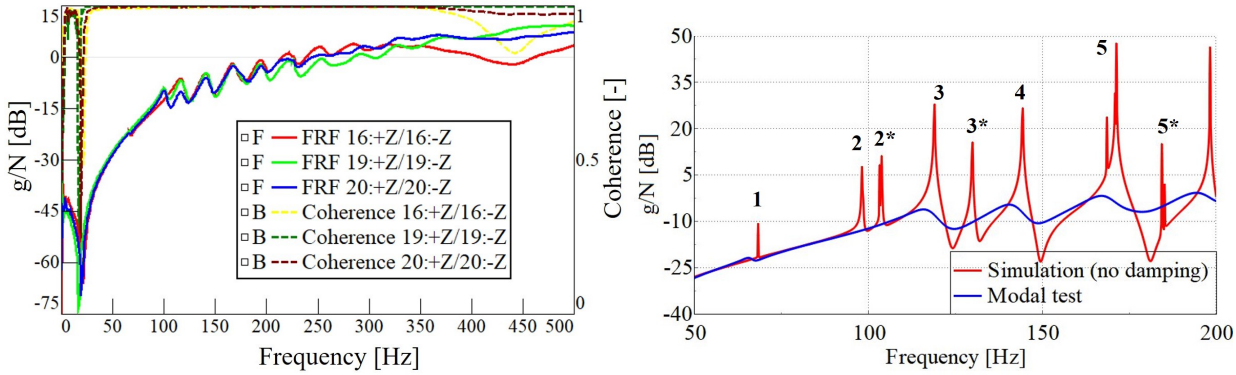

(a) (b)

Figure 3.8: Tyre modal analysis - (a) A sample of measured point inertance behaviour on different points (16, 19 and 20) of the tyre along with coherence of the measurement and (b) Point inertance of tyre without any modal damping. Modes with asterisk, that are observed in simulation only, are not detected in tests due to the naturally occuring damping property of rubber materials. Hence these modes are not considered for the current DoE study.

The identifiable modes of the tyre from the simulation (considered only up to 200 Hz) are shown in Figure 3.8b as a comparison with the tests. It should be noted that the simulation model includes hyperelastic properties of rubbers and not any form of damping, as a result of which the simulation curve is not smooth or damped. The curves are compared with each other to offer reader an idea about the behaviour of the simulation model without any form of damping definitions. In this figure, some of the modes that are observed explicitly in the simulation (and not in test) are identified with the corresponding mode number with an asterisk. The mode shapes are shown in Appendix A.1. The correlation of transfer inertances is shown in Appendix A.3.

3.2.2 Individual rubber contributions to the tyre modes

In the previous section, experimental modal analysis of the tyre was discussed, which gave an understanding that the tyre is a highly damped system and the limit up to which the modes can be distinguished is 300 Hz. However, for the study on the contribution of individual rubber to the overall tyre modal behaviour, the limit is set to 200 Hz in order to avoid any overlap of the considered modes with the high modal density regime that is observed beyond 250 Hz (refer Figure 3.8a). DoE technique is used in this process in which the hardness values (in shoreA) of the six rubbers of the tyre are considered as inputs and the frequency of the Eigen modes as outputs. Input value of each individual rubber hardness is varied by a percentage change in

Cette thèse est accessible à l'adresse : https://theses.insa-lyon.fr/publication/2022ISAL0081/these.pdf
© [B. Anantharamaiah], [2022], INSA Lyon, tous droits réservés

its shoreA values and the corresponding change in the tyre Eigen frequencies are determined. Input parameters can be referred from Figure 3.3. Their lower and upper limits for the DoE study is shown in Table 3.4.

Table 3.4: Rubber hardness sampling limits for modal behaviour study. Initial values shown are normalised. The limits are in terms of percentage of optimised/initial hardness value (in shoreA) of the tyre rubbers.

Parameter	Rubber name	Initial value	Lower limit (%)	Upper limit (%)
ShoreA_sidewall	Sidewall	61.67	-25	50
ShoreA_tread	Tread	62.5	-25	25
ShoreA_apex	Apex	77.05	-25	25
ShoreA_carcass	Carcass	62.5	-50	25
ShoreA_shoulderwedge	Shoulderwedge	48.6	-50	25
ShoreA_rimcushion	Rimcushion	66.67	-25	25

The values for these limits are derived from several pre-run DoEs in which the mode shapes are made to fit inside the acceptable frequency range, i.e 200 Hz, as identified in modal tests. A total of 28 samples (the minimum number of runs required for 6 variables considered [83]) are generated using LHS technique for the purpose of DoE. The results from the DoE study are shown in Table 3.5.

Table 3.5: Results from modal DoE which offers the correlation coefficients between the tyre rubber hardness and the Eigen frequency of the tyre modes. Refer Appendix A.1 for mode numbers and shapes.

		Input parameters (shoreA of)					
		Sidewall	Apex	Tread	Carcass	Shoulderwedge	Rimcushion
Output parameters	Mode 1	0.9	0.3	0.0	0.6	0.0	0.24
	Mode 2	0.5	0.3	0.0	0.8	-0.1	-0.1
	Mode 3	0.6	0.3	0.0	0.8	-0.1	0.15
	mode 4	0.6	0.3	0.0	0.8	-0.1	0.0
	mode 5	0.6	0.3	0.0	0.9	-0.1	-0.2

This table gives the correlation coefficients[†] between the inputs (or rubber hardness) and the output parameters (or the Eigen frequency of the modes). From this table, it can be seen that the hardness of the sidewall and the carcass rubbers of the tyre dominate the tyre modal behaviour. The sidewall rubber hardness influences the lower modes of the tyre, while its influence reduces for the higher modes. However, the influence of carcass hardness is vice-versa. While the influence of the rimcushion and the apex rubber hardness stand trivial in comparison to the sidewall and the carcass rubbers, the tread and the shoulderwedge rubber hardness offer zero or near-zero contribution to the tyre modal behaviour. The reader is referred to Appendix A.1 for mode numbers and shapes.

Apart from understanding the correlation between input and output variables, it is important to understand the degree of their influence on the tyre behaviour. A set of pareto plots for the five Eigen modes considered is shown in Figure A.10 in Appendix A.5. From these plots, it can be seen that the hardness of the sidewall and the carcass rubbers are the major factors that control

[†]The correlation coefficient is a statistical measure of the strength of a relationship between the relative movements of two variables.

Cette thèse est accessible à l'adresse : https://theses.insa-lyon.fr/publication/2022ISAL0081/these.pdf
© [B. Anantharamaiah], [2022], INSA Lyon, tous droits réservés

the overall tyre modal behaviour. The hardness of the sidewall rubber has a dominant influence over the first Eigen mode of the tyre, as displayed in Figure A.10a. On the other hand, the hardness of the carcass rubber dominates the rest of the modes of the tyre. This can be realised from Figures A.10b - A.10e. These pareto plots complement the findings and discussions on the correlation coefficients (in Table 3.5), thus assuring that the modal DoE study is valid and credible.
Hence, from these studies, it can be concluded that the hardness of the tyre carcass rubber is a critical parameter that affects the static as well dynamic behaviour of the tyre. Although the hardness of the sidewall has mediocre influence on the tyre static behaviour, it has a very strong participation in the dynamic behaviour of the tyre.

3.2.3 Test and simulation correlation

The study of tyre FE modal behaviour was discussed without an introduction of any kind of damping, either material or mode based, in the simulation model until now. In order to correlate the tyre simulation results with that of tests, damping in the FE model is necessary and this is introduced in the form of modal damping values. These values are determined from the tyre impact tests using polyreference least-squares complex frequency-domain (p-LSCFD) method in LMS Testlab® software [84] and are as tabulated in Table A.1 in Appendix A.6. In case the viscoelastic properties of rubbers are known, then these can be used as an alternative to the modal damping values. This, however, cannot yet be introduced in this study since the viscoelastic property of these rubber regions needs to be recalibrated. This is because the tyre FE model has been simplified by merging several rubber regions. Figure 3.9 offers a comparison of point inertance measured from tests and simulations for a hammer impact on points 16, 19 and 20 of the tyre. Refer Figure 3.7 for the locations of impact points.

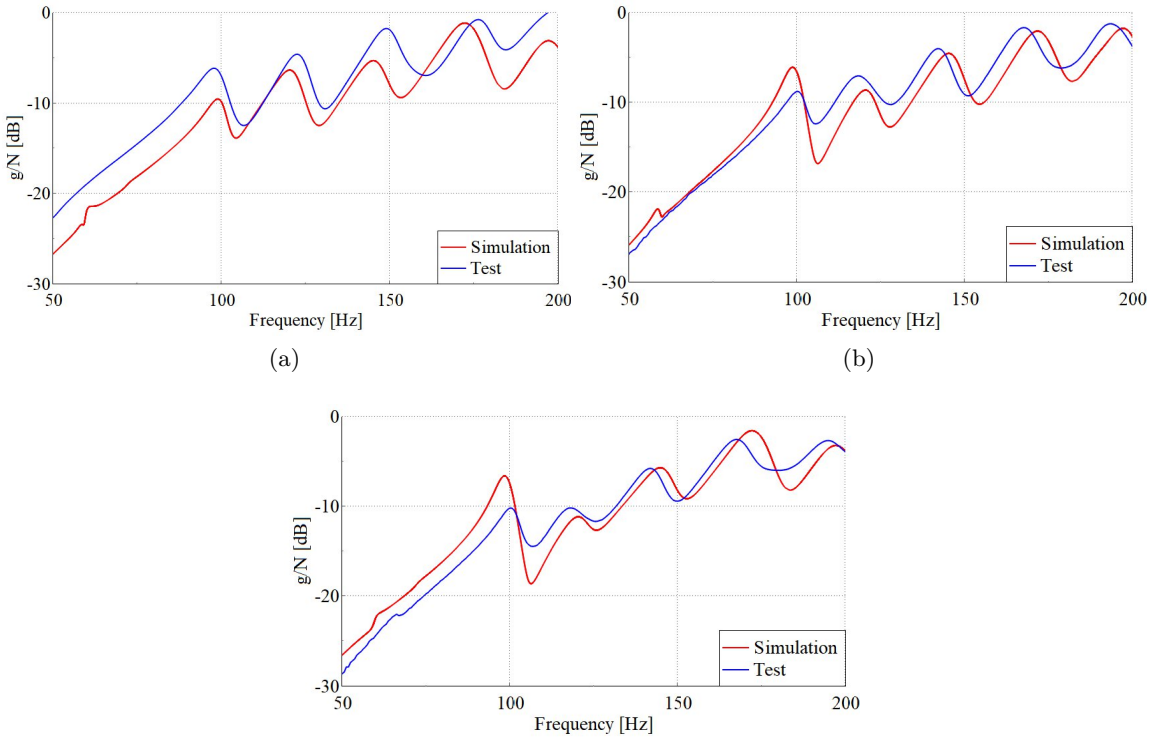

Figure 3.9: Point inertance comparison between modal test and simulation - (a) for point 16, (b) for point 19 and (c) for point 20. Refer Figure 3.7 for points location.

Cette thèse est accessible à l'adresse : https://theses.insa-lyon.fr/publication/2022ISAL0081/these.pdf
© [B. Anantharamaiah], [2022], INSA Lyon, tous droits réservés

From Figure 3.9, it can be observed that there is a good match between the modal test and simulation results (the criteria considered to judge the conditions for the match is elucidated in Appendix A Section A.2). This implies that the methodology used in this work to estimate the rubber hardness (in shoreAs) in order to model the tyre overall performance is prolific.
From Figure 3.9b the modal simulation predicts a mode at 66 Hz which is not "significantly" observable in the test. However, this mode is also observed in the test but its amplitude is very negligible. The reason for the negligible (detection of) amplitude of this mode in test lies in the fact that the measured mode has displacements in the tyre axial direction (refer Appendix A Figure A.1). A monoaxial accelerometer, that measures the radial displacements, is used to measure this axial mode due to which this accelerometer is not capable to detect the mode. The same behaviour is observed in Figure 3.9a. However, in Figure 3.9c the impact location is at the bottom end of the tyre (Refer Figure 3.7 for points location) which can be imagined as the outer end of a cantilever beam which is stiffer at point 16 than at point 20 due to the non-symmetric design of rim. This induces both radial and axial displacements in the tyre which are associated to the same axial mode (i.e. for this mode, even thought it is axial, it also exhibits noticeable levels of radial vibration).
From Figures 3.10a and 3.10b, it can be clearly observed that the change in the hardness of the carcass and the sidewall rubbers, respectively influence the Eigen frequencies of tyre modes by a larger extent than that of change in the hardness of the tread and the rimcushion rubbers (Figures 3.10c and 3.10d). This is exactly the behaviour predicted by modal DoE. To conclude, the rubber hyperelasticities predicted by the DoE technique is describing the modal behaviour of the tyre effectively.

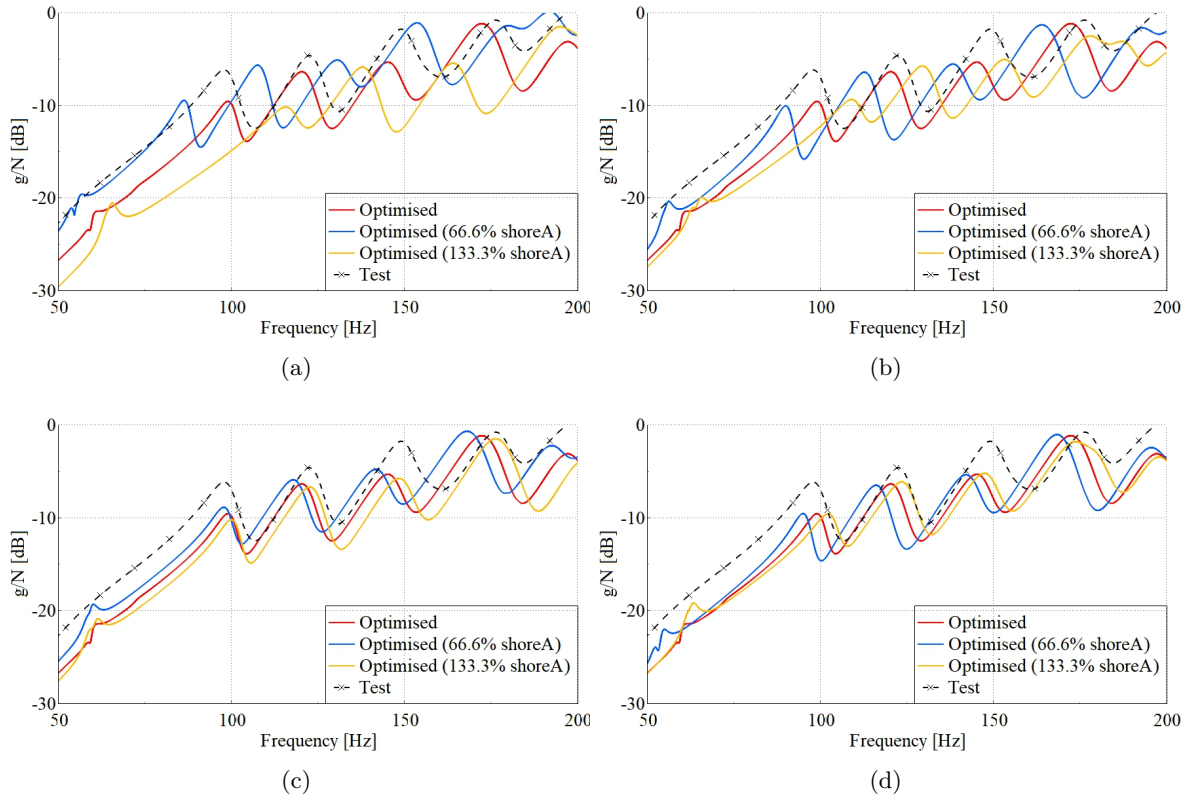

Figure 3.10: Influence of hardness (in shoreA) on the tyre point inertance (for impact on point 16) of the free-free tyre. (a) Carcass rubber influence, (b) sidewall rubber influence, (c) tread rubber influence and (d) rimcushion hardness influence. The unusual rubber hardness percentage variation (in shoreA) is due to the next available lowest and highest values of the shoreAs of rubbers from the optimised value.

Cette thèse est accessible à l'adresse : https://theses.insa-lyon.fr/publication/2022ISAL0081/these.pdf
© [B. Anantharamaiah], [2022], INSA Lyon, tous droits réservés

3.2.4 Noise generation and propagation study

Noise generation and propagation is a study subsequent to tyre modal analysis. In previous sections, a free-free tyre setup is impacted using a hammer and the displacements of external points on the tyre are measured using accelerometers. In this section, the setup and the results from noise FE simulations are discussed.
In the noise generation study, the same tyre is impacted (with a hammer) on the same points as described in Figure 3.7. The propagation of noise generated or NTFs are measured using microphones as shown in Figure 3.11a. Two microphones M1 and M2 are used for tests and their placements are as shown in Figure 3.11b. On the similar lines to tyre noise tests, tyre FE noise simulation model is also setup. The procedure of FE noise propagation is based on sequentially coupled submodelling analysis technique (available in commercial FE analysis software packages).

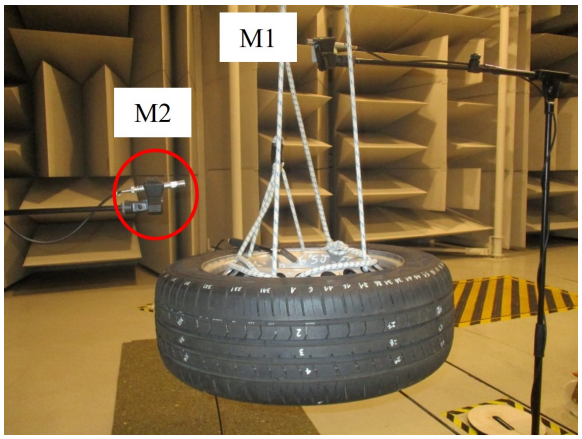

(a)

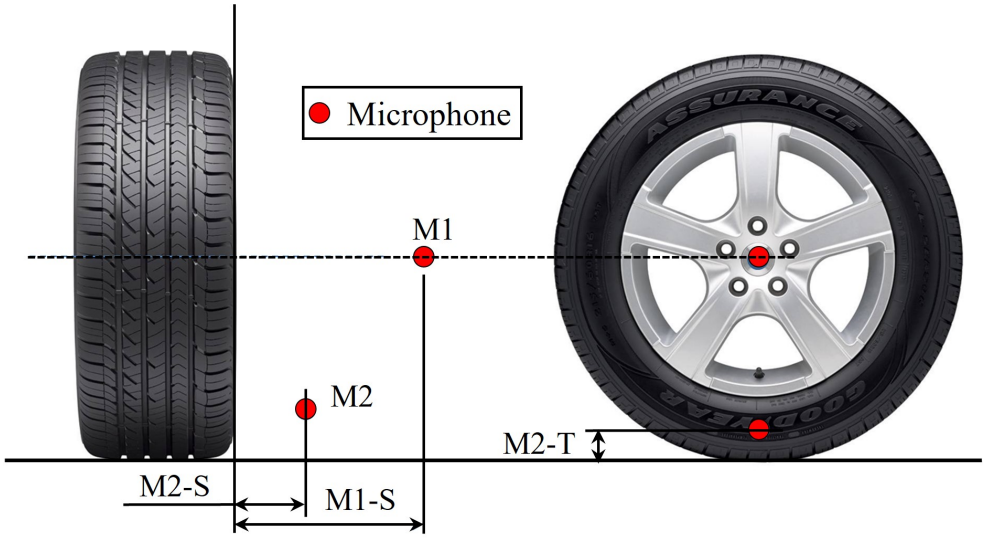

(b)

Figure 3.11: Free-free tyre setup for noise generation and propagation - (a) experimental setup at the hemi-anechoic chamber in Idiada and (b) microphone positions for the measurements. M1-S = 0.5 m, M2-S = 0.15 m and M2-T = 0.06 m.

A schematic description of this technique is shown in Figure 3.12. In this figure, the global model involves the mechanisms that generate tyre noise, which in this study corresponds to the modal FE model of the tyre. The output from the global model is the corresponding nodal displacements of the tyre. This output from the global model is then utilised as a boundary

Cette thèse est accessible à l'adresse : https://theses.insa-lyon.fr/publication/2022ISAL0081/these.pdf
© [B. Anantharamaiah], [2022], INSA Lyon, tous droits réservés

condition in the submodel analysis in which the acoustic or noise propagation is simulated. A snap of global model, submodel and acoustic wave propagation as developed in an FE modelling software is shown in Figure 3.13. Microphones in this FE model are modelled as sensor points (not shown in the figure) to measure acoustic pressure variations or NTFs. These variations are due to perturbations in the acoustic medium that are caused by the nodal displacements of the global model. The position of these sensor points are the same as that of the experiment shown in Figure 3.11(b).

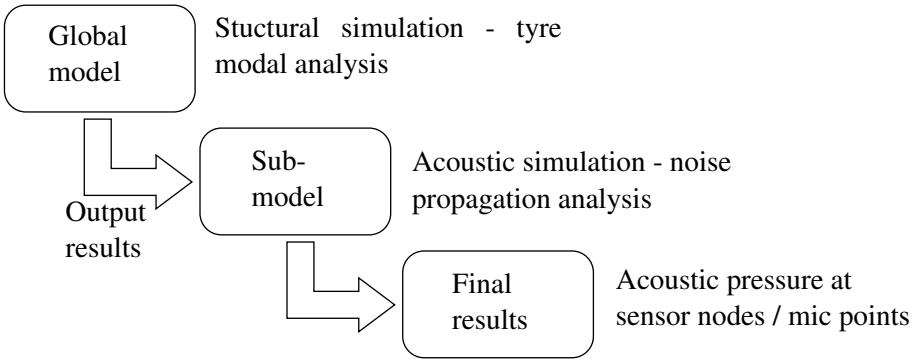

Figure 3.12: Sequentially coupled submodelling technique for tyre FE noise simulations.

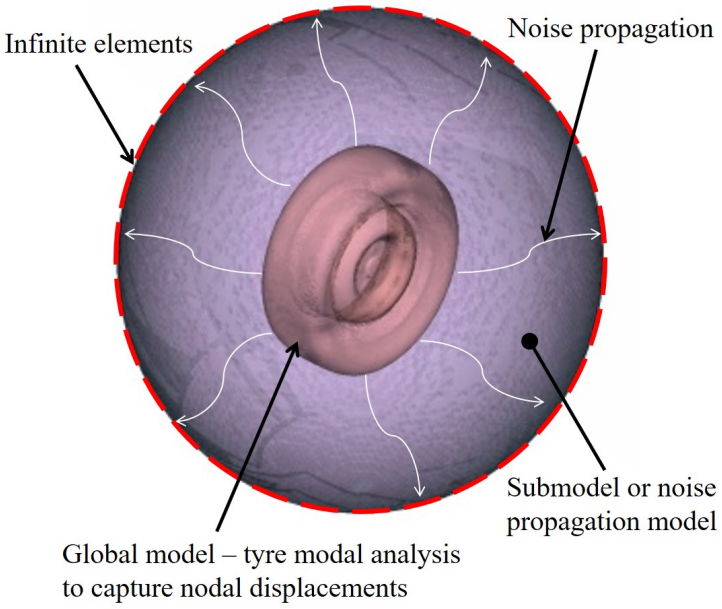

Figure 3.13: FE model of the sequentially coupled analysis for tyre noise modelling.

3.3 Results and discussions

To assess the reliability of the FE model, the NTF from test and simulation must be compared with each other. The noise measurement test involves two microphones M1 and M2 for NTF measurements (refer Figure 3.11a) of which only M2 is considered for the comparison. Figure 3.14 shows a comparison between the simulation and test results. From this figure, it can be seen that there is a good match between the NTF levels, however, the measurements are reliable beyond, approximately, 75 Hz as indicated by coherence curves. In Figure 3.14a, an offset in NTF peaks can be observed for an impact on point 16, the reason for which has to be understood.

Cette thèse est accessible à l'adresse : https://theses.insa-lyon.fr/publication/2022ISAL0081/these.pdf
© [B. Anantharamaiah], [2022], INSA Lyon, tous droits réservés

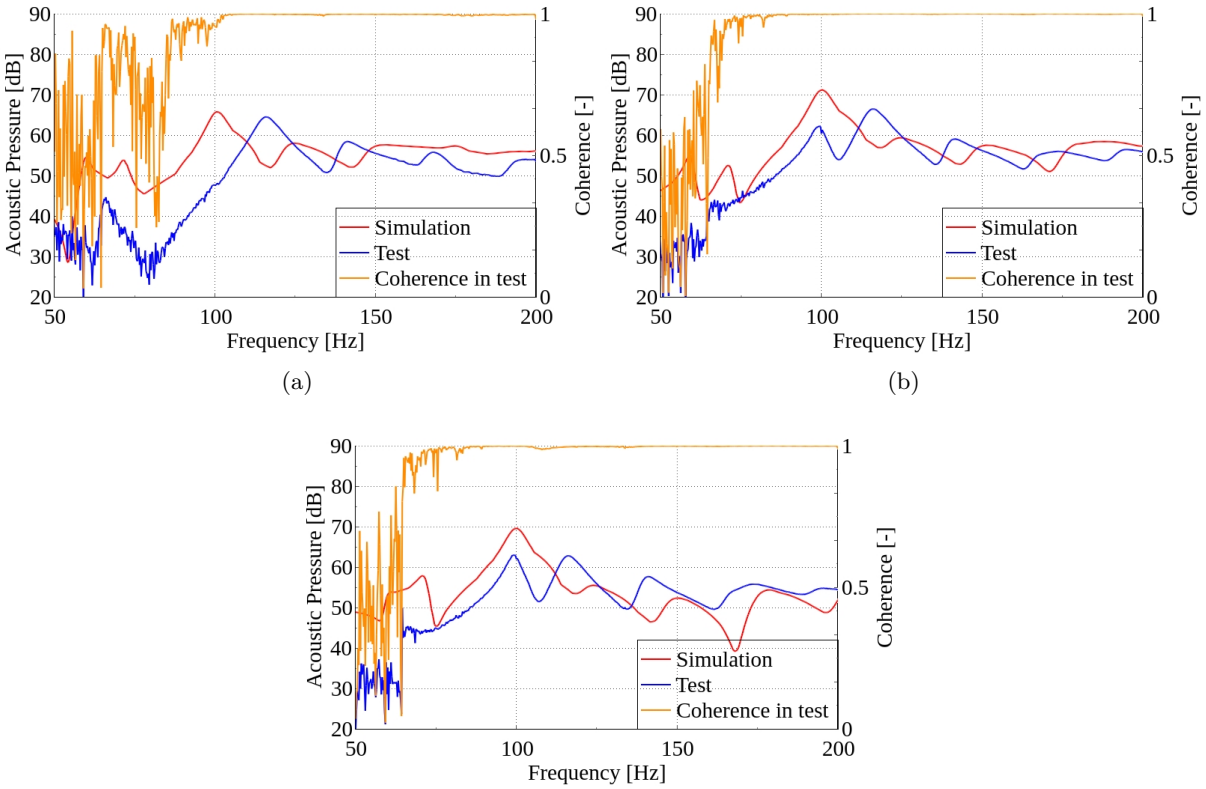

Figure 3.14: Noise transfer function comparison between test and simulation - (a) for point 16, (b) for point 19 and (c) for point 20. Refer Figure 3.7 for the location of impact points. NTF from microphone M2 is considered for this study. Coherence in measurements is good beyond 80 Hz. Refer Figure 3.11 for the microphone positions.

The relevant TIs associated with the impact on point 16 of the tyre is shown in Appendix A.1 Figure A.8. The microphone in the test is placed just above the impact point 16 and in the sidewall region of the tyre as shown in Figure 3.11. In Figures A.8a and A.8e (in Appendix A.1) it can be observed that the twisting mode in the simulation at 100 Hz is dormant in the tests. Although, this mode is detected in other locations of the tyre (refer Figures A.8b-A.8d in Appendix A.1) in the tests, the amplitude is negligible or at least 20 dB lower than the simulation. This dormancy and low level of detection of twisting mode is leading to a case in which the twisting mode at 100 Hz and the following radial mode at 118 Hz are mutually interfering with each other. This interference is leading to a combined mode in the NTF as seen in Figure 3.14a. Note that this only happens in the test.

In addition to the study of the influence of hardness on tyre point inertances (as in Figure 3.10), it is also important and interesting to study the same on tyre NTFs. The same models that were studied for point inertances are considered in NTF simulations. The effect of the hardness of the carcass, the sidewall, the tread and the rimcushion rubber on the tyre NTF are shown in Figure 3.15. Impact is on point 16 (Refer Figure 3.7). The NTF is measured at microphone, M2, whose location is shown in Figure 3.11.

All the observations and discussions that are evident for the dependance of Eigen frequencies on rubber hardness (refer Figure 3.15 and its corresponding discussion) are still relevant for the dependance of tyre NTFs on rubber hardness. From Figures 3.15a and 3.15b, it can be clearly observed that a change in the hardness of the carcass and the sidewall rubbers influences the

Cette thèse est accessible à l'adresse : https://theses.insa-lyon.fr/publication/2022ISAL0081/these.pdf
© [B. Anantharamaiah], [2022], INSA Lyon, tous droits réservés

NTF to a larger extent than that of the tread and the rimcushion rubbers (Figures 3.15c and 3.15d). This means that the DoE technique used for the calibration of rubber hyperelasticity not only helps in the development of an FE model to study its Eigen mode dynamics but also assists in fine tuning the NTF (and thus noise) when the model is incorporated with appropriate damping values.

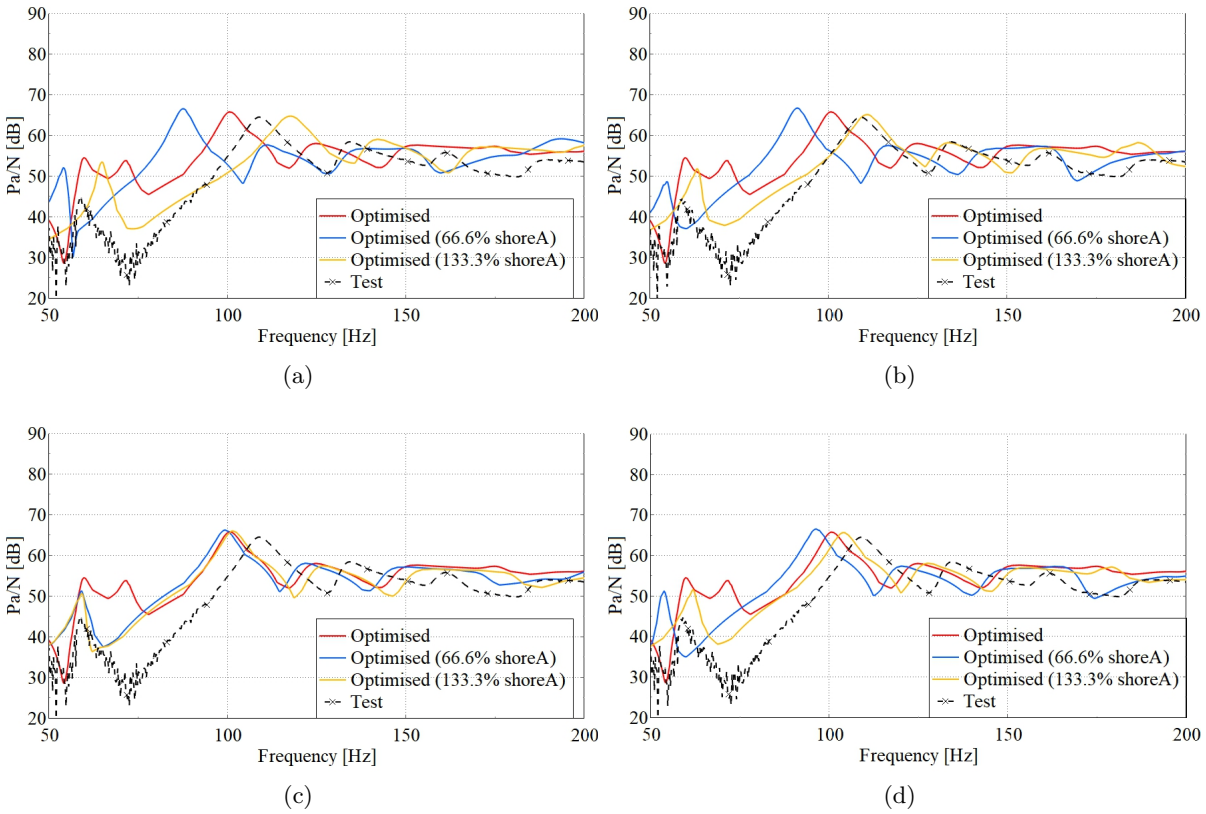

Figure 3.15: Variation in the free-free tyre NTF due to variations in (a) carcass hardness, (b) sidewall hardness, (c) tread hardness and (d) rimcushion hardness. Impact is on point 16 (Refer Figure 3.7). Refer Figure 3.11 for the microphone position.

3.4 Conclusions

In this chapter, an innovative and simplified tyre axi-model was developed that takes into account the behaviour of the individual components of a tyre due to its manufacturing variability. The tyre axi-model was simplified based on the degree of the local dominance of each rubber of the tyre based on the information shared by the tyre manufacturer. Tyre static behaviour, i.e. radial, lateral and longitudinal stiffness were measured on an SSM machine and a replicative FE simulation model was developed. LHS technique was used to generate several tyre FE model samples with varying rubber hardness. A DoE study was performed in which all the tyre FE model samples were simulated and the corresponding static behaviour in each of these was compared against the tyre static tests. Among these samples, a tyre model, with optimised individual rubber hardness, that matches the test behaviour results was determined. Using this optimised tyre rubber model, DoE was again implemented to understand the contribution of constituent rubbers to the overall dynamic behaviour of the tyre. In these models, the damping was defined in the form of modal damping values determined from modal tests. This approach offers a systematic segregation of the contribution of individual rubber regions to the frequencies of the tyre Eigen modes.

Cette thèse est accessible à l'adresse : https://theses.insa-lyon.fr/publication/2022ISAL0081/these.pdf
© [B. Anantharamaiah], [2022], INSA Lyon, tous droits réservés

From the tyre static behaviour study, it was found that the hardness of the carcass rubber dominates the overall tyre stiffness for two reasons - (a) carcass rubber runs between bead to bead of the tyre, thus forming a skeleton of the tyre and (b) it is the main component per volume of the tyre. Carcass plies hyperelasticity influence the tyre radial and lateral stiffness, whereas the cap plies influences the tyre lateral stiffness. This is due to their stiffening effects in the corresponding loading directions. The shoulderwedge and the sidewall rubber hardness induce mediocre effect on the tyre static behaviour whereas tread, apex and rimcushion rubber hardness impart trivial influence.

Tyre dynamic behaviour study showed that the key contributors for the tyre Eigen modes are the carcass and the sidewall rubbers hardness. From the DoE results, theoretically it was found that the hardness of the carcass rubber dominates the Eigen frequency of tyre modes at higher frequencies, whereas the hardness of the sidewall rubber dominates the lower ones. The contribution of the hardness of the apex and the rimcushion rubber was negligible, while the tread and the hardness of the shoulderwedge rubber made no contribution to the tyre modal behaviour.

It is important to note that tyre modal density increases considerably beyond 300 Hz. Although the rubber hyperelasticity is sufficient to identify the Eigen frequencies of the tyre modes up to 300 Hz, the definition of the damping property of the rubbers is essential to model the tyre dynamic behaviour beyond it. On one hand, modal damping values from the modal test provide the damping information in a straightforward step, on the other hand, these values are hard to identify from the tests beyond 250 Hz - 300 Hz; again, due to the problem of high modal density. In case the aim is to model the same tyre for higher frequency analyses, it is advisable to estimate and introduce the viscoelastic definitions of rubbers. The estimation of rubber viscoelastic property can be performed by calculating the Prony parameters and this procedure will be discussed in the following chapter.

Cette thèse est accessible à l'adresse : https://theses.insa-lyon.fr/publication/2022ISAL0081/these.pdf
© [B. Anantharamaiah], [2022], INSA Lyon, tous droits réservés

4

Calibration of tyre rubber viscolelasticity

HYPERELASTICITY and viscoelasticity are the most important properties of a material, especially rubbers, post the elastic limit. A brief introduction about tyre rubber material properties and their theoretical expression is offered in Section 1.3. Hyperelastic calibration of various rubbers of the tyre has been discussed already in the previous chapter. As a step further, it is necessary to calibrate the viscoelastic part of the rubbers since this material regime defines the damping of rubber materials. The behaviour of basic material viscoelasticity is best represented by equivalent model consisting of a spring and a dashpot. Although several models of linear viscoelasticity exist, a few models are shown in Figure 4.1. For more information, the reader is referred to [85]. It is to be noted that this work is not aimed at carrying out fundamental research in the field of rubber viscoelasticity. Instead, it aims at implementing a method of characterising the rubber viscoelasticies.

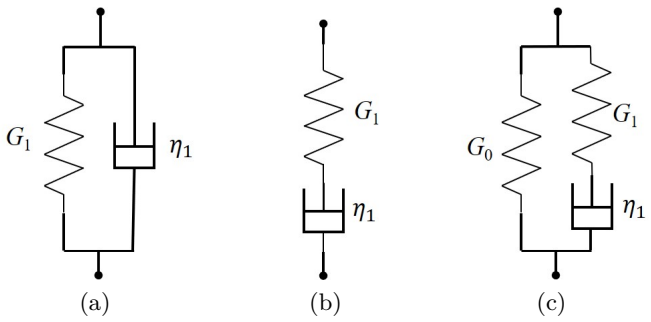

Figure 4.1: Common models for linear viscoelastic materials - (a) Kevin-Voigt (b) Maxwell and (c) Zener. G_1, G_0 and η_1 represent the bulk modulus, the relaxed shear modulus and the viscosity coefficient or the loss factor, respectively.

4.1 Dynamic mechanical analysis and material rheology

Rubbers are polymers that need special tests for determining their mechanical and dynamic characteristics. Quasi-static Tension and shear tests are very basic and can only define the static behaviour of rubbers which is not sufficient to predict the rubber dynamic behaviour. Through dynamic tests, the frequency dependant behaviour of rubbers can be calibrated. These tests are known as dynamic mechanical analyses (DMA), in which a rubber specimen is subjected to a series of forced oscillations or temperatures or both and the corresponding responses, e.g. dynamic stress or dynamic strain of the rubbers are measured [86].
Material rheology involves the application of continuum mechanics to charaterise the material

Cette thèse est accessible à l'adresse : https://theses.insa-lyon.fr/publication/2022ISAL0081/these.pdf
© [B. Anantharamaiah], [2022], INSA Lyon, tous droits réservés

behaviour, especially the combination of hyperelasticity and viscoelasticity of the material that has been tested using DMA technique. The rubber DMA data is important to incorporate in the current work since the point inertance of the tyre is damped excessively at higher frequencies as observed in the previous chapter (refer Figure 3.8a). This leads to difficulty in characterising rubber behaviour for higher frequencies and thus the development of high frequency noise FE models.
By subjecting the rubber to DMA, complex modulus is determined that is different from the conventional Young's modulus. Young's modulus restricts itself to define a relation between the material stress and strain only. However, complex modulus describes the rubber's ability to store and lose energy which in turn determines its damping properties. This section lays foundation to the common terms used in DMA tests.

4.1.1 Stress relaxation function

Considering the instantaneous force $F(t)$ acting on a system modelled by a single Maxwell model (refer Figure 4.1b) as shown in Figure 4.2, the stress relaxation function is expressed as [87, 85]

$$\boldsymbol{\sigma}(t) = \boldsymbol{\gamma}_0 \ \boldsymbol{G}(t)\ e^{\frac{-t}{\tau_1}}, \tag{4.1}$$

where $\boldsymbol{\sigma}$(t), $\boldsymbol{\gamma}_0$ and τ_1 are the time dependent stress relaxation term, initial constant shear strain and time relaxation term, respectively. τ_1 is defined as

$$\tau_1 = \frac{G_1}{\eta_1}. \tag{4.2}$$

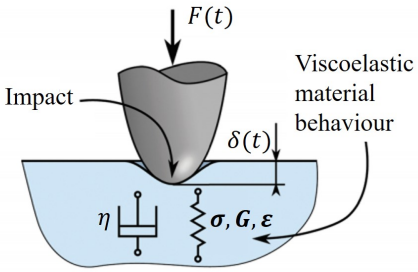

Figure 4.2: A sample representation of a system comprising of a single Maxwell model under the influence of an impact force $F(t)$. Image reference [88].

In real scenarios and industrial application, a single Maxwell element model is insufficient to describe the exact material behaviour and hence a generalised Maxwell (GM) model is employed. A GM model comprises of several springs and dashpots as shown in Figure 4.4.

4.1.2 Storage and loss moduli for a generalised Maxwell viscoelastic material

The fundamental principle to describe stress in linear viscoelastic materials is derived from the Boltzmann's superposition principle [89, 90]

$$\boldsymbol{\sigma}(t) = \int_{-\infty}^{t} G_{\text{rel}}(t-\tau)\frac{\partial \boldsymbol{\epsilon}}{\partial \tau}\mathrm{d}\tau, \tag{4.3}$$

where G_{rel} is the linear shear relaxation modulus and $\boldsymbol{\epsilon}$ is the strain tensor.
To model the strain function as shown in Figure 4.3b, Equation 4.3 is employed as

$$\boldsymbol{\sigma}(t) = \int_{0}^{t} G_{\text{rel}}(t-\tau)\frac{\partial \boldsymbol{\epsilon}}{\partial \tau}\mathrm{d}\tau. \tag{4.4}$$

Cette thèse est accessible à l'adresse : https://theses.insa-lyon.fr/publication/2022ISAL0081/these.pdf
© [B. Anantharamaiah], [2022], INSA Lyon, tous droits réservés

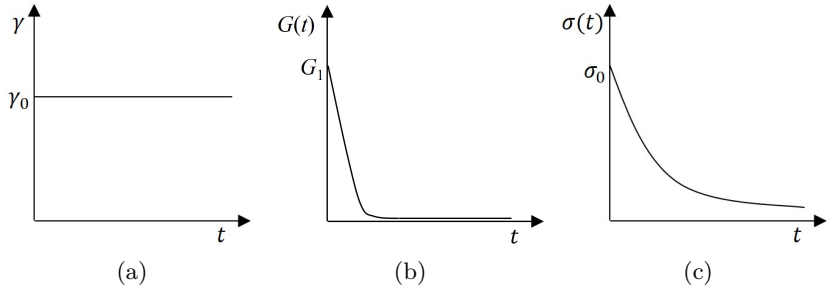

Figure 4.3: Description of viscoelastic material models - (a) applied shear strain, (b) time dependent shear modulus and (c) time dependent stress relaxation.

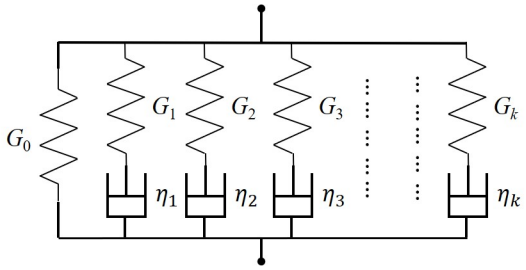

Figure 4.4: A generalised Maxwell (GM) viscoelasticity model.

On applying the Laplace transform, the above equation can be formulated as

$$\tilde{\boldsymbol{\sigma}}(s) = s\tilde{G}_{\mathrm{rel}}(s)\tilde{\boldsymbol{\epsilon}}(s), \tag{4.5}$$

where Laplace transforms of stress and strain (with variable s) are denoted by $\tilde{\boldsymbol{\sigma}}$ and $\tilde{\boldsymbol{\epsilon}}$, respectively. From these two terms, the complex shear modulus is defined as

$$\boldsymbol{G}^*(s) = \frac{\tilde{\boldsymbol{\sigma}}(s)}{\tilde{\boldsymbol{\epsilon}}(s)}. \tag{4.6}$$

On expressing the imaginary variable s as $j\boldsymbol{\omega}$ ($\boldsymbol{\omega}$ being the circular frequency and j the complex number defined by $\sqrt{-1}$) and, substituting Equation 4.5 in Equation 4.6 and expanding, the complex shear modulus can be deduced as

$$\boldsymbol{G}^*(j\boldsymbol{\omega}) = j\boldsymbol{\omega}\tilde{G}_{\mathrm{rel}}(j\boldsymbol{\omega}) = j\boldsymbol{\omega}\int_0^\infty G_{\mathrm{rel}}(\tau')exp(-j\boldsymbol{\omega}\tau')d\tau'. \tag{4.7}$$

In the above equation, it can be observed that $\boldsymbol{G}^*(j\boldsymbol{\omega})$ bears a complex form. This complex form is known as the *complex modulus* or *dynamic modulus* expressed as

$$\boldsymbol{G}^*(j\boldsymbol{\omega}) = \boldsymbol{G}'(\boldsymbol{\omega}) + j\boldsymbol{G}''(\boldsymbol{\omega}), \tag{4.8}$$

where $\boldsymbol{G}'(\boldsymbol{\omega})$ and $\boldsymbol{G}''(\boldsymbol{\omega})$ are the shear *storage modulus* and *loss modulus*, respectively. Now, upon reformulating the relaxation term in the Equation 4.3 in terms of discrete sets of exponential decays as

$$G_{\mathrm{rel}}(t) = G_\infty + \sum_{i=1}^{N} G_i exp(-t/\tau_i), \tag{4.9}$$

Cette thèse est accessible à l'adresse : https://theses.insa-lyon.fr/publication/2022ISAL0081/these.pdf
© [B. Anantharamaiah], [2022], INSA Lyon, tous droits réservés

and from Equation 4.7, Equation 4.8 is expressed as

$$\boldsymbol{G}^*(j\omega) = G_\infty + \sum_{i=1}^{N} G_i \frac{\tau_i j\boldsymbol{\omega}}{1+\tau_i j\boldsymbol{\omega}}, \tag{4.10}$$

where, G_i is the rigidity modulus of each spring (relaxation mode) of the GM model (refer Figure 4.4), $i = 1, 2..\ N$, with N relaxation modes and G_∞ the *relaxed long term modulus* which is defined as the shear modulus of a material when it is at completely relaxed condition. By the properties of complex numbers, the loss and storage moduli can be expressed as

$$\boldsymbol{G}'(\boldsymbol{\omega}) = \Re\{\boldsymbol{G}^*\} = G_\infty + \sum_{i=1}^{N} G_i \frac{(\tau_i\boldsymbol{\omega})^2}{1+(\tau_i\boldsymbol{\omega})^2}, \tag{4.11}$$

$$\boldsymbol{G}''(\boldsymbol{\omega}) = \Im\{\boldsymbol{G}^*\} = \sum_{i=1}^{N} G_i \frac{(\tau_i\boldsymbol{\omega})}{1+(\tau_i\boldsymbol{\omega})^2}. \tag{4.12}$$

Although the above equations describe the storage and loss moduli in terms relaxed long term modulus, practically the evolution of these moduli are measured in the experiments using *unrelaxed long term modulus* or G_0. The relationships between G_0, G_i and G_∞ are defined in terms of the Prony coefficient, g_i as

$$G_\infty = G_0 - \sum_{i=1}^{N} G_i \text{ and } g_i = \frac{G_i}{G_0}. \tag{4.13}$$

Up on substituting the above equation in Equations 4.11 and 4.12 and simplifying the following relationships can be established.

$$\boldsymbol{G}'(\boldsymbol{\omega}) = G_0[1 - \sum_{i=1}^{N} g_i] + G_0 \sum_{i=1}^{N} g_i \frac{(\tau_i\boldsymbol{\omega})^2}{1+(\tau_i\boldsymbol{\omega})^2}, \tag{4.14}$$

$$\boldsymbol{G}''(\boldsymbol{\omega}) = G_0 \sum_{i=1}^{N} g_i \frac{(\tau_i\boldsymbol{\omega})}{1+(\tau_i\boldsymbol{\omega})^2}. \tag{4.15}$$

The unrelaxed long term modulus can be defined as the material modulus that is exhibited when an instantaneous load is applied on the material so that the time-dependent processes have insufficient time to let material undergo relaxation. The above equations are particularly important with respect to experimental, theoretical and computational problems. The relation between G_0 and G_∞ is shown in Figure 4.5a.

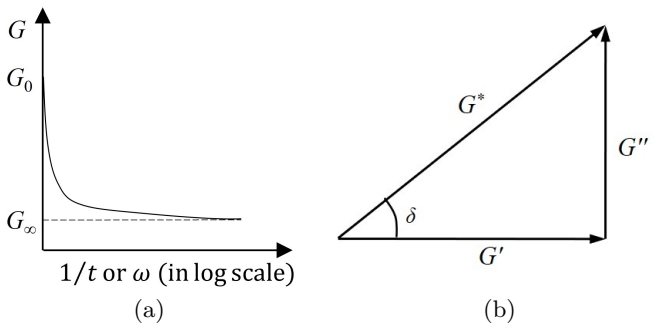

(a) (b)

Figure 4.5: Description of viscoelastic material models (a) Graphical representation of relationship between relaxed and unrelaxed long term moduli and (b) Phasor diagram depicting the relationship between $\boldsymbol{G*}$, $\boldsymbol{G}'$ and $\boldsymbol{G}''$.

Cette thèse est accessible à l'adresse : https://theses.insa-lyon.fr/publication/2022ISAL0081/these.pdf
© [B. Anantharamaiah], [2022], INSA Lyon, tous droits réservés

The relation between complex modulus, storage modulus and loss modulus that are deduced in Equations 4.10, 4.14 and 4.15, respectively are represented as a phasor diagram in Figure 4.5b [91]. In this figure the phasor angle or loss angle or the Prony delta δ represents the lag between the generated stress and material response (strain). Graphically, the interpretation of phase angle is best shown in Figure 4.6a [91]. It should be noted that the applied stress continues to be sinusoidal if the regime of loading is within the linear viscoelasticity. In case there is no considerable lag in the stress and strain curves, then the loading state has not activated the material viscoelasticity regime. However, in linear viscoelastic limit, the greater the δ, the greater is the influence of the material viscoelasticity on the system. This is a corollary that the magnitude of $\boldsymbol{G}''$ is higher for larger values of δ.
It is important to know the practical implications of $\boldsymbol{G}'$ and $\boldsymbol{G}''$. The storage modulus as expressed in Equation 4.14 defines the elastic or hyperelastic part of the material property. Loss modulus (Equation 4.15) characterises the viscoelastic material behaviour. Now, referring to Figure 4.5b, the following relations can be deduced between the storage, loss and complex moduli

$$\boldsymbol{G}' = \boldsymbol{G}^* cos(\delta), \tag{4.16}$$

$$\boldsymbol{G}'' = \boldsymbol{G}^* sin(\delta), \tag{4.17}$$

$$tan(\delta) = \boldsymbol{G}''/\boldsymbol{G}', \tag{4.18}$$

where $tan(\delta)$ (δ in degrees) is known as the loss tangent. A general behaviour of a complex modulus plot is shown in Figure 4.6b.

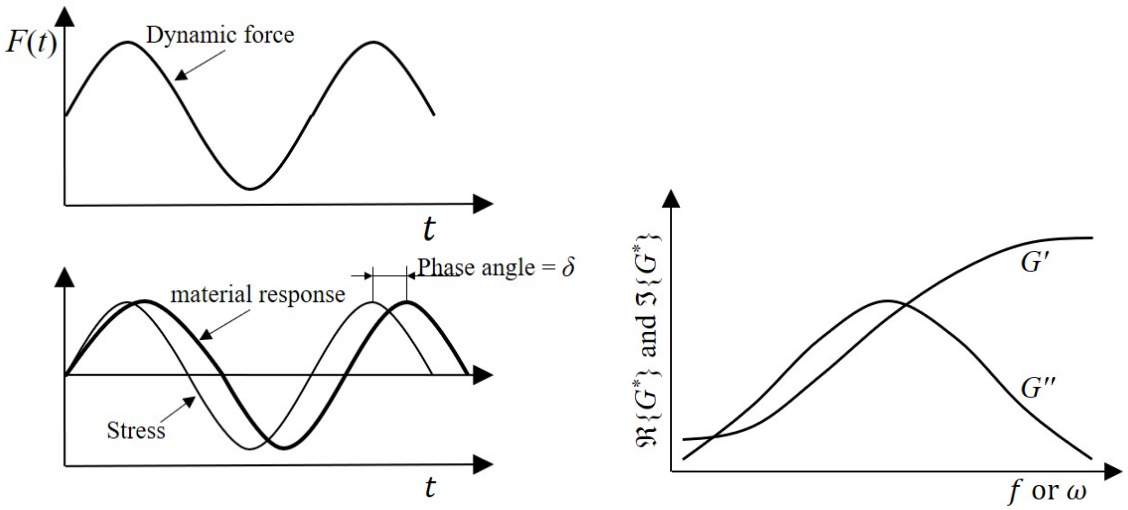

(a) (b)

Figure 4.6: Characteristics of a viscoelastic material. (a) Graphical example to represent the phase angle δ between the applied stress and material response, e.g. strain. Image reference [91]. (b) A general behaviour of the complex modulus for a viscoelastic material [90].

In chapter 3, the calibration of rubber hyperelasticities was performed based on the shore hardness of the rubbers. This in turn means that the storage modulus has been successfully calibrated. In this chapter, the rubber viscoelasticities are determined by estimating the Prony coefficients g_i using curve fitting techniques. This is because, Abaqus® software supports the definition of material viscoelasticity using the Prony series in terms of Equations 4.14 and 4.15 [12].

Cette thèse est accessible à l'adresse : https://theses.insa-lyon.fr/publication/2022ISAL0081/these.pdf
© [B. Anantharamaiah], [2022], INSA Lyon, tous droits réservés

4.2 Viscoelasticity characterisation

As discussed in the previous section, the Prony parameter fitting for DMA test data is necessary to estimate rubber viscoelasticity. In literature, a standard procedure already exists involving the excitation of rubbers under dynamic forces followed by the determination of rubber viscoelasticity by curve fitting of resulting experimental curves [91, 92, 93]. However, these works explain the estimation of the Prony coefficients for every rubber. In case of the tyre considered in this work, performing a DMA test for every rubber (which is vulcanised) is time consuming and is not economical. This is because, such DMA tests must be performed on every rubber samples with a certain geometry defined by relevant testing standards. This sample dimensions cannot be obtained from a real tyre.
Hence, a workaround is to establish a theoretical equation that describes the behaviour of the Prony delta as a function of rubber hardness or shoreAs. As previously mentioned, this theoretical equation has been already determined at IDIADA from the DMA data of various vulcanised rubbers that were tested. In these tests, the variation of δ (in Equation 4.18) is determined as a function of frequency for various rubber shoreAs. The Prony delta behaviour for rubbers from these tests is shown in Figure 4.7.

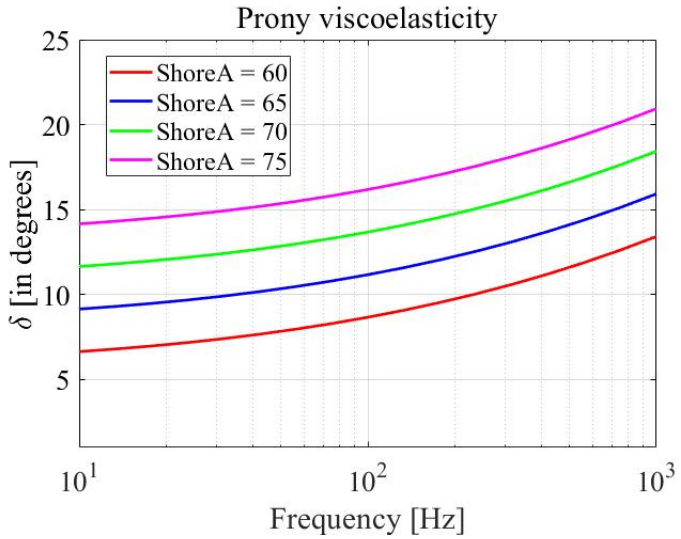

Figure 4.7: A general behaviour of the Prony delta or loss angle for a viscoelastic material as measured at IDIADA testing center. ShoreA values are normalised.

From this figure, the behaviour of Prony viscoelasticities can be theoretically expressed (by using curve fitting technique) by equation

$$\delta = (\log_{10}(f) - \log_{10}(X_{offset}))^p + Y_{offset}, \tag{4.19}$$

where p denotes the power which converts the log terms to a bi-quadratic log behaviour in order to describe the behaviour of curves.
In Equation 4.19, X_{offset} is a numerical value which represents the onset of viscoelastic effect (loss modulus) in the rubber and is independent of rubber hardness. However, the term Y_{offset} describes the shift of the Prony series curves (as shown in Figure 4.7) as a result of change in rubber hardness. Analytically, this term is expressed as a set of discontinuous equations as

$$Y_{offset} = \begin{cases} a \cdot shoreA + b, & hardness \leq 50 shoreA, \\ c \cdot shoreA - d, & hardness > 50 shoreA, \end{cases} \tag{4.20}$$

Cette thèse est accessible à l'adresse : https://theses.insa-lyon.fr/publication/2022ISAL0081/these.pdf
© [B. Anantharamaiah], [2022], INSA Lyon, tous droits réservés

where a, b, c and d are parameters that are obtained during the process of curve fitting of Y_{offset} (as obtained from experiments) vs rubber shoreA. Now that the Prony series has been theoretically defined in Equation 4.19, it is necessary to determine the Prony coefficients g_i in Equations 4.14 and 4.15. These are the terms that need to be introduced into Abaqus® model to define the viscoelastic material properties of rubbers.
To determine these coefficients, Equations 4.14 and 4.15 are used to fit the curve determined by the theoretical Equation 4.19. However, before fitting, Equations 4.14 and 4.15 need to be reformulated and simplified to suit the fitting process. The arctan of the ratio of Equation 4.15 to Equation 4.14 yields the loss angle, i.e.

$$\delta = arctan\left(\frac{\sum_{i=1}^{N} g_i \frac{(\tau_i \omega)}{1+(\tau_i \omega)^2}}{[1-\sum_{i=1}^{N} g_i] + \sum_{i=1}^{N} g_i \frac{(\tau_i \omega)^2}{1+(\tau_i \omega)^2}}\right), \tag{4.21}$$

where N is chosen to be 8 so that the Prony parameter value g_i is determined (through curve fitting which is discussed subsequently) with adequate interval spacing within the limits of 10 Hz to 1 kHz. Term τ_i is defined by choosing random frequency values, at least two per decade, as

$$\tau_i = \frac{1}{2\pi f_i}. \tag{4.22}$$

Thus, Equation 4.21 is fitted against Equation 4.19 using FMINCON code with sqp algorithm in MATLAB®. The constraints of the fit is the frequency value, that is between 10 Hz to 1 kHz and the function that is fitted is the Prony parameter g_i. The result of fit is shown in Figure 4.8. From this figure, it can be observed that the theoretical and estimated Prony viscoelasticity show a good match with each other. Since this work is about the study of tyre noise perception due to mechanical effects up to 1 kHz, the Prony viscoelasticity fitting is restricted up to this limit. In case there is a need to estimate the effect of rubber Prony viscoelasticity beyond 1 kHz, the current methodology is flexible to incorporate this. However, the maximum operating frequency range of the rubber should be known before performing the fitting.

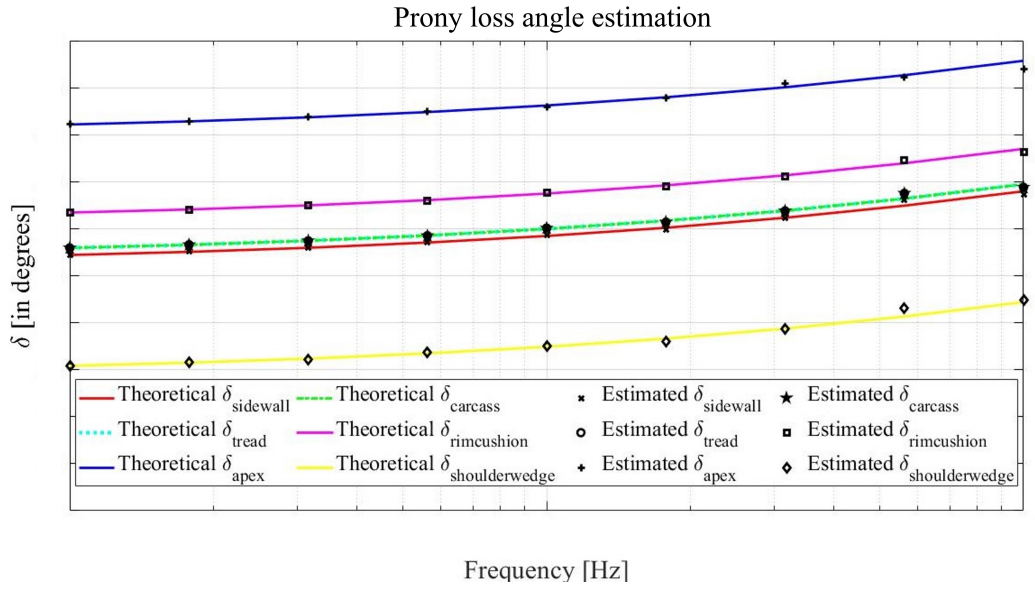

Figure 4.8: Estimation of g_i to fit the theoretical and estimated Prony loss angle curves. Theoretical values are calculated using Equation 4.19 and the estimated values, using Equation 4.21. Axis scaling is omitted due to confidentiality.

The main advantage of this technique, apart from the flexibility of extending the estimation frequency range as mentioned previously, are the non-necessity of repeated and tedious DMA

Cette thèse est accessible à l'adresse : https://theses.insa-lyon.fr/publication/2022ISAL0081/these.pdf
© [B. Anantharamaiah], [2022], INSA Lyon, tous droits réservés

testing to estimate the Prony term (g_i) as described in [93]. Apart from this, the current procedure of estimation of the Prony viscoelaticity terms improves the precision in tyre dynamic analyses, e.g. in [94] in which only one Prony term is defined per decade to analyse the rolling resistance of the tread material.

4.3 Results and discussion

Upon determining the values of Prony parameters, these values are used in the FE simulations of free-free and also loaded tyre to study their dynamic behaviour. It is important to state here that, previously (refer section 3.2.3), the modal damping values were used in the FE model to compare the model behaviour with the tests. In the current simulation, these values are discarded and, along with rubber viscoelasticity, the damping values are introduced to each component of the tyre. All steel components, namely the rim and the beads, are defined by a damping factor of 4% [95]. The rest, i.e. the nylon plies are defined using the Rayleigh damping. This is determined by calculating the mass and stiffness proportional damping coefficient values from the damping ratio (45%, normalised), as obtained from the IDIADA internal (confidential) standards for Nylon material. The procedure to determine these coefficients is referred from [96]. This frequency dependent damping behaviour is shown in Figure 4.9.

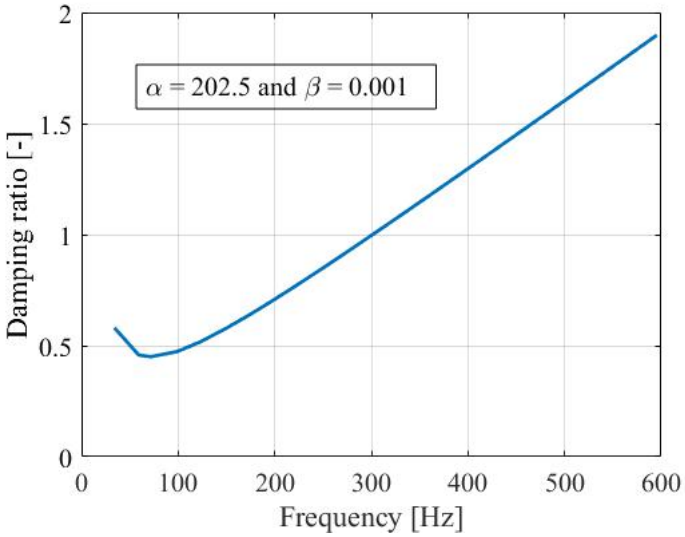

Figure 4.9: Values of the Rayleigh damping coefficients with a damping ratio of 45% for Nylon plies. The value of damping ratio is normalised for confidentiality.

4.3.1 Dynamic modelling of the free-free tyre with the Prony viscoelasticity data

Using the damping values as discussed in Section 4.3, the tyre free-free model is simulated and the PIs are compared with the tests. Figures 4.10a, 4.10b and 4.10c show this comparison for the three impact points, i.e. 16, 19 and 20 (as previously used in Section 3.2.1 Figure 3.7) considered for the tyre.
From Figure 4.10, it can be seen that the PI amplitude in test is lower than that of simulations, especially beyond 200 Hz. This discrepancy arises due to the fact that the Prony delta and rubber hardness relationships, as described in Equations 4.19 and 4.19, are established from measurement data of rubbers up to 300 Hz. In this work, the same relationships are used to extrapolate the Prony delta for the frequency limit to 1 kHz. This mathematical estimation comes at the cost of underestimation of damping values.

Cette thèse est accessible à l'adresse : https://theses.insa-lyon.fr/publication/2022ISAL0081/these.pdf
© [B. Anantharamaiah], [2022], INSA Lyon, tous droits réservés

Nevertheless it can be concluded that there is a good match in the dynamic behaviour of the free-free tyre between tests and simulations in terms of PI. The damping definitions that are proposed in the simulation model, i.e. the Prony viscoelasticity for rubbers and the Rayleigh coefficients for Nylon plies, are capable enough to predict the dynamic behaviour of the free-free tyre. A comparison of the PIs between the simulation models consisting of rubber viscoelastic definitions and modal damping factors (as discussed in Section 3.2.3) is provided in Appendix A Figure A.11. As a next step, it is necessary to model and study the loaded tyre dynamics using these damping definitions, since a loaded tyre represents more realistic working condition of a tyre.

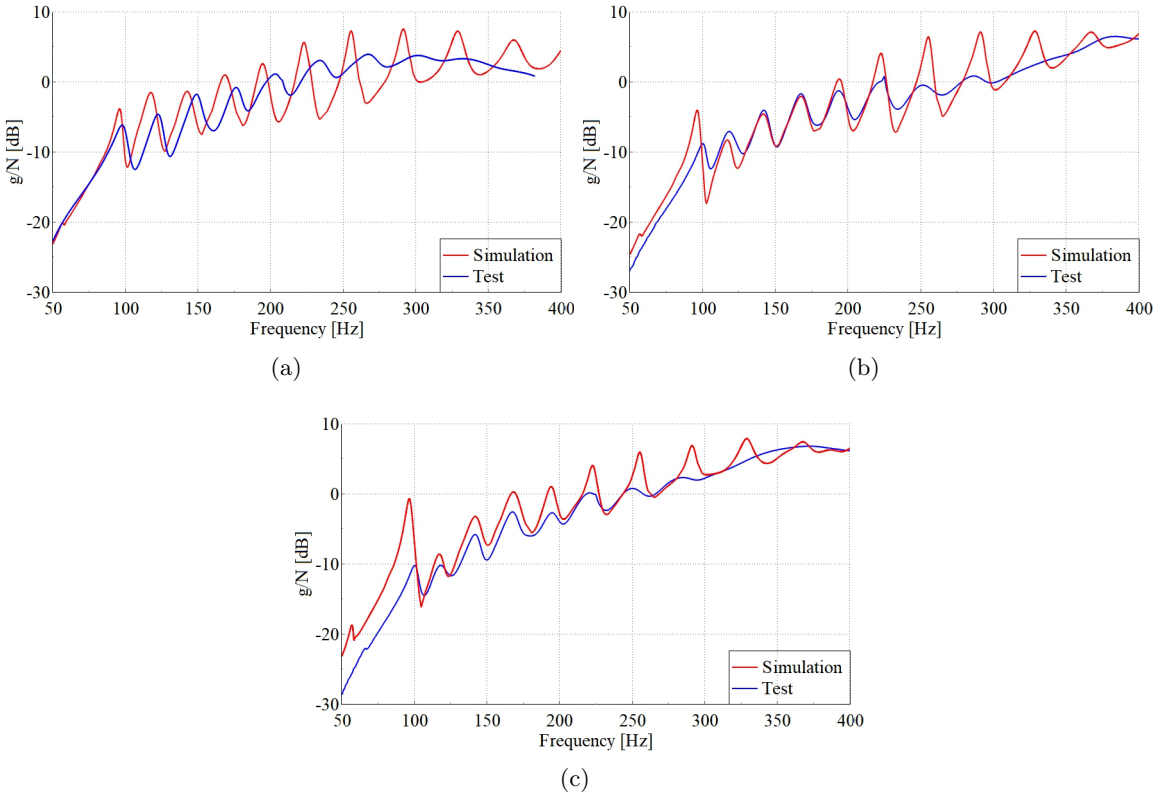

Figure 4.10: Comparison of point inertances between test and simulation with the Prony viscoelasticity definition - (a) for point 16, (b) for point 19 and (c) for point 20. Refer Figure 3.7 for the location of the points.

4.3.2 Dynamic modelling of the loaded tyre with the Prony viscoelasticity data

In the discussion until now, focus was laid on a free-free tyre since it is a very simple condition that can be used to characterise the tyre material properties. In subsequent steps, the characterised materials are used in a loaded tyre FE model to predict the tyre dynamic behavior. This study is important since this type of tyre model represents a condition in which a tyre operates in the real world. The modus operandi of this study is to load the tyre statically on a test-bench and excite a tread to determine the PI. This PI is then correlated with the tyre PI from the simulation model which is setup exactly according to the test-bench conditions.
The test setup of the loaded tyre is shown in Figures 4.11a, 4.11b, 4.11c and 4.11d. A solid block of large mass is used to apply a predetermined static force (F_1) as shown in Figure 4.11a. Now, a shaker is used to excite the tyre as opposed to hammer since the latter could not induce adequate energy to excite all the modes of the tyre. Moreover, the VTF showed low match for

Cette thèse est accessible à l'adresse : https://theses.insa-lyon.fr/publication/2022ISAL0081/these.pdf
© [B. Anantharamaiah], [2022], INSA Lyon, tous droits réservés

frequencies beyond 400 Hz (refer Figure 3.8) for hammer impacts.

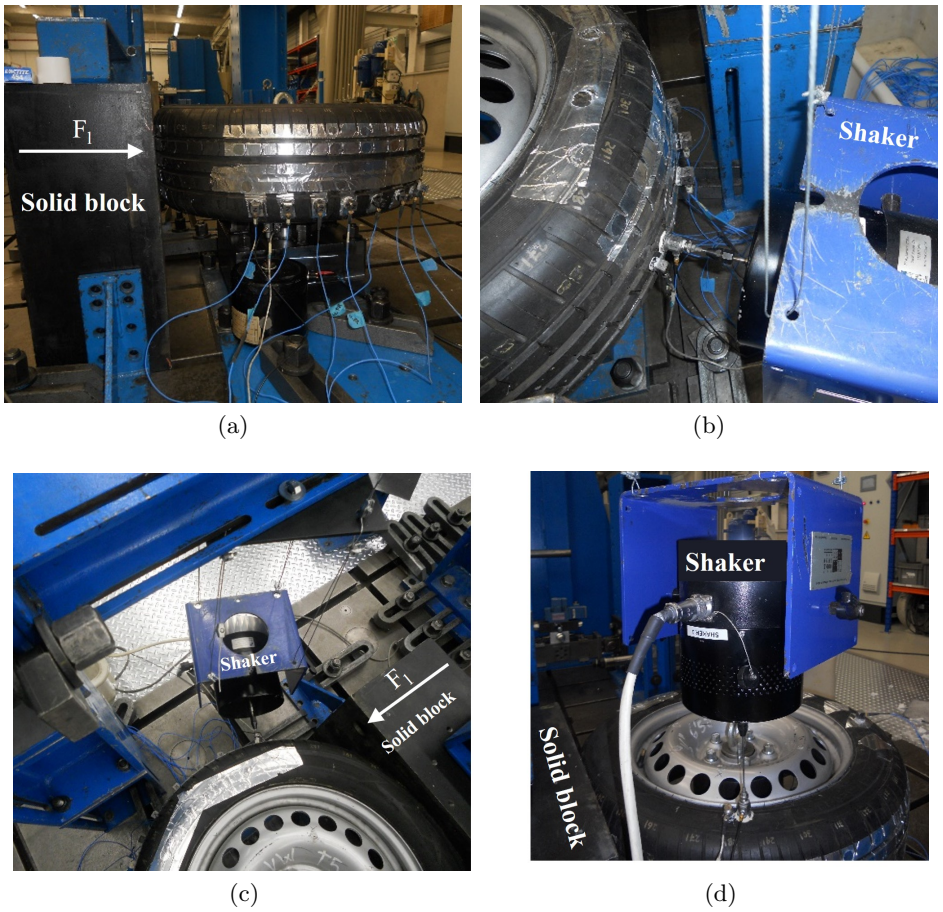

Figure 4.11: Loaded tyre setup for modal analysis. (a) Sideview showing solid block and direction of application of static load (F_1), (b) closeup view of the location of the application of shaker force on tread, (c) top view of the test setup for tread excitation and (d) sidewall excitation point. The solid block exerts a static load on the tyre.

The point of the application of shaker load on a tread block is shown in Figures 4.11b and 4.11c (top view). The location of sidewall excitation is shown in Figure 4.11d. A fixed level of burst random signal is used for shaker excitation. PIs are determined using monoaxial accelerometers in close proximity of the excitation.
In simulations, the loading and PI measurement points are maintained identical to the corresponding ones in tests (as in Figure 4.11b and 4.11c). This simulation model is shown in Figure 4.12. In the simulation, the solid block is modeled as an infinitely rigid surface. Figures 4.13a and 4.13b compare the results obtained from the test and the simulation for tread excitation and sidewall excitation, respectively. From these figures, we can observe that there is a good match in terms of PI and levels, especially for tread excitation (Figure 4.13a).
For sidewall excitations, as seen in Figure 4.13b, although the coherence and the prediction of PI behaviour is good, the level of modes beyond 250 Hz is lower in simulation than in tests. There are two reasons for this case:

- the mesh size in the sidewall region is coarser compared to tread. This leads to artificial localised stiffness which restricts the nodal displacements during numerical interpolation and
- the mass effect of the shaker coil induces an increase in the vibration measured on the sidewalls. This is because, for the sidewall measurement setup, the shaker coil is under

Cette thèse est accessible à l'adresse : https://theses.insa-lyon.fr/publication/2022ISAL0081/these.pdf
© [B. Anantharamaiah], [2022], INSA Lyon, tous droits réservés

the influence of shaker force and the gravitational force. However, the PI determined during the acquisition only considers the shaker force due to which the level of inertance is comparatively higher.

Nevertheless, it can be observed that there is a very good coherence in sidewall and tread excitation tests. This means that the results obtained from tests are reliable up 1 kHz. It is brought to the notice of the reader that although air elements are modeled inside the tyre torus, the influence of temperature changes on the tyre modal or noise behaviour is neglected.

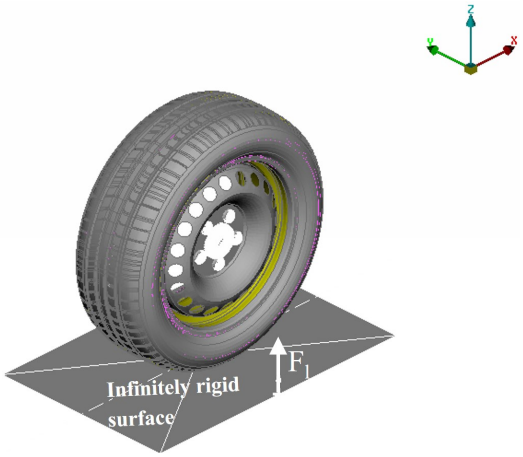

Figure 4.12: FE simulation setup of the loaded tyre

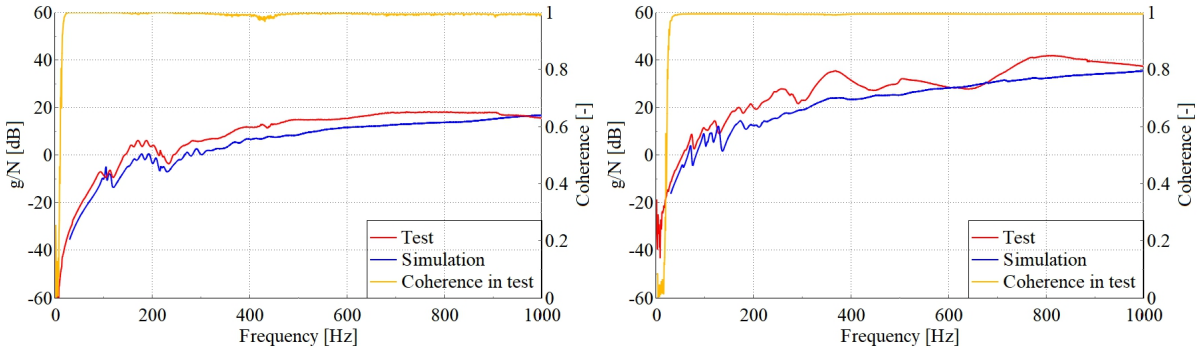

Figure 4.13: Point inertance measurement results of the loaded tyre (a) comparison of test and simulation results for a tread point excitation (refer Figures 4.11b and 4.11c for tread impact location information) and (b) comparison of test and simulation results for a sidewall point excitation. Refer Figure 4.11d for sidewall impact location on a loaded tyre.

4.3.3 Noise modelling of the loaded tyre

In this work so far, it was proved that the modelling of tyre dynamics is possible for higher frequencies (e.g. 1 kHz) through the implementation of material based damping. Now, it is necessary to model the tyre noise, especially for a loaded tyre for the corresponding frequency limit. To achieve this, firstly, the loaded tyre NTFs are determined by impact testing in a hemi-anechoic chamber. The impact is made on the same tread location as described in Section 4.3.2, but with a hammer instead of a shaker. This is because, shaker excitation leads to additional noise during its operation. Space constraints in the measurement setup, the size and mass of

Cette thèse est accessible à l'adresse : https://theses.insa-lyon.fr/publication/2022ISAL0081/these.pdf
© [B. Anantharamaiah], [2022], INSA Lyon, tous droits réservés

the shaker posed as a hurdle to setup any mechanism to isolate its operational noise.
The test setup consists of a piston mechanism that applies a loading force on the solid block, and thus on the tyre that is mounted on a base using a fixture as shown in Figure 4.14a. Various microphones are placed to measure the NTFs due to the impact on the tyre treads. These are shown in Figure 4.14b.
To calculate the NTFs from simulations, again, the sequentially coupled submodelling technique is used as described in Figure 3.13. However, these now include necessary modifications to consider possible reflections due to the base and the solid block. The structural model/tyre simulation model in which the outer most nodal displacements are saved, remains the same. These displacements are used as boundary conditions for the submodel and acoustic simulations. However, in the submodel, the base and the solid block are included as reflecting surfaces for acoustic simulations, the cross section of which is shown in Figure 4.14c. The front view of this model without acoustic mesh is shown in Figure 4.14d. The comparison between test and simulation NTFs are made for microphone M1 (shown in Figure 4.14b). The coordinates of this microphone is shown in Figure 4.15.

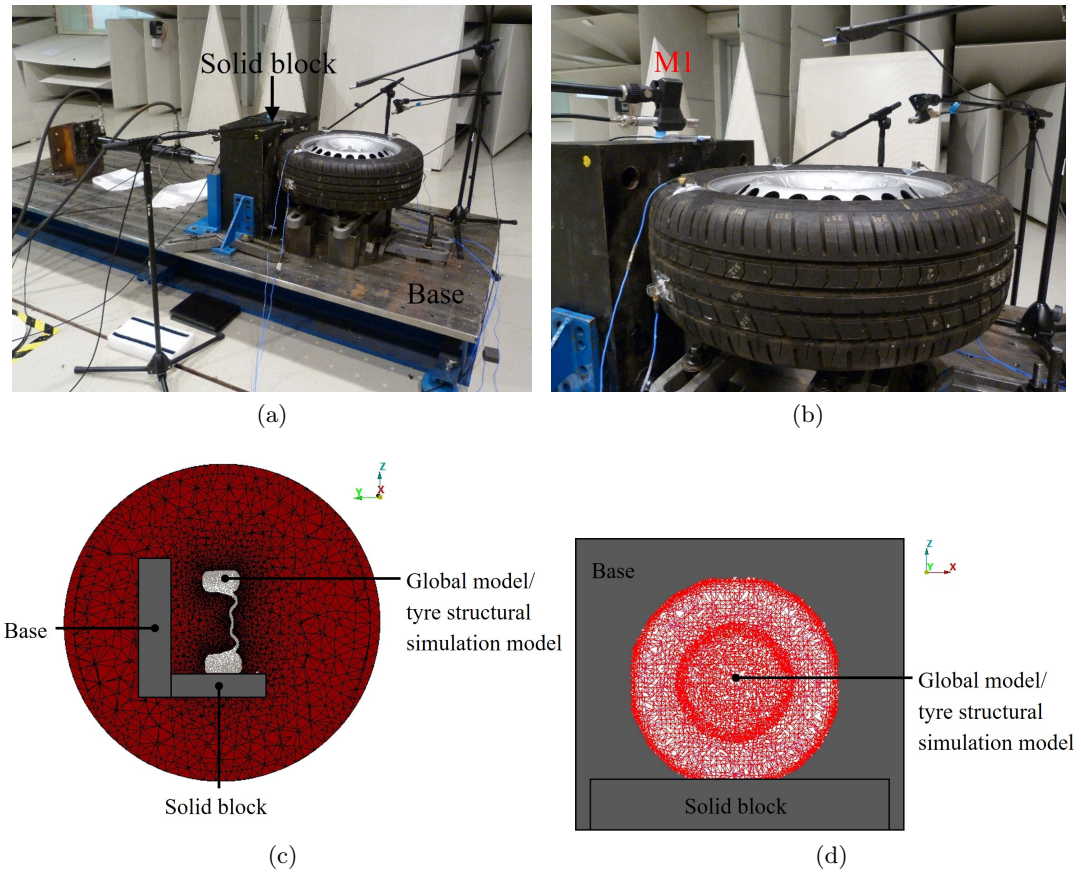

Figure 4.14: Noise analysis of a loaded tyre (a) test setup in hemi-anechoic chamber, (b) Microphone setup in test, (c) side cross-section of the acoustic submodel and (d) front view of structural mesh in acoustic submodel simulation.

Figure 4.16 offers a comparison of output NTFs between the test and the simulation for the loaded tyre model. The NTFs in simulation are measured using sensor nodes that are positioned according to the coordinates defined in the tests (refer Figure 4.15). In Figure 4.16, it can be observed that the inclusion of reflection in 3D plane in the simulation is important, especially for the frequency ranges beyond 450 Hz. For non-reflective condition, the model as described in Figure 3.13 is used. It can also be seen that in spite of the inclusion of reflection modelling,

Cette thèse est accessible à l'adresse : https://theses.insa-lyon.fr/publication/2022ISAL0081/these.pdf
© [B. Anantharamaiah], [2022], INSA Lyon, tous droits réservés

there exists a drop of 10 dB in NTF level post 450 Hz. It can be attributed to two reasons:

- Coarser acoustic mesh which leads to underestimation of levels. However, the finer the model the higher is the computational cost and time;
- Necessity of precise definition/modelling of acoustic reflection which is very complex, ideally, since these reflections are dependent on various components of which only the base and the solid block are considered in simulation.

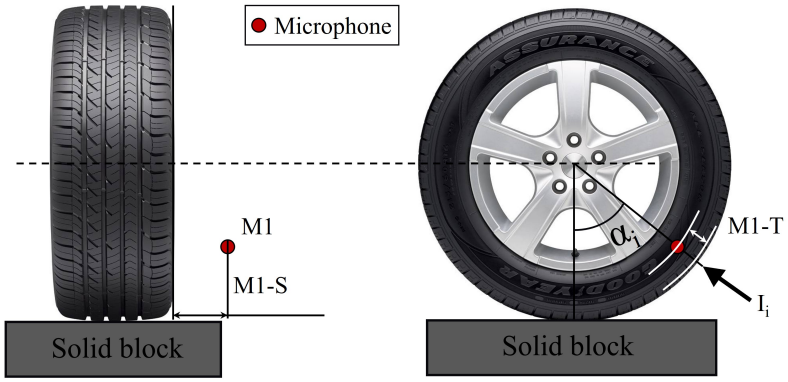

Figure 4.15: Microphone M1 position for the noise measurement in the loaded tyre in test. M1-S = 0.1 m, M1-T = 0.06 m and $\alpha_i = 60°$. I_i is the hammer impact point on the tyre tread.

Nevertheless, it can be observed that beyond 450 Hz, although there is a constant drop of 10 dB in the amplitude levels, the output NTF from simulation matches the progression of that in the test. Hence, it can be concluded that there is a fair match of NTFs and the developed FE model captures the main trends and levels of the NTF of the loaded tyre. Additionally, from the same figure, it can be observed that the NTF from test has a lot of variations. Not neglecting the fact that the lower modes of tyre has the highest radiation efficiencies [97], these variations in NTFs are possible due to multiple reflections at the vicinity of the microphone. Refer Figures 4.14a and 4.14b for the measurement setup.

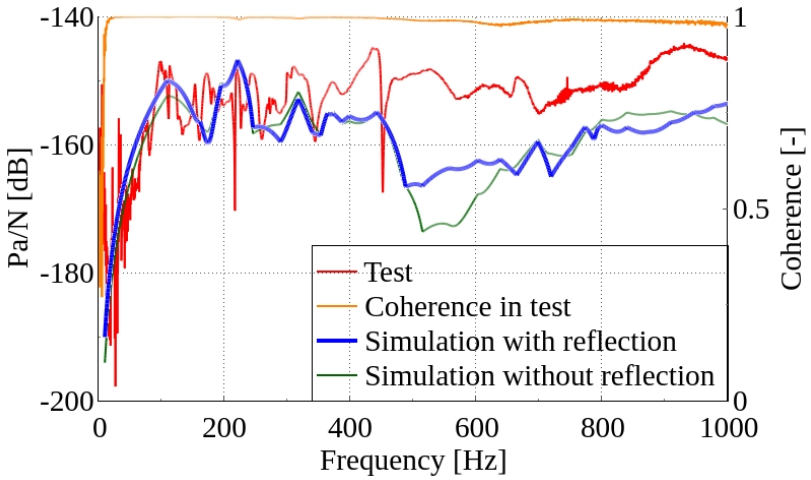

Figure 4.16: Comparison of test and simulation output NTFs for loaded tyre model with and without reflection due to setup components. Acoustic reflection model is shown in Figure 4.14c. Non-reflective acoustic model is described in Figure 3.13.

Although there has been a constant drop in the level of NTF from simulations, it is important to verify the sensitivity of the current model. This is to check the reliability of the model

Cette thèse est accessible à l'adresse : https://theses.insa-lyon.fr/publication/2022ISAL0081/these.pdf
© [B. Anantharamaiah], [2022], INSA Lyon, tous droits réservés

to predict variations in different conditions, especially the sensitivity of NTFs for various tyre inflation pressures. For this verification, the tyre with three different inflation pressures, i.e. 2.1 bar, 2.4 bar and 2.7 bar is considered. The NTFs from the test and the simulation are compared with each other. Figure 4.17 provides information on FE acoustic model sensitivity for various tyre inflation pressures.

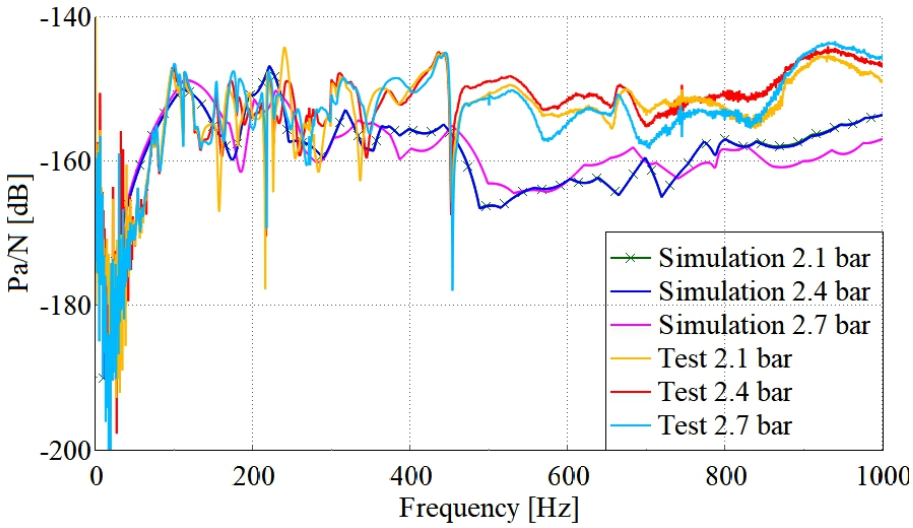

Figure 4.17: Sensitivity check of FE acoustic model for various tyre inflation pressures.

It can be observed from this figure that there is trivial difference between NTFs for various inflation pressures in test. Especially, the NTFs for 2.1 bar and 2.4 bar indicate peaks that overlap with each other while that of 2.7 bar has slight variations. This is also exhibited by the FE acoustic simulation model. In FE simulation results it can be seen that NTFs of tyre inflated at 2.1 bar and 2.4 bar overlap with each other whereas the one with 2.7 bar displays minor variations. Thus, it can be concluded that although the model shows that the difference in the output NTFs for the three tyre pressures are of the same order of magnitude as those found in the tests, it does not allow the possibility to assess the robustness of the correlation for this small range of tyre pressure variation.

4.4 Conclusions

From this chapter, it is clear that the definition of material based or viscoelastic damping is necessary in order to model tyre dynamic behaviour for higher frequencies. These definitions can be of several types, however in this work, it was defined as Prony series, specifically in terms of Prony pair/parameter. These parameters represent the viscoelastic damping for a given set of frequency ranges, which in the current work was 10 Hz to 1 kHz. For every rubber of the tyre, these parameter values are estimated from fitting the experimental data with that of a theoretical equation. While the experimental data is expressed as a mathematical relation between loss angle and rubber shore hardness, the theoretical expression establishes a relation between the loss angle and Prony parameters. Once the Prony parameters were determined using this technique, they were incorporated into FE simulation to model tyre modal and noise behaviour.

For this study, the free-free tyre and the loaded tyre were considered. The impact and PI measurement locations in the free-free tyre remained the same as in previous chapter. In case of loaded tyre, a solid block of approximately 10 ton was used to apply a static load of 5 kN on the tyre. In the modal acquisition study the tyre was impacted in its loaded condition using a shaker at a location approximately 60° from the contact patch. In case of noise measurement of

Cette thèse est accessible à l'adresse : https://theses.insa-lyon.fr/publication/2022ISAL0081/these.pdf
© [B. Anantharamaiah], [2022], INSA Lyon, tous droits réservés

a loaded tyre, the same location was impacted using a hammer in order to eliminate the noise that is generated due to the excitation of the shaker coil.
From the results of tyre dynamic simulations, it was observed that there was a very good match in tyre PIs with test up to 1 kHz for the loaded tyre and 500 Hz for the free-free tyre (the limit of comparison for the free-free tyre was only up to 500 Hz due to drop in coherence beyond this frequency as described in previous chapter). Continuing the discussion about the loaded tyre, although the PI due to sidewall excitation showed minor variations, it is a result of added mass effects from the shaker. Nevertheless, the level of PIs stood comparable in test and simulation.
From the results of output NTFs calculations, it was observed that there is a good match between the NTFs of test and simulation up to 450 Hz beyond which there is a constant drop of 10 dB up to 1 kHz in the simulations. However, this should not hinder the further simulation process since the dB drop will be evident in all cases. This was also observed in the simulation models of tyres with various inflation pressures. The FE model was sensitive to variations in inflation pressure, even though these variations were trivial. It should be noted that such small differences in responses caused by small tyre pressure variations do not facilitate to draw conclusions about the robustness of the correlation. Moreover, the actual location of the impact during the tyre rolling is closer to the tread contact patch, thus the dB loss may not be highly significant.
With the current model, it can be seen that the essential material properties of tyre rubbers have been well characterised. By employing these, the next objective is to model the rolling noise of the tyre and subjecting it to listening tests. To achieve this, the principle of convolution and concatenation is used to synthesise the tyre rolling noise instead of actually rolling the tyre in simulations. Tyre treads close to contact patch are impacted and the corresponding NTFs are determined. These are further converted into time domain IR signals using IFFT technique which are then convolved with the forces acting on corresponding treads. Finally, the convolved impulse responses thaat are generated are concatenated to obtain the rolling noise. In this process, only simulation models will be considered since it is technically impossible to impact the treads at the contact patch in tests. However, the characteristics of rolling noise that are generated in simulation for various conditions are correlated against those obtained from tyre rolling noise measurements in hemi-anechoic chamber.

Cette thèse est accessible à l'adresse : https://theses.insa-lyon.fr/publication/2022ISAL0081/these.pdf
© [B. Anantharamaiah], [2022], INSA Lyon, tous droits réservés

Cette thèse est accessible à l'adresse : https://theses.insa-lyon.fr/publication/2022ISAL0081/these.pdf
© [B. Anantharamaiah], [2022], INSA Lyon, tous droits réservés

5

Simulation of tyre rolling noise and psychoacoustics

In the previous chapter, an acoustic FE model was developed to model the generation of tyre noise and its propagation. It was accomplished only for an impact on a predefined location on the tyre but for various inflation pressures. Although that provided information about the credibility, reliability and limitation of the developed acoustic model, it did not consider the generation of realistic impact noise (IN) which occurs in the proximity of contact patch. Apart from that, it also did not consider the realistic forces acting on the tyre treads while rolling, which mainly influence the noise quality and attributes.
In the current chapter, the objective to model complete tyre rolling noise and its perception for various tyre inflation pressures and vehicle speeds considering the realistic conditions, is discussed. To achieve this, NTFs due to impacts in the contact patches are determined and converted to impulse responses (IRs) using IFFT technique. Forces acting on each tread in the contact patch of the rolling tyre are determined and are convolved with the corresponding tread IR. Next, the convolved IRs are concatenated to obtain tyre rolling noise. The average spectral power of the octave bands of the simulated and the measured rolling noise serve as a basis for comparing the similarities or differences between them. Finally, the simulated and the measured noise samples are subjected to listening tests, in which their unpleasantness are graded based on responses from 29 listeners.
It should be noted that although the detectability of tyre noise is the topic of concern with respect to the current work, due to time constraints and tedious test setup process the objective was streamlined to analyse annoyance only. The current work can be further implemented in detection studies in future.

Design of tyre tread pattern

A tyre tread pattern comprises of a set of treads of various pitch lengths (L_p). If every tread block featured the exact same size and shape, each one would generate the exact same sound tone and intensity as they rolled through contact with the road. This would result in tyres contributing to an unpleasant monotonous tone. In order to avoid that from happening, tyre designers use computers to sequence multi-pitch tread designs that subtly vary tread block size and shape to randomize the forces acting due to the road contact and the resulting noise. A small offset is provided in the circumferential block placement of neighboring block to reduce noise by aligning lateral grooves with adjacent tread blocks. This is called tread pattern randomisation which will be discussed in the subsequent section.
It is important to understand the tread geometry used in this work before proceeding further. Figures 5.1a, 5.1b and 5.1c portray the tread blocks with various pitch lengths used in this work. These represent the tread block design for a non-inflated and non-loaded tyre. It can

Cette thèse est accessible à l'adresse : https://theses.insa-lyon.fr/publication/2022ISAL0081/these.pdf
© [B. Anantharamaiah], [2022], INSA Lyon, tous droits réservés

be observed from these figures that there is a small circumferential offset between the treads in each tread block. L_p is defined as the length of one tread of a tyre as shown in Figure 5.1d. Alternatively, it can also be defined as the length from a point on one tread block to the same point on the next immediate tread block.

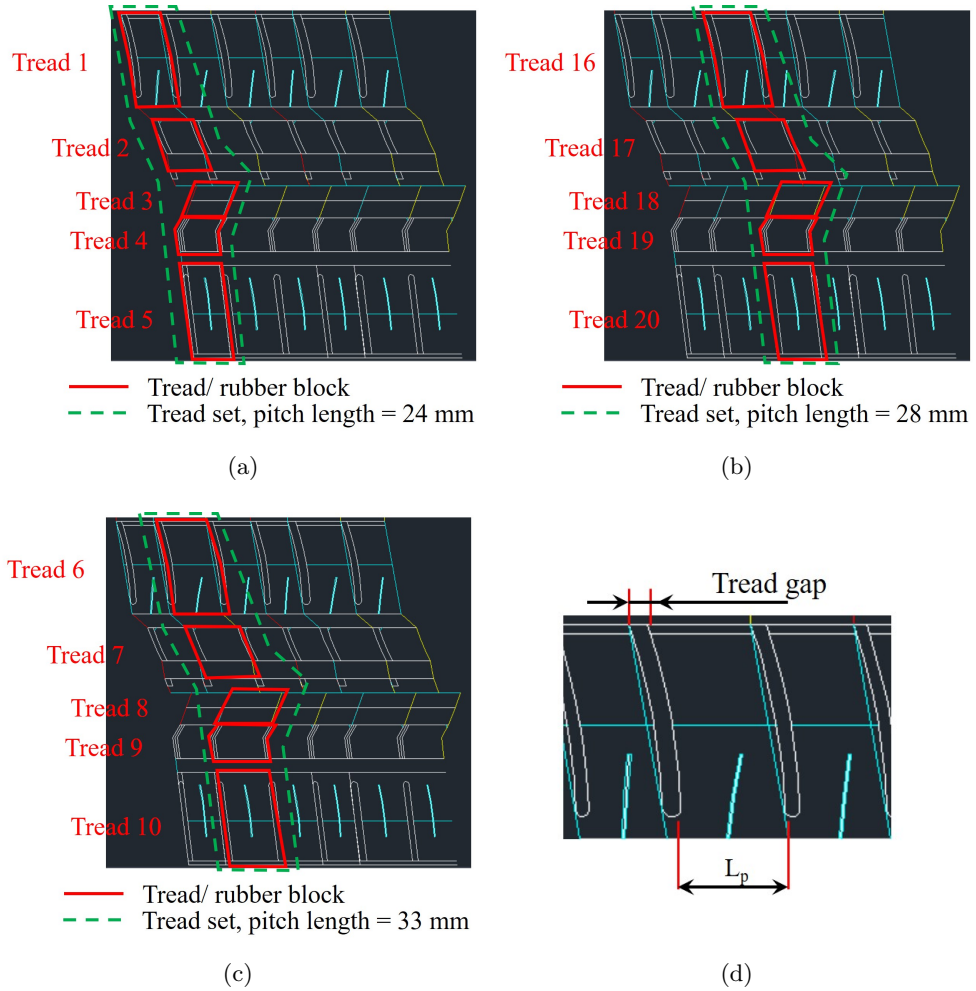

Figure 5.1: Tread/ rubber blocks of various pitch lengths used in this work. Tread blocks of (a) small pitch, (b) medium pitch and (c) large pitch for a non-inflated and non-loaded tyre. (d) The definition of pitch length (L_p).

5.1 Modelling of tyre impact rolling noise

Considering the fact that tyre-road interaction noise due to vibrational mechanisms emerges mainly due to the impact at contact patch, it is now necessary to model this noise using FE simulations. Figure 5.2a depicts the contemporary/instantaneous impact points at the contact patch when the tyre is rolling. For the determination of the rolling noise, only the impacts at the leading edge are considered in this work. The location of the impact points at the contact patch is visualised in Figure 5.2b. From this figure, it should be observed that the location of the microphone that is used in the previous chapter, remains unchanged.
To simulate the tyre rolling noise, the following technique is adopted:

- Simulate the tyre tread impact NTF;
- Determine the corresponding IR by applying the IFFT on the simulated NTF;

Cette thèse est accessible à l'adresse : https://theses.insa-lyon.fr/publication/2022ISAL0081/these.pdf
© [B. Anantharamaiah], [2022], INSA Lyon, tous droits réservés

- Convolution of individual tread IR with corresponding rolling forces acting on the tread block. The rolling forces correspond to time history of tread force acting during the tread entry into and exit from the contact patch. A brief introduction to convolution technique is provided in Appendix B Section B.1. And
- Concatenate the audio files resulting from convolution according to the tread randomisation data provided by tyre manufacturer to generate tyre rolling noise.

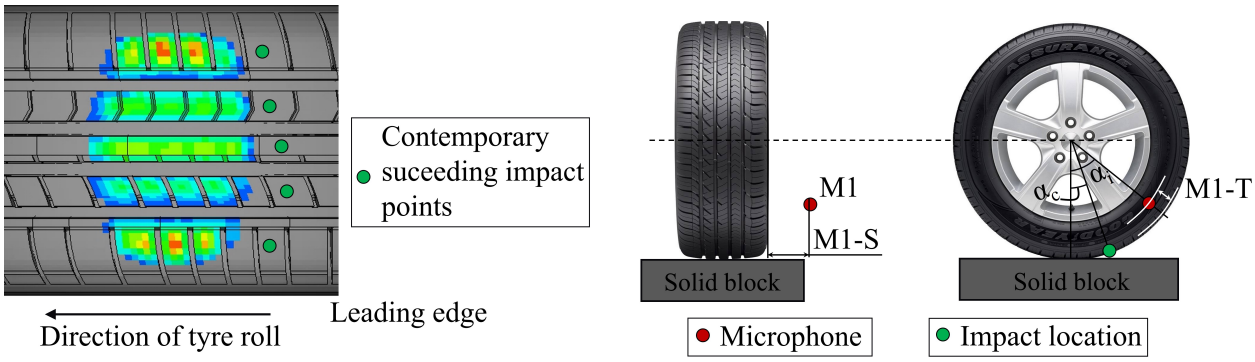

Figure 5.2: Modelling of the impact location of the rolling tyre. (a) Impact points at contact patch during tyre rolling and (b) visualisation of the location the impact points of the rolling tyre. M1-S = 0.1 m, M1-T = 0.06 m, $\alpha_i = 60°$ and $\alpha_c \sim 20°$.

Figure 5.3 describes the procedure in a concise manner.

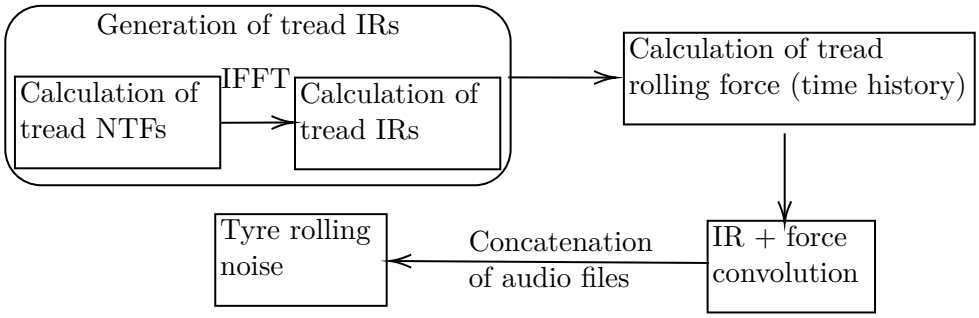

Figure 5.3: Procedure for the modelling of tyre rolling noise.

5.1.1 Determination of tyre tread impulse responses

Although the considered tyre has three different tread pitch lengths, the IRs are determined using IFFT technique from the corresponding NTF of impact on the medium tread pitch block $16 - 20$ (refer Figure 5.1b) from simulation. In real time tyre rolling condition, the rolling noise of a tyre is a function of rolling force acting on each tread block. Hence, the IRs from other treads could also be considered simultaneously, provided there are no (computational) restrictions in time and resources for the calculations of corresponding NTFs and IRs. The other reason to consider these specific tread blocks is that they were used for the correlations of test-simulation results in Chapter 3.
The simulated tyre NTFs for an inflation pressure of 2.4 bar are shown in Figure 5.4a. From this figure, it can be observed that the NTF for each rubber block is different from the other. Tread 16 has lower amplitude compared to, e.g., tread 20 at lower frequencies, however, its level is higher in high frequencies. The influence of tread position can also be seen in the phase diagram

Cette thèse est accessible à l'adresse : https://theses.insa-lyon.fr/publication/2022ISAL0081/these.pdf
© [B. Anantharamaiah], [2022], INSA Lyon, tous droits réservés

in the same figure. Phase difference also varies for a shift in the impact on the treads along 16 to 20. Thus, it can be concluded that each rubber block along the tyre tread set has specific excitation behaviour. By using IFFT technique, the IRs of these tread NTFs are determined and are shown in Figure 5.4b.

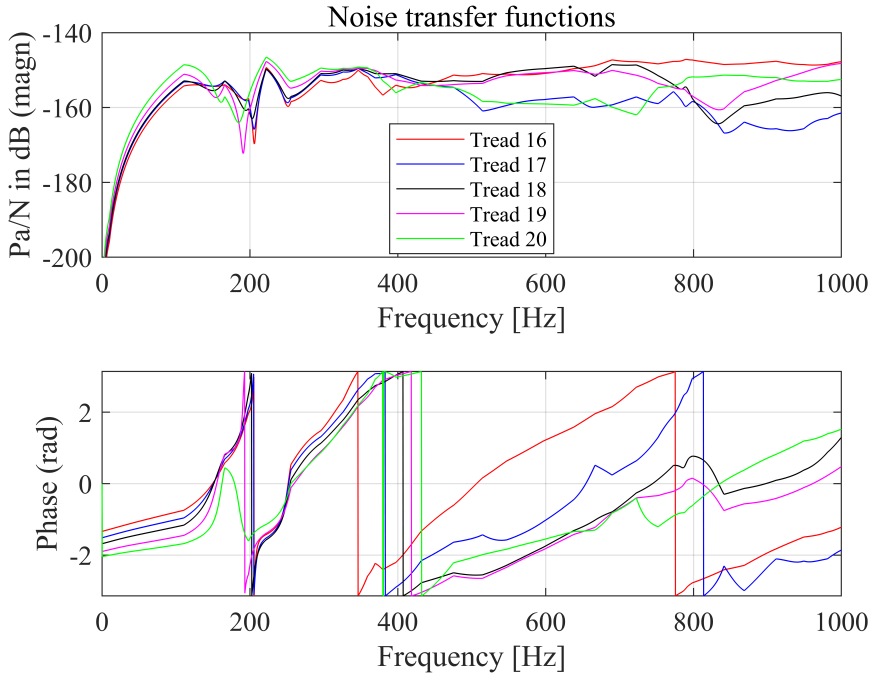

(a)

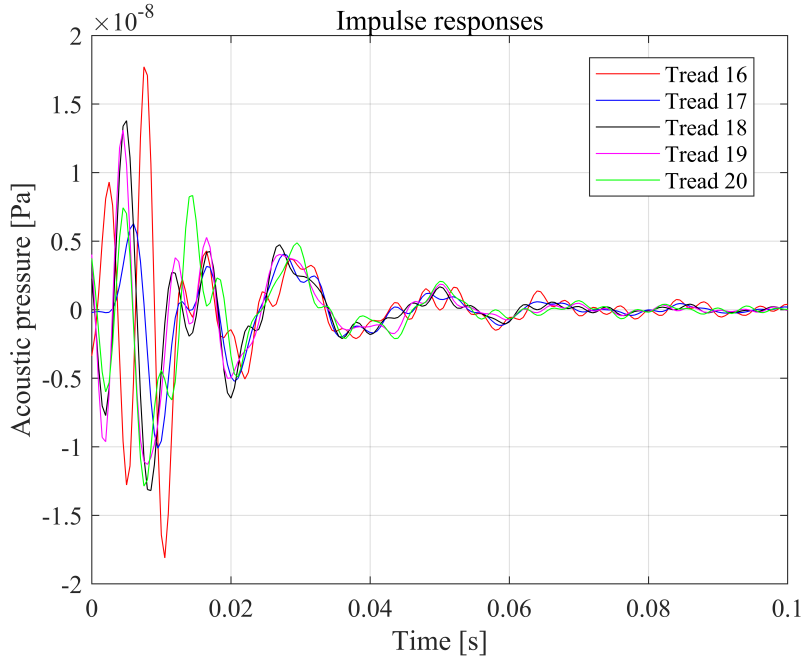

(b)

Figure 5.4: Tyre tread noise behaviour study for a tyre inflated at 2.4 bar. (a) The NTF plot of tread block impacts considered and (b) IRs generated from IFFT of NTFs of the treads considered. Considered for these studies are medium pitch tread blocks as shown in Figure 5.1b. Sampling frequency - 2 kHz.

Cette thèse est accessible à l'adresse : https://theses.insa-lyon.fr/publication/2022ISAL0081/these.pdf
© [B. Anantharamaiah], [2022], INSA Lyon, tous droits réservés

From the same figure, it can be observed that different rubber blocks have different levels and temporal peaks in their corresponding IRs. Hence, each tread block contributes uniquely to the overall noise generated from the tyre while rolling. In a similar way, IRs for tread impacts for various tyre inflation pressures are determined (refer Appendix B.2 Figures B.1 and B.2). These are necessary in order to study the influence of tyre inflation pressure on its rolling noise perception, which will be discussed in the upcoming sections.

5.1.2 Determination of tyre contact forces and convolution with IRs

The IRs that are generated from the NTFs due to tread impacts (at the leading edge of the contact patch) do not sufficiently describe the tyre noise generated in reality. To model the noise from a single tread block during its rolling precisely, its IR must be convolved with its corresponding contact patch force during the tyre roll. Rolling forces acting on each tread are determined from FE simulations, the model setup of which is shown in Figure 5.5. The rubbers of the tyre FE model used in this simulation bear the hardness values that were determined from optimisation process using DoE and the viscoelastic properties that were estimated from curve fitting of loss angle; these are described in details in Chapters 3 and 4, respectively.

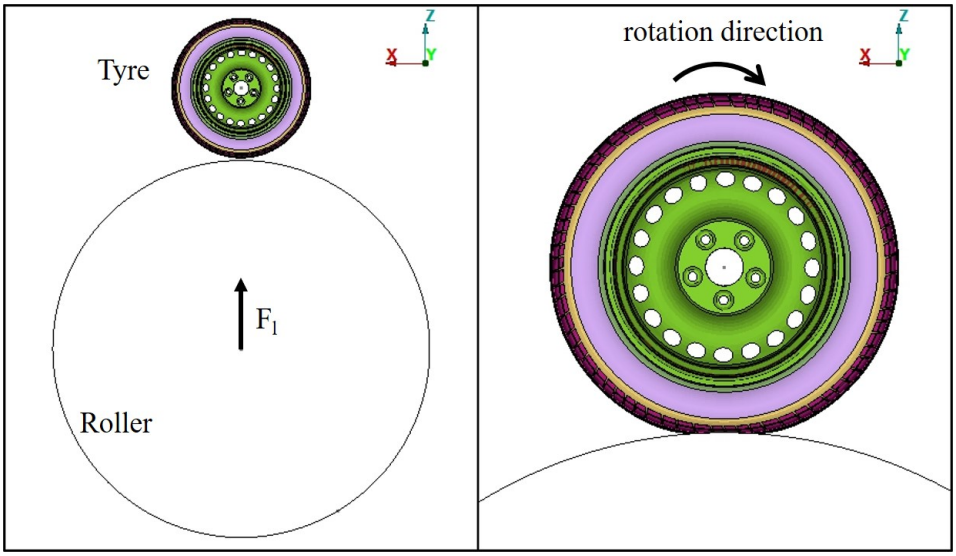

Figure 5.5: FE setup to determine the forces on the tyre tread during rolling. (Left) Direction of roller loading and the magnitude of load, F_1, and (right) close-up of the contact between the tyre and the roller. The contact patch is shown in Figure 5.2a.

In the FE model setup, all degrees of freedom (DoF) except Dz (linear DoF in the z direction) of the roller are fixed. The tyre is rotated for two (roll) cycles in order to ensure that a stable rolling condition is achieved and all the treads experience the contact patch forces. In this way, tyres with three different inflation pressures are loaded and the contact forces acting on treads are determined. A comparison of forces acting on the (small pitch) treads 16-20 of the tyre with different inflation pressures and F_1 of 5000 N (refer Figure 5.5), that is rotating at a linear velocity of 30 kph is shown in Figures 5.6a to 5.6e. Figure 5.6f shows the variation in forces acting on the treads of the tyre which is inflated at 2.4 bar and rotating with a linear velocity of 30 kph. It can be observed from this figure that forces on the treads are not uniform at the contact patch. The treads at the outermost ends are restricted by sidewall region due to which reaction forces accumulate in this region. This is because, the tyre cross-section behaves like a *fixed ended* or a rotating *hinged* beam in which the outer treads are fixed by the sidewall rubbers [98]. This allows the treads to be in constant traction with the road surface. Figure 5.7 depicts this condition. Hence, reaction forces at these locations due to tyre-road contact are

Cette thèse est accessible à l'adresse : https://theses.insa-lyon.fr/publication/2022ISAL0081/these.pdf
© [B. Anantharamaiah], [2022], INSA Lyon, tous droits réservés

higher compared to other treads in the contact patch.
From Figures 5.6a to 5.6e, it can be observed that the magnitude of contact forces does not significantly *vary* for the outermost rubber blocks, i.e. tread 16 and tread 20 but do so for the inner three rubber blocks. This is normal since the increase in inflation pressure increases the radial dimensions of the tyre. Since tread 16 and tread 20 are held along by the sidewall region of the tyre, the system behaves like a bulged fixed ended beam of high tension at its ends. The representation is shown in Figure 5.7. The higher the inflation pressure, the higher is the bulge radius and the lesser is the roller contact with the outermost rubber blocks of the tyre. Due to this behaviour of the tyre, the magnitude of forces acting over treads 16 and 20 remains significantly constant as it can be seen in Figures 5.6a and 5.6e.

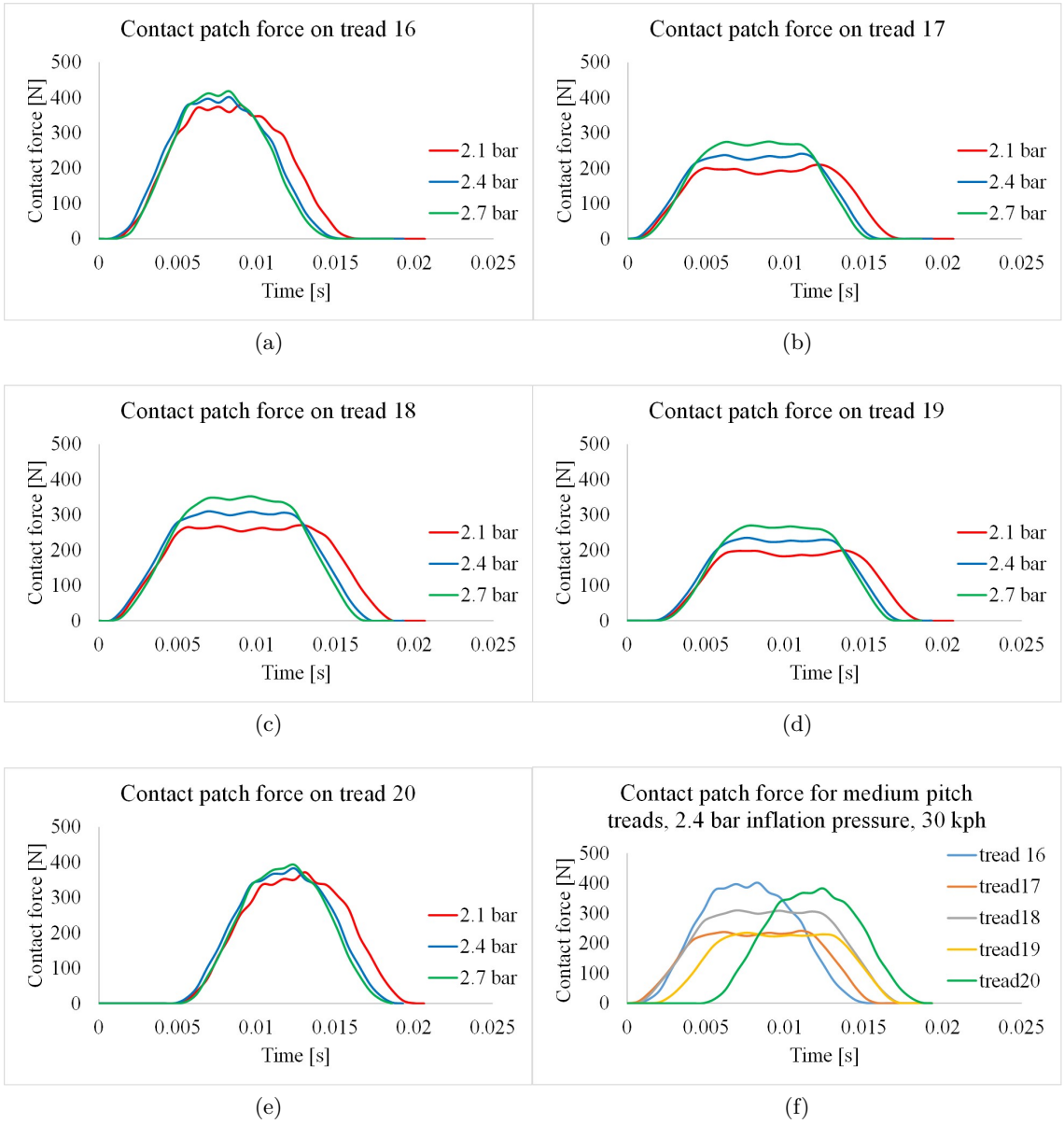

Figure 5.6: The influence of tyre inflation pressure on contact patch force for (a) tread 16, (b) tread 17, (c) tread 18, (d) tread 19 and (e) tread 20. (f) depicts the variation in contact patch forces on the treads of a tyre rolling at 30 kph and inflated to 2.4 bar pressure. Considered for these studies are medium pitch tread set as shown in Figure 5.1b.

Figure 5.8 describes the decreasing contact area of the outermost rubber blocks for increasing

Cette thèse est accessible à l'adresse : https://theses.insa-lyon.fr/publication/2022ISAL0081/these.pdf
© [B. Anantharamaiah], [2022], INSA Lyon, tous droits réservés

inflation pressure. However, for the rubber blocks 17, 18 and 19, the contact area remains constant, but these treads experience higher forces due to additional virtual forces arising from increasing inflation pressures. Additionally, due to increased radius, the duration of contact reduces. This phenomenon may also be witnessed, graphically, in Figures 5.6b to 5.6d.

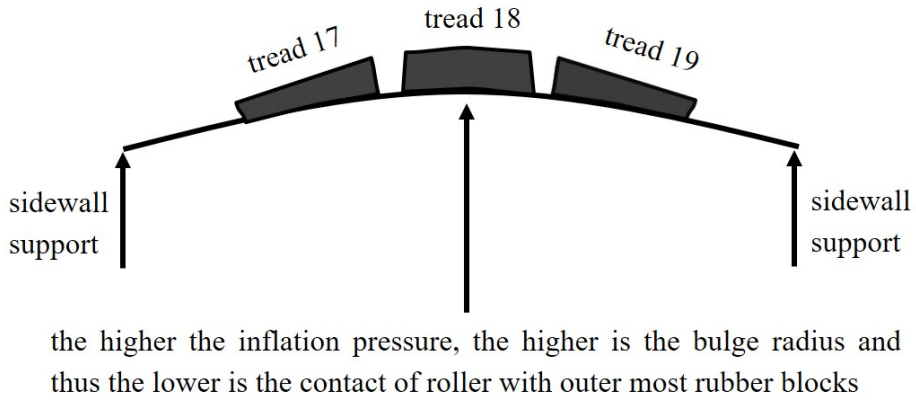

Figure 5.7: A tyre represented as a cantilever system sensitive to the internal pressure.

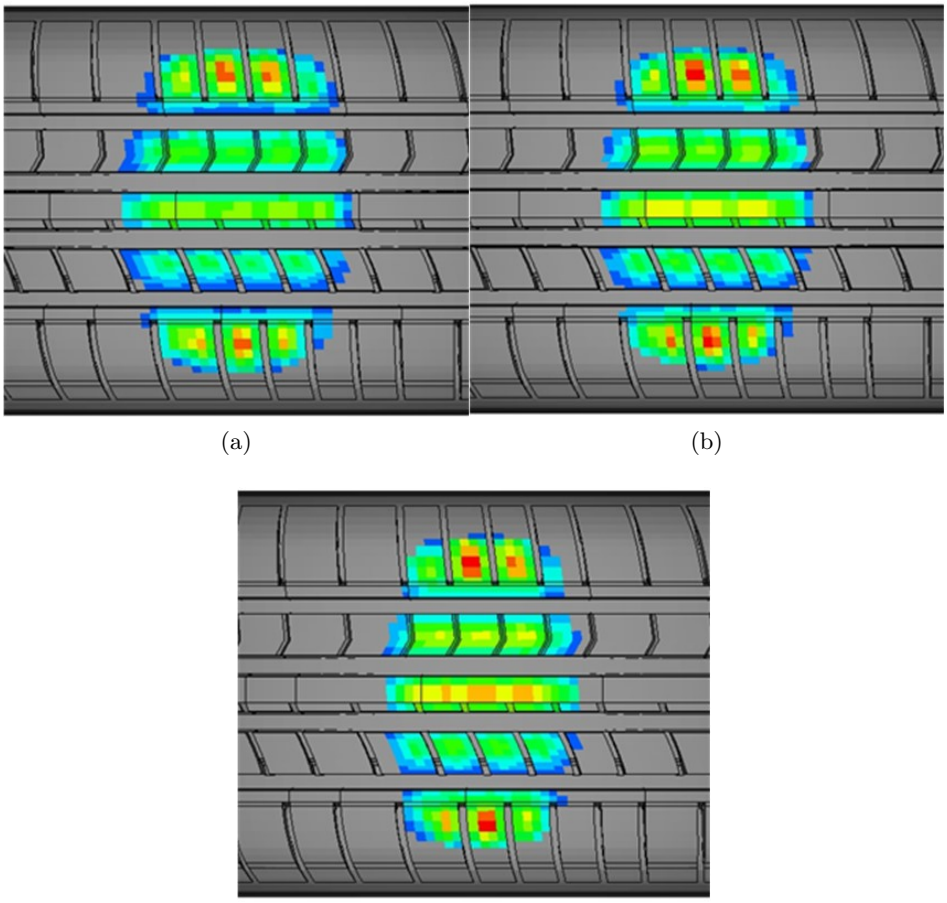

Figure 5.8: Tyre footprint illustrating the contact patch force distribution at a sample instant of time for the rolling tyre at 30 kph that is inflated at (a) 2.1 bar (b) 2.4 bar and (c) 2.7 bar for a loading force (F_l) of 5000 N.

Cette thèse est accessible à l'adresse : https://theses.insa-lyon.fr/publication/2022ISAL0081/these.pdf
© [B. Anantharamaiah], [2022], INSA Lyon, tous droits réservés

Contact forces for car speeds 40 km/hr and 50 km/hr are also determined. Finally, these forces are convolved with the IRs obtained from simulation that were as discussed in section 5.1.1. The convolution is performed using MATLAB®. The convolution force, IR and the corresponding convolved response for the medium pitch tread set of the tyre inflated at 2.4 bar moving with a linear velocity of 30 kph is shown in Figure 5.9. The same for the small and large pitch tread sets is shown in section Appendix B.2 Figure B.3.

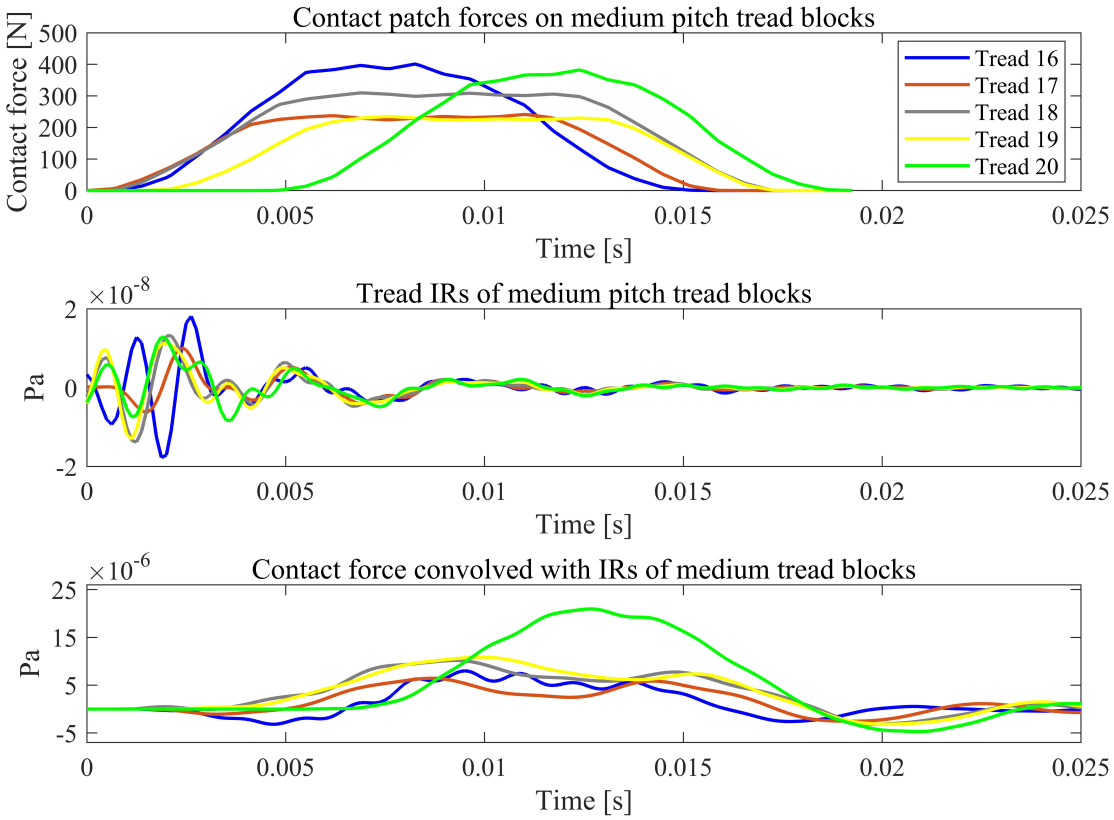

Figure 5.9: Convolved response for the medium pitch tread blocks for the loaded tyre that is inflated at 2.4 bar and rolling at 30 kph. The tyre loading force is 5000 N. Refer Figure 5.8b for the footprint of the loaded tyre that is rolling at 30 kph with inflation pressure of 2.4 bar. Refer Figure 5.1b for the illustration of medium pitch tread set/block for the unloaded tyre.

5.1.3 Concatenation of the convolved IRs for rolling noise

The penultimate step in this work is to concatenate the convolved IRs to mimic the tyre rolling condition. To achieve this, firstly, it should be made clear to the reader that the tyre itself is not rolling in the simulations. The convolved noise is played back in a sequence that is defined by tread randomisation, generated by the tyre manufacturer. A tabulated representation of tread randomisation as provided by the tyre manufacturer is shown in Appendix B Table B.1. In this table, pitch no. refers to the tread set types, where 1, 2 and 3 correspond to small, medium and large pitch tread block sets, respectively. Refer Figure 5.1 for the details on the pitch tread sets.
Concatenation of the convolved IRs or henceforth, the impact noise for the modelling of rolling noise is performed in two steps:

Cette thèse est accessible à l'adresse : https://theses.insa-lyon.fr/publication/2022ISAL0081/these.pdf
© [B. Anantharamaiah], [2022], INSA Lyon, tous droits réservés

- concatenation of the impact noise of individual treads blocks from tread sets of various pitch sizes to generate combined impact noise from tread sets and
- concatenation of these combined impact noises from tread sets using the tread randomisation sequence to generate the tyre rolling noise for various rolling speeds.

Concatenation of the impact noises of individual tyre tread blocks of a tread set

Tyre tread can be imagined as a set of treads, separated by a small gaps between them as shown in Figure 5.1d. In the process of concatenation, each tread set is (imaginarily) impacted with the duration of its corresponding force along with the delay between two successive tread blocks of the same tread set. This pictorial representation of tread concatenation is shown in Figure 5.10. In this process, although the individual tread impact noises used for the concatenation process are considered from the loaded tyre that is inflated to various pressures, the concatenation algorithm do not consider the sequence in which the tread blocks are excited at the contact patch of the tyre-road interface.
The concatenated impact noise for the medium pitch tread set of the tyre with inflation pressure of 2.4 bar is shown in Figure 5.11. The same for the small and the large pitch tread sets are shown in Appendix B Figures B.4 and B.5, respectively.

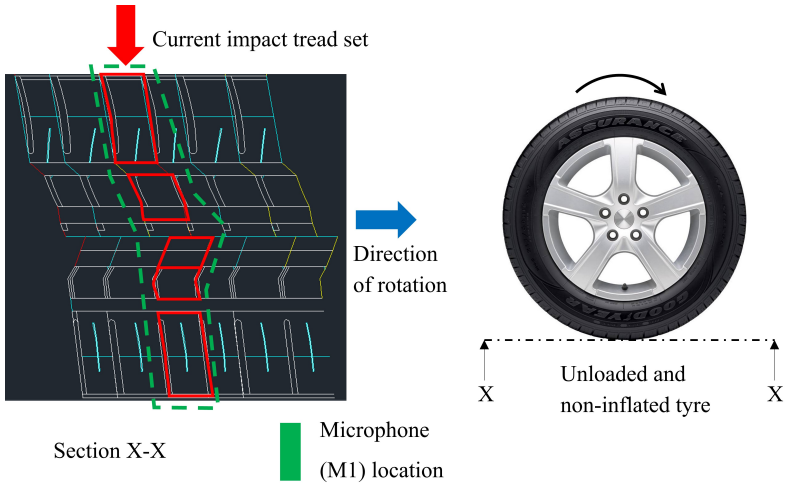

Figure 5.10: The process of concatenation of the rubber block noise. The locations of the impact and the microphone remain unchanged. However, the convolved IRs from the next tread set is concatenated with the current tread set after considering the delay (due to tread gap, refer Figure 5.1d) between two successive rubber block and/or tread set impacts at the leading end of the contact patch using MATLAB®. Tyre model for representation purpose only.

Concatenation of the impact noises of tread blocks of various pitch size of the tyre to generate rolling noise

Once the impact noise of each tread sets are generated, they are further concatenated mutually based on the randomisation sequence (as described in Appendix B Table B.1) to generate the tyre rolling noise. During this step of concatenations, impact noises of some of the tread blocks from the successive tread set overlap with the current tread set. This is because, the forces do not act according to the concatenation sequence as defined by Figure 5.10 but according to impacts over the treads at the contact patch as depicted in Figure 5.8. From this figure, it can be observed that the treads in the center are impacted ahead of the ones at the edges. This is also fortified by the force behaviour that is determined from the tyre rolling simulations in Figure 5.9. From this figure, it is clear that the force acting on tread block 20 is delayed the most. Once

Cette thèse est accessible à l'adresse : https://theses.insa-lyon.fr/publication/2022ISAL0081/these.pdf
© [B. Anantharamaiah], [2022], INSA Lyon, tous droits réservés

the combined impact noise of this tread set (that contains tread block 20) is concatenated with the succeeding one, the forces that act on the central tread blocks of the succeeding tread set would have already generated the impact noise. These impact noise contributes to the impact noise from the current tread set thus ensuring that the noise generated from the leading end of the tyre contact patch is precisely modelled during the tyre roll.
Such process of concatenation is performed for all the cases of the tyre pressure and rolling speeds considered and the corresponding tyre rolling noise generated are subjected to listening tests.

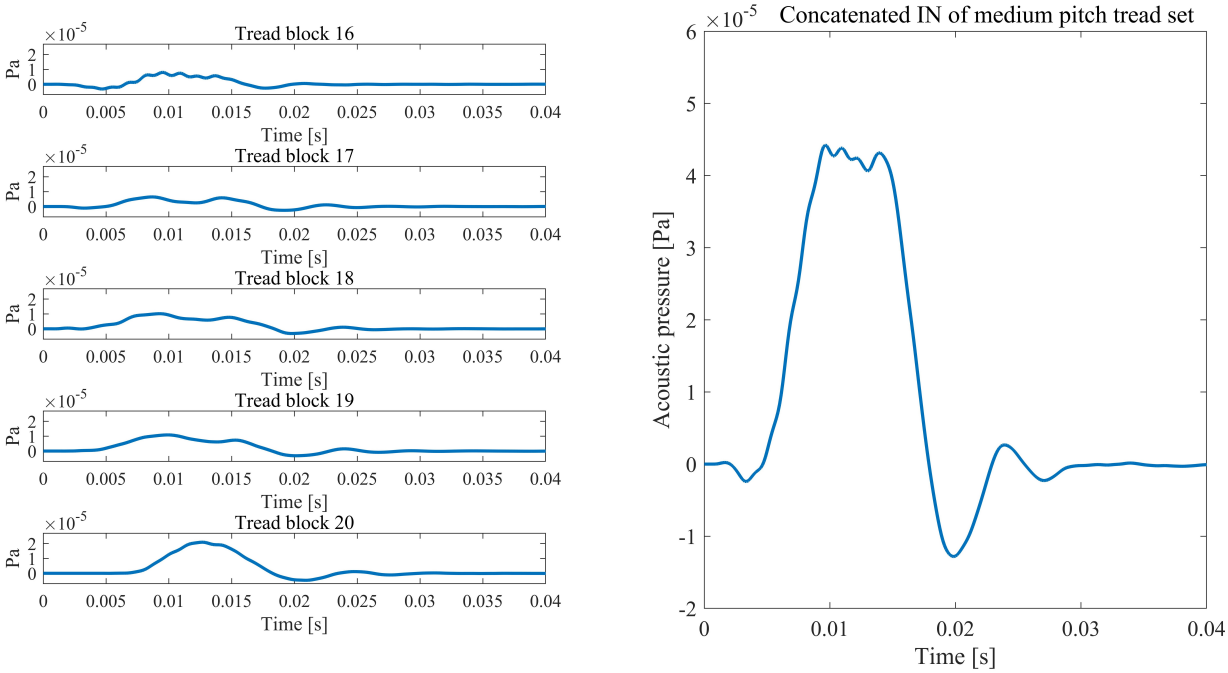

Figure 5.11: Convolved IR for rubber blocks of medium pitch tread set (left) and impact noise (IN) of the medium pitch tread set as a result of concatenation of convolved IRs of individual rubber blocks of the same tread set (right).

5.2 Tyre noise psychoacoustic test

This section speaks about the setup for the ultimate goal of this work - tyre noise psychoacoustic perception study. Listening tests are performed in the silent room at the Laboratoire Vibrations Acoustique de l'INSA Lyon (LVA). A total of eighteen audio files - nine each from rolling simulations and rolling tests (combination of three different inflation pressures and three different rolling speeds) are assessed for their unpleasantness by 29 listeners. The aim is to detect the possible distinction between rolling noise of tyres comprising of different rolling conditions. These listeners are made to participate in the listening test one after the other. Post the tests, the grading from the listeners are used to check the possible correlation between the unpleasantness of the measured rolling noise with that of the synthesised rolling noise from the simulations of the tyre. The measurement of rolling noise from tests is briefly described in Section 5.3. An audio playback system is used to play the tyre rolling audio files for the listeners. In this system, the sound card level was adjusted such that sound pressure level of the audio file of the tyre with 2.1 bar inflation pressure that is rolling at 30 kph is 71 dB when measured at the ears of the dummy head (refer Figure 5.12a). The initial setup and the example of the environment inside the silent chamber of LVA are shown in Figure 5.12.
In each test, the listeners are provided with a circumaural high quality electrodynamic head-

Cette thèse est accessible à l'adresse : https://theses.insa-lyon.fr/publication/2022ISAL0081/these.pdf
© [B. Anantharamaiah], [2022], INSA Lyon, tous droits réservés

phone (Sennheiser HD 650) for the test which is conducted inside the silent room. They are given access to a custom designed audio *playback tool* that offers them options to *play*, *replay* and *switch* to next audio sample as shown in Figure 5.12b.

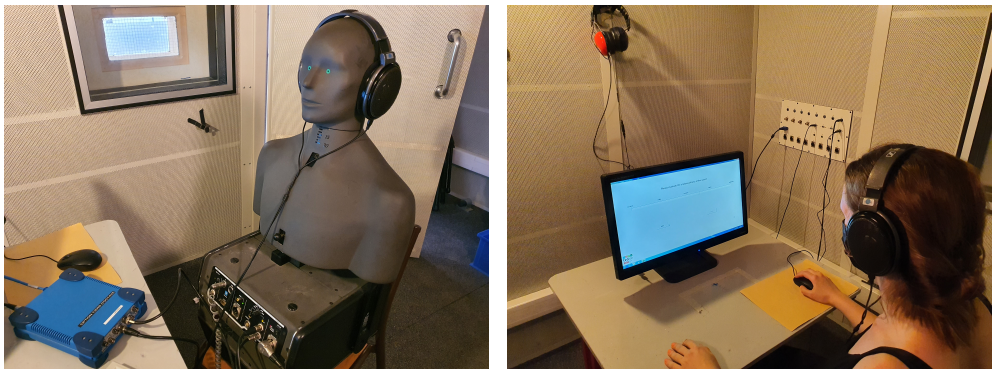

(a) (b)

Figure 5.12: Tyre noise psychoacoustic test in the silent chamber of LVA - (a) Initial test setup using an audio measuring dummy and (b) a typical listening test.

The audio files are played under two categories - rolling test audio and rolling simulation audio. The acquisition conditions for the tyre rolling audios in the test is explained in the following section. The listening test begins for every listener in an alternate sequence of these categories, i.e. if the first listener starts the listening test with rolling test audio, then the second listener starts with rolling simulation audio. Also, the nine audio files in each of these categories are randomly played for listeners during each listening test. Rule in the playback tool is set in such a way that each audio file can be replayed as many times as necessary until the listener is confident enough to assess it. However, once an audio file is graded and switched to the next one, the listener is not allowed to roll back to the previous audio for re-assessment. The listeners assess the audio files based on the feeling of unpleasantness on a continuous categorical scale under five categories - *not at all*, *a little*, *medium*, *highly* and *extremely*. Statistically, these options are ranked between -1 (for not at all) to 1000 (for extremely).

5.3 Results and discussion

In order to verify the credibility of the audio files of the synthesised tyre rolling noise, it is necessary to compare their attributes such as spectral power with that of the rolling audio files from the measurements. The rolling noise of the tyre is measured in the hemi-anechoic chamber at IDIADA, the setup of which is shown in Figure 5.13a. In this figure, the position of the microphone M1 remains the same as in the case of static noise measurement (refer Figure 5.2). The noise from the rolling tyre as shown in Figure 5.13a is measured for three speeds and inflation pressures for a vehicle load of 5000 N (corresponding to F_l in Figure 5.2a) with a sampling frequency of 32 kHz. A comparison of the spectral powers of octave bands (hereby also spectral powers) between the synthesised and the measured rolling noise of the tyre inflated at 2.4 bar that is rolling with a linear velocity of 30 kph is depicted in Figure 5.13b.
From Figure 5.13b, it can be observed that the spectral power of the synthesised tyre rolling noise matches well with that of the test. However, there are small discrepancies at the extreme limits of the curves. These are mainly due to the fact that the frequency content from the measurements was up to 16 kHz (sampling frequency 32 kHz) and it had to be filtered to obtain the audio files whose frequency content ranges between 10 Hz to 1000 Hz. Similar behaviour can also be observed in the spectral powers for tyre rolling with same speeds but 2.1 bar and 2.7 bar inflation pressures in Figure 5.14.

Cette thèse est accessible à l'adresse : https://theses.insa-lyon.fr/publication/2022ISAL0081/these.pdf
© [B. Anantharamaiah], [2022], INSA Lyon, tous droits réservés

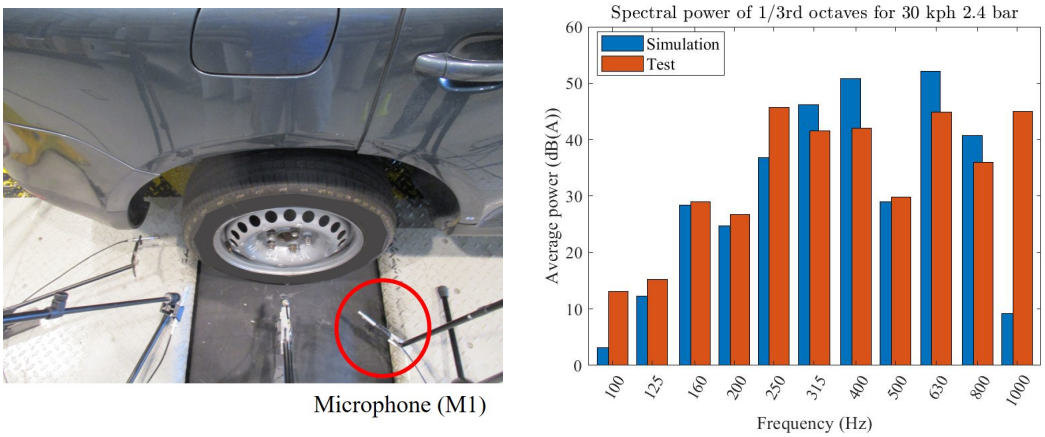

(a) (b)

Figure 5.13: Measurement and assessment of tyre rolling noise (a) Measurement of tyre rolling noise at hemi-anechoic chamber in IDIADA. For details about the location of microphone M1, refer Figure 5.2; and (b) comparison of the average power of one-third octave bands between the synthesised and measured rolling noise for a tyre inflated at 2.4 bar that is rolling with a linear velocity of 30 kph. X-axis values correspond to central band frequencies.

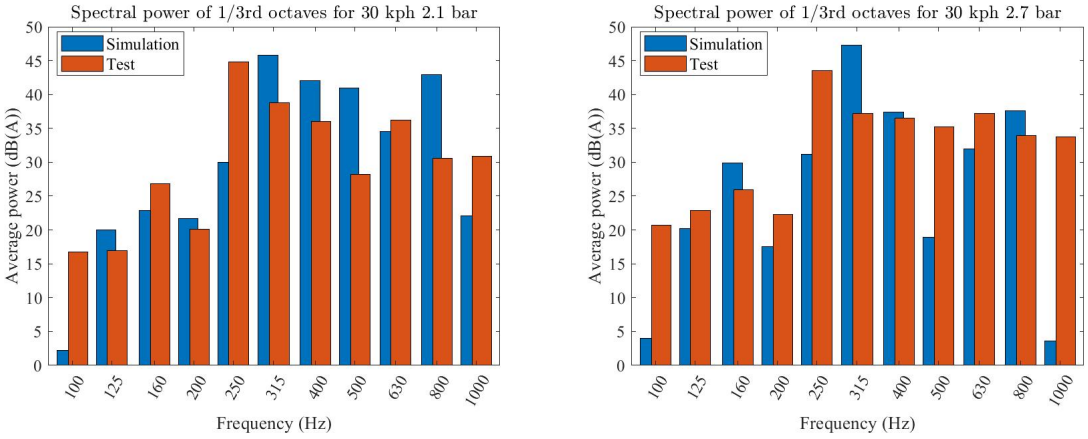

(a) (b)

Figure 5.14: Comparison of the average power of one-third octave bands between the synthesised and measured rolling noise for a tyre inflated at (a) 2.1 bar and (b) 2.7 bar with a linear velocity of 30 kph. X-axis values correspond to central band frequencies. Vehicle load remains constant with 5000 N.

The comparison of spectral powers for other tyre rolling conditions considered are shown in Appendix B Figures B.6 and B.7.

Unpleasantness in tyre rolling noise

The audio files measured from a rolling tyre are played in the listening test and the corresponding grading of unpleasantness is obtained as a feedback from 29 listeners. This grading is shown in Figure 5.15a. From this figure, it can be observed that the unpleasantness is not uniform for all tyre rolling cases. For example, the grading of unpleasantness is increasing for the tyre rolling with inflation pressure of 2.1 bar and 2.7 bar. However, the same for 2.4 bar is the highest when the tyre is rolling at 40 kph and the least when rolling at 30 kph. Although these

Cette thèse est accessible à l'adresse : https://theses.insa-lyon.fr/publication/2022ISAL0081/these.pdf
© [B. Anantharamaiah], [2022], INSA Lyon, tous droits réservés

behaviours are observed, the probability of distinguishing the unpleasantness among the tyre rolling noise samples is very faint for a constant rolling speed. The likelihood of distinguishing the unpleasantness is good for the following cases - (a) tyre with inflation pressure of 2.4 bar rolling at 30 kph, (b) between tyres rolling at 40 kph with 2.4 bar and 2.1 bar and (c) tyre inflated at 2.7 bar that is rolling at 50 kph.

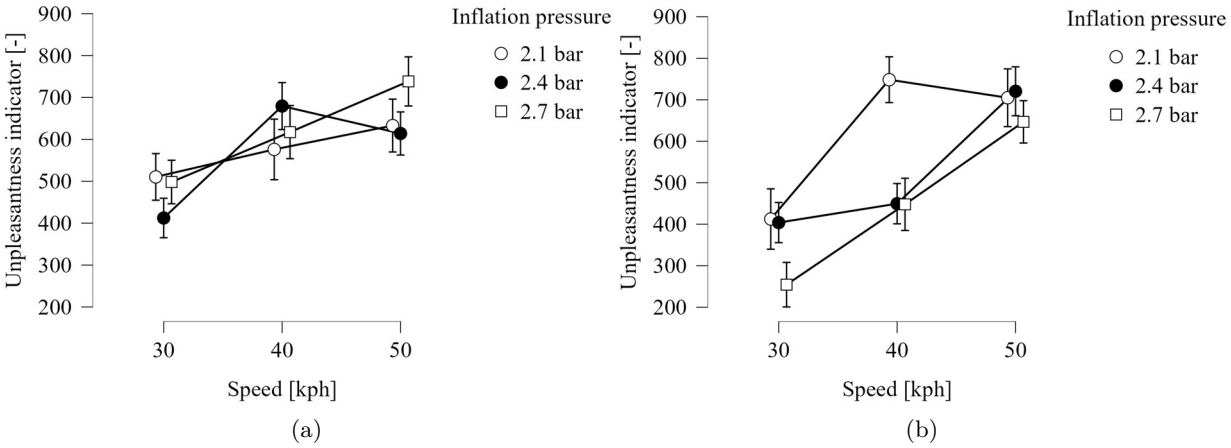

Figure 5.15: Unpleasantness in (a) measured and (b) synthesised tyre rolling noise for various conditions as obtained from the listening test at LVA, INSA Lyon. On the y-axis, 200 denotes least unpleasantness and 900 denotes high unpleasantness.

Extending the same analogy to the results from the listening tests of the rolling noise of the synthesised tyre, it can be observed from Figure 5.15b, that the unpleasantness of the tyre rolling at 50 kph can be vaguely distinguished from other inflation pressures for the tyre with inflation pressure of 2.7 bar. However, for the case of tyre rolling at 40 kph and 30 kph, only the cases with inflation pressures of 2.1 bar and 2.7 bar, respectively can be distinguished from others. Following key conclusions can be drawn from the unpleasantness perception for the measured tyre rolling noise from Figure 5.15a:

- the tyre rolling at 30 kph and 50 kph with 2.4 bar and 2.7 bar inflation pressure, respectively offer the highest variations in terms of unpleasantness for the tyre considered;
- the second highest number of variations is exhibited by the tyre inflated to 2.4 bar that is rolling at 40 kph and
- irrespective of rolling speeds, the tyre with an inflation pressure of 2.1 bar offers the least variations in terms of unpleasantness.

Similar set of conclusions on unpleasantness as graded for synthesised tyre rolling noise as shown in Figure 5.15a can be drawn:

- the tyre rolling at 30 kph with 2.7 bar inflation pressure offers the highest variation in terms of unpleasantness for the tyre noise synthesised;
- the second highest number of variation is exhibited by the synthesised noise of the tyre rolling at 40 kph and 50 kph inflated to 2.1 bar and 2.7 bar, respectively and
- the rest of the cases offer equal number of variations in unpleasantness.

From the interpretation and analysis of the results obtained, it is quite clear that the distinction of unpleasantness of the synthesised tyre rolling noise does not represent the same from the

Cette thèse est accessible à l'adresse : https://theses.insa-lyon.fr/publication/2022ISAL0081/these.pdf
© [B. Anantharamaiah], [2022], INSA Lyon, tous droits réservés

measured noise of the rolling tyre. To identify the possible cause that is leading to this discrepancy, it is necessary to understand the grading of unpleasantness for the tyre rolling speeds and inflation pressures separately. Figure 5.16 provides an insight on the discrepancies in the unpleasantness observed due to tyre inflation pressure and rolling speeds separately.

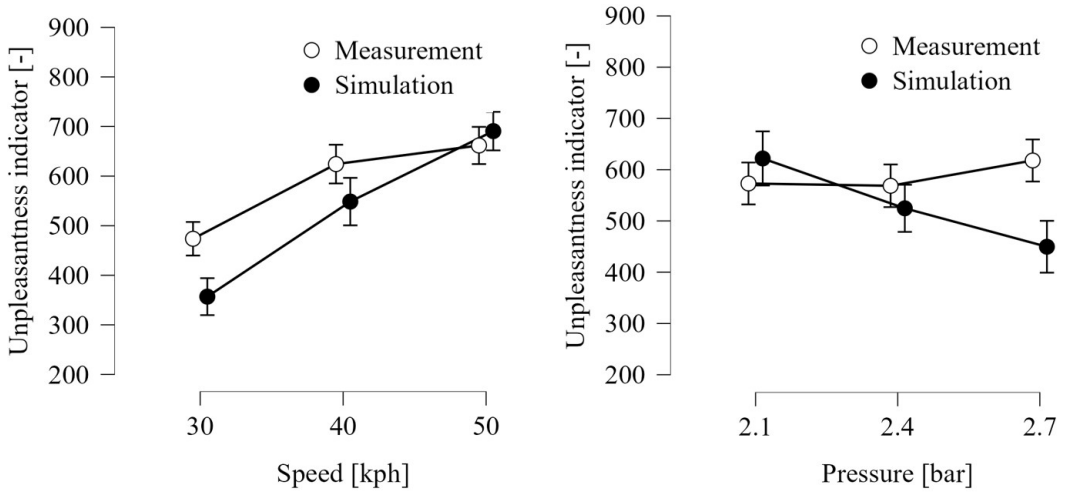

Figure 5.16: Distinction between unpleasantness experienced by listeners for (a) various tyre rolling speeds and (b) for various inflation pressures of the tyre. On the y-axis, 200 denotes least unpleasantness and 900 denotes high unpleasantness.

From Figure 5.16a, it can be observed that the unpleasantness grading from the listeners were congruent in terms of tyre rolling speeds, although the level of unpleasantness was lower in synthesised rolling noise (mentioned as simulation in the plot legend) than the measured one for 30 kph. On the other hand, from Figure 5.16b, the unpleasantness perception has good agreement at lower inflation pressures but not at higher values. The unpleasantness in measured rolling noise shows an uptrend with increase in pressure but the same for synthesised rolling noise (shown as simulation in the legend) is in downtrend. Hence, the discrepancy in the listening test is due to the unreliability in the grading of tyre noise unpleasantness due to variations in tyre inflation pressures. The root cause for this unreliability can be associated with the loudness of the audio files. A comparison of the loudness (in sones) of the audio files is depicted in Figure 5.17.

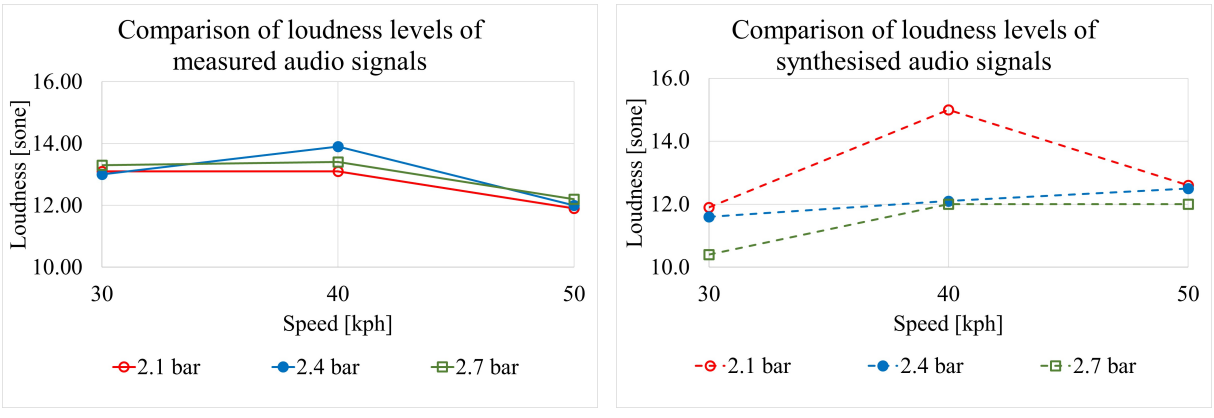

Figure 5.17: Comparison of loudness in (a) test and (b) synthesised audio files of rolling tyres.

Cette thèse est accessible à l'adresse : https://theses.insa-lyon.fr/publication/2022ISAL0081/these.pdf
© [B. Anantharamaiah], [2022], INSA Lyon, tous droits réservés

Comparing Figure 5.17a with Figure 5.15a and Figure 5.17b with Figure 5.15b, it can be observed that the loudness levels of the measured and synthesised rolling tyre audio files have a direct influence on the unpleasantness of the tyre rolling noises. Hence the discrepancies in the unpleasantness that is evaluated by the listeners is attributed to the levels of the audio that is perceived in the listening tests. A possible solution to address the problem with different loudness levels, particularly during the generation of synthesised audio files, is recommended as a future task of this work. Additionally, from Appendix B Figures B.8 and B.9, it can be observed that sharpness and roughness of the audio files has no concrete correlation with the unpleasantness grading of the audio files, although the loudest case has the highest roughness. It is also clear that the synthesised model of the tyre with inflation pressure of 2.1 bar, irrespective of rolling speeds, has a higher loudness level compared to all other audio files. For this case, the loudness level depicts similar behaviour as other cases but increases abruptly for the rolling speed of 40 kph. This impacts the listeners psychologically while grading the unpleasantness of other audio files. Referring to Figure B.6b in Appendix B, the reason for the high value of RMS level can be attributed to:

- average higher spectral powers in the audio file of the synthesised tyre rolling noise than the measured audio in the range of 125 Hz to 250 Hz and
- higher amplitude and number of peaks/tones in the audio file of the synthesised tyre rolling noise than the measured audio for the spectrum considered.

In an attempt to understand this behaviour, the amplitude of forces used for the convolution step, process of convolution and concatenation, IR and NTF levels of the treads are cross-verified. However, there are no data or procedural errors observed. As a corollary, if the discrepancy is with 40 kph 2.1 bar tyre rolling case, then the same must be reflected on to 50 kph and 30 kph tyre rolling with an inflation pressure of 2.1 bar. This however, is not the case. Hence it should be accepted that the behaviour of the loudness curves as shown in Figure 5.17, especially for the case of tyre rolling at 40 kph with inflation pressure of 2.1 bar, is correct.

5.4 Conclusions

In this chapter, the main objective set for this work has been verified for its credibility, i.e. whether a deterministic tyre model can be developed using FEM to synthesise the tyre rolling noise. Additionally, its applicability in perception of its unpleasantness was also cross-verified with the tyre rolling noise measured from tests. The tyre noise files were synthesised for various combinations of tyre rolling speeds, namely - 30 kph, 40 kph and 50 kph with inflation pressure values of 2.1 bar, 2.4 bar and 2.7 bar. The rolling noise synthesised using these combinations were compared with the corresponding rolling noise measured in the hemi-anechoic chamber in IDIADA.
First and foremost, the impulse response of the rolling tyre was measured for the combinations of cases as discussed in this chapter using a microphone placed at a predetermined location. In the FE model, the tyre was impacted at the leading edge of contact patch on each tread of a rubber/tread block to determine its output NTF for various tyre inflation pressures of 2.1 bar, 2.4 bar and 2.7 bar. These NTFs were measured at a node (in the FE using submodelling technique) whose position was same as that of the microphone used in the measurement of the tyre rolling noise test. Each of these NTFs were converted to IRs using IFFT technique. The corresponding forces acting on each tread during the tyre roll over a drum was determined using FE simulations. These forces were convolved with their corresponding IRs. Based on the contact patch and tread randominsation patterns, the convolved tread IRs obtained were concatenated using MATLAB®. This concatenation process took into account the time duration for which each tread experiences contact patch forces for various rolling speeds of 30 kph, 40 kph and

Cette thèse est accessible à l'adresse : https://theses.insa-lyon.fr/publication/2022ISAL0081/these.pdf
© [B. Anantharamaiah], [2022], INSA Lyon, tous droits réservés

50 kph along with the time difference between successive tread impacts. As a result, 18 tyre rolling audio files - 9 from measurements and 9 synthesised using convolution and concatenation procedure, were generated. Finally, these audio files were subjected to listening tests in which 29 listeners graded them based on their perception of unpleasantness.
From the listening test, it was found that the difference in the unpleasantness between any two tyre rolling audio signals in measurements, for the same inflation pressure, could be identified by paying *acute* attention to the audio. However, it is possible to detect the unpleasantness of the tyre rolling noise for different inflation pressures. The tyre rolling at 30 kph and 50 kph with 2.4 bar and 2.7 bar inflation pressure, respectively offered the highest variations in terms of unpleasantness for the tyre considered. The second highest number of variations was exhibited by the tyre inflated to 2.4 bar and rolling at 40 kph. Finally, it was observed that, irrespective of rolling speeds, the tyre rolling with an inflation pressure of 2.1 bar offered the least variations in terms of unpleasantness.
From the listening test results of synthesised tyre rolling noise, it was found that the tyre rolling at 30 kph with 2.7 bar inflation pressure offered the highest variation in terms of unpleasantness for the tyre noise. The second highest number of variations was exhibited by the synthesised noise of the tyre rolling at 40 kph and 50 kph inflated to 2.1 bar and 2.7 bar, respectively. The rest of the cases offered equal number of variations in unpleasantness. Based on the observations it can be concluded that the developed FE tyre model:

- has the credibility to reproduce the unpleasantness of the tyre rolling noise at different speeds and
- requires further work for in-depth understanding on the unpleasantness of the tyre rolling noise generated from the FE simulations with respect to variation in tyre inflation pressures. This is mainly due to unaccounted loudness levels observed in some of the cases of the synthesised tyre rolling audio files of different tyre inflation pressures.

It was found that the loudness of the audio files, both from tests and synthesised, influenced the perception of their corresponding unpleasantness in tests. Particularly with respect to synthesised audio files, there were discrepancies observed in the loudness levels. The loudness of the audio files of the tyre rolling with an inflation pressure of 2.1 bar and 2.7 bar had fairly congruence in test and synthesised cases. However, the same for the case of tyre with an inflation pressure of 2.1 bar had no match; the loudness of the synthesised audio files was higher than that of the tests. Apart from this, other attributes like roughness and sharpness of the audio files had no influence over the unpleasantness grading.
In order to overcome the observed discrepancies in the unpleasantness grading, it is necessary to control the loudness levels during the synthesis of the audio files, which was not made during the current study. This is the most important recommendation as future work in order to improve the accuracy in unpleasantness grading and correlation of the same between the measured and synthesised tyre rolling audio files.

Cette thèse est accessible à l'adresse : https://theses.insa-lyon.fr/publication/2022ISAL0081/these.pdf
© [B. Anantharamaiah], [2022], INSA Lyon, tous droits réservés

General Conclusions and Perspectives

Discussion and conclusion

The noise from a moving automotive that is perceived by pedestrians is collectively called exterior noise or Pass-by Noise (PBN). Automotive PBN is an important factor that influences the vulnerable road user (VRU) safety or pedestrian safety. With the implementation of next generation Electric Vehicles (EVs) in which the PBN is next to nothing due to the absence of an engine, the safety of VRUs, especially the blind, bicyclists and children is of utmost concern. As a result, the European Union has established a regulation (Regulation (EU) No 540/2014) to car manufacturers that all new electric cars must be equipped with an adequate noise source to enhance safety. However, the addition of this noise source to a car comes at an extra cost to customer.

Considering the contribution of engine and tyres to PBN, it is seen that for lower car speeds, the engine noise dominates that of tyres and is vice versa at higher speeds. This means that tyres are also one of the major contributors to the pass-by noise of a car. Although several investigations have been carried out on tyre noise, there existed no deterministic studies on its efficient design, especially on its acoustic perception with respect to pedestrian safety. The objective of this work is to develop a numerical model of the tyre that assists in modelling, generation, propagation and perception of the its rolling noise. This thesis has explored the factors, especially from material, rolling speeds and inflation pressure perspectives, that influence the noise generated by tyres, in order to enhance the psychoacoustic perception of a car at low speeds.

Major challenge in modelling tyres in a numerical tool is the lack of reliable information on rubber material properties, i.e. hyperelasticity and viscoelasticity. Although a rubber manufacturer can provide this information, it will merely describe the behaviour of rubber in its standard testing condition, i.e of a particular shape of the specimen tested at a predefined temperatures and pressures. During the manufacturing process of a tyre, the constituent rubbers undergo curing process in which they are subjected to high pressures and temperatures. Due to this, the rubber behaviour will not be the same as measured in the standard testing conditions. To overcome this challenge effectively, an attempt is made through this work to determine the properties of rubbers, esp. hyperelasticity (or rubber hardness expressed in shoreA values) and viscoelasticity using the responses of the tyre from static and dynamic tests as opposed to employing any pre-defined material data in numerical simulations.

For the determination of properties of rubbers, a simplified and innovative axi-model of the tyre is developed in a numerical tool which was later revolved to obtain a 3D tyre model. In the axi-model, the rubbers were identified based on their dynamic mechanical analysis (DMA) behaviour data and segregated in terms of their dominance in the local regions of the tyre. Once these dominant rubbers were identified, the other rubbers were merged with these to result in

Cette thèse est accessible à l'adresse : https://theses.insa-lyon.fr/publication/2022ISAL0081/these.pdf
© [B. Anantharamaiah], [2022], INSA Lyon, tous droits réservés

simplified rubber regions. In the current tyre, the total number of rubbers were reduced from eleven to six based on this process. This simplified model was used in the DoE process in which the rubber hardness/ hyperelasticity was randomly sampled using the Latin hypercube sampling (LHS) technique to arrive at an optimised tyre model that predicted the tyre characteristic behaviour as measured in the tests. Reduction in the number of the rubber regions of the tyre not only aided in FE model simplification but also reduced the DoE optimisation time since, in general, the minimum samples required to optimise a system in DoE process is a function of sampling variables of the same.

On the determination of rubber hyperelasticity and its influence on tyre overall behaviour

To determine the rubber hyperelasticity, the static responses, e.g. radial, lateral and longitudinal stiffness from the numerical tyre model were compared and calibrated with that of the physical tyre. A DoE technique was used in this process. Firstly, the static responses of the physical tyre were determined using a stiffness measurement machine. Next, using DoE approach, 45 samples of simplified tyre model were generated by varying the rubber hyperelasticity (hardness) values of the six rubber regions. For this sample generation process, the Latin Hypercube sampling (LHS) technique was used. These numerical tyre models were loaded in radial, lateral and longitudinal directions (with identical boundary and loading conditions as in stiffness measurement tests) to determine their respective stiffness. The numerical tyre model that offered a promising match between the stiffness in tests and simulation was selected for the rest of the work. DoE technique non only lead to optimised hardness values of the tyre rubbers that minimised the error between the tyre stiffness in simulation and tests but also offered a systematic segregation of the contribution of individual rubber regions to the tyre static and dynamic behaviour studies.
From the tyre static behaviour study, it was found that the hardness of the carcass rubber dominates the overall tyre stiffness, i.e. lateral, longitudinal and radial, for two reasons - (a) carcass rubber runs between bead to bead of the tyre, thus forming a skeleton of the tyre and (b) it is the main component per volume of the tyre. Hyperelasticity of carcass plies influenced the tyre radial and lateral stiffness, whereas that of cap plies influenced the tyre lateral stiffness. This is due to their stiffening effects in the corresponding loading directions. The shoulderwedge and the sidewall rubber hardness induced moderate effect on the tyre static behaviour whereas tread, apex and rimcushion rubber hardness imparted trivial influence.
Following the tyre static study, the vibrational dynamic behaviour of the tyre was also studied. For this, a free-free tyre was setup and the point inertances (PI), vibrational and noise transfer functions were determined in the tests. During the post processing of the modal data test, it was found that the tyre is a highly damped system. The tyre modal density increased considerably beyond 300 Hz. Hence, in order to study the influence of rubber hyperelasticity on tyre dynamic behaviour, the frequency limit of interest was set to 200 Hz. In this limit, five Eigen modes and their corresponding Eigen frequencies were identified. Using the optimised FE tyre model, the influence of each rubber region on these Eigen modes were studied using DoE technique. In this process, the FE model was setup with identical boundary conditions as in the free-free modal and noise test with same definitions of impact, point inertance and transfer function measurements. The constituent rubber hyperelastic properties were sampled using LHS technique and their contribution to the tyre dynamic behaviour was studied.
The modal damping factor for each of the Eigen mode was determined from results of the post-processing of the test data using polyreference least-squares complex frequency-domain (p-LSCFD) method in LMS Testlab® software. These values were also incorporated into the optimised model and the credibility of the results from tyre modal DoE study was verified in tyre dynamic behaviour studies.
Tyre dynamic behaviour study showed that the key contributors for the tyre Eigen modes and

Cette thèse est accessible à l'adresse : https://theses.insa-lyon.fr/publication/2022ISAL0081/these.pdf
© [B. Anantharamaiah], [2022], INSA Lyon, tous droits réservés

thus the noise are the carcass and the sidewall rubbers hardness. From the DoE results, it was found that the hardness of the carcass rubber dominates the Eigen frequency of tyre modes and noise transfer function at higher range of frequency considered (200 Hz), whereas the hardness of the sidewall rubber dominates the lower ones. The contribution of the apex and the hardness of the rimcushion rubber was negligible, while the tread and the hardness of the shoulderwedge rubber offered no contribution to the tyre modal and noise behaviour. From the outcome of this study, it was observed that, if the tyre dynamic behaviour has to be modelled for up to 1 kHz, it is advisable to estimate and introduce rubber material based damping, i.e. rubber viscoelasticity. The implementation of material based damping and the associated outcomes are discussed in the following subsection.

On the determination of rubber viscoelasticity and modelling of static tyre impact noise

The rubber viscoelasticity can be introduced into the model through various definitions, however in this work, it was defined as Prony series, specifically in terms of Prony parameter (g_i). It is used as a term in Abaqus® solver to define the viscoelastic damping of rubbers for a given set of frequency ranges, which in the current work was 10 Hz to 1 kHz. For every rubber of the tyre, value of these parameter were estimated from fitting the experimental DMA data with that of a theoretical equation which was expressed in terms of Prony delta or loss angle. While the experimental data was expressed as a mathematical relation between loss angle and rubber shore hardness, the theoretical expression, that defines the Prony series in Abaqus® software, established a relation between the loss angle and the Prony parameters. Once the Prony parameters were determined using this technique, they were incorporated into FE simulation to predict the tyre modal and noise behaviour.
For the study on tyre modal and noise behaviour, the free-free tyre and the loaded tyre were considered. The locations of impact/excitation and the measurements of PI in the free-free tyre remained the same as in the dynamic behaviour analysis that was performed to characterise the rubber hyperelasticities. In case of loaded tyre, a static radial load of 5 kN was applied on the tyre. In the modal study, the tyre was excited in its loaded condition using a shaker at a location approximately 60° from the contact patch. In case of noise measurement of a loaded tyre, the same location was impacted using a hammer in order to eliminate the noise that is generated due to the excitation of the shaker coil.
From the results of tyre dynamic simulations, it was observed that there was a very good correlation in tyre PIs with test up to 1 kHz for the loaded tyre and 500 Hz for the free-free tyre (the limit of comparison for the free-free tyre was only up to 500 Hz due to the drop in coherence beyond this frequency limit). Along with the tread excitation, the sidewall excitation was also studied for the loaded tyre case. It was found that PI due to sidewall excitation in test depicted higher amplitude in acceleration which was a result of added mass effects from the shaker. Nevertheless, the level of PIs stood comparable in test and simulation.
From the noise simulations for the loaded tyre, it was observed that there was a good correlation between the output NTFs of test and simulation up to 450 Hz beyond which there was a constant drop of 10 dB up to 1 kHz in the simulations. This difference seemed to be caused by limitations in the FE noise propagation model to precisely predict the acoustic reflections that was observed in the measurements. The FE model was sensitive to variations in inflation pressure, even though these variations were trivial. It should be noted that such small differences in output NTF responses caused by small variations in tyre pressures could not lead to any concrete conclusions regarding the robustness of the correlation.
With the model developed in this work, it was concluded that the essential material properties of the tyre rubbers necessary to model the tyre static and dynamic behaviours were well characterised. By employing these, the next objective was to model the rolling noise of the tyre and subjecting it to listening tests. To achieve this, the principle of convolution (of output NTF

Cette thèse est accessible à l'adresse : https://theses.insa-lyon.fr/publication/2022ISAL0081/these.pdf
© [B. Anantharamaiah], [2022], INSA Lyon, tous droits réservés

with input contact force on treads at contact patch) and concatenation was used to synthesise the tyre rolling noise instead of actually rolling the tyre in simulations.

On the modelling of tyre rolling noise and psychoacoustics

The FE tyre noise model that was developed in this work was checked for its applicability to the perception of unpleasantness of the tyre noise. The rolling noise measured from tests was used for validate the rolling noise of tyres that were synthesised from FE simulations. The audio files of the tyre noise were synthesised from simulations for various combinations of tyre rolling speeds, namely - 30 kph, 40 kph and 50 kph with inflation pressure values of 2.1 bar, 2.4 bar and 2.7 bar. The rolling noise synthesised using these combinations were compared with the corresponding rolling noise measured in the hemi-anechoic chamber in IDIADA.
With regard to measurements, the rolling noise of the tyre was measured for the combination of cases considered using a microphone placed at a predetermined location near the leading edge of the rolling tyre. In the FE model, the tyre was excited at the contact patch on each rubber block of the tread set to determine its output NTF for various tyre inflation pressures of 2.1 bar, 2.4 bar and 2.7 bar. These NTFs were measured at a node (in the FE using submodelling technique) whose spatial position was the same as that of the microphone used in the measurement of the tyre rolling noise in test. Each of these NTFs were then converted to IRs using IFFT technique. The forces acting on each tread during the tyre roll over a drum was determined using FE simulations. These forces were convolved with their corresponding IR for the same tread. Based on the contact patch and tread randominsation patterns, the convolved tread IRs obtained were concatenated using MATLAB®. This concatenation process took into account the time duration for which each tread experiences contact patch forces for various rolling speeds of 30 kph, 40 kph and 50 kph along with the time difference between successive tread impacts. As a result, 18 tyre rolling audio files - 9 from measurements and 9 synthesised using convolution and concatenation procedure, were generated. Finally, these audio files were subjected to listening tests in which 29 listeners graded them based on their perception of unpleasantness.
From the listening test, it was found that the difference in the unpleasantness between any two tyre rolling audio signals in measurements, for a given inflation pressure, could be identified by paying *acute* attention to the audio. However, it was possible to detect the unpleasantness of the tyre rolling noise for different inflation pressures for some of the cases. The tyre rolling at 30 kph and 50 kph with 2.4 bar and 2.7 bar inflation pressure, respectively offered the highest variation in terms of unpleasantness for the tyre considered. The second highest number of variations was exhibited by the tyre inflated at 2.4 bar that was rolling at 40 kph. Finally, it was observed that, irrespective of rolling speeds, the tyre rolling with an inflation pressure of 2.1 bar offered the least variation in terms of unpleasantness.
From the listening test results of the synthesised tyre rolling noise, it was found that the tyre rolling at 30 kph with 2.7 bar inflation pressure offered the highest variation in terms of unpleasantness of the tyre noise. The second highest number of variations was exhibited by the synthesised noise of the tyre rolling at 40 kph and 50 kph inflated to 2.1 bar and 2.7 bar, respectively. The rest of the cases offered equal number of variations in unpleasantness. Based on the observations it can be concluded that the FE tyre model developed in this work:

- has the credibility to reproduce the unpleasantness of the tyre rolling noise at different speeds and
- requires further work for in-depth understanding on the unpleasantness of the tyre rolling noise generated from the FE simulations with respect to variation in tyre inflation pressures. This is mainly due to unaccounted loudness levels observed in some of the cases of the synthesised tyre rolling audio files of different tyre inflation pressures.

In general, by analysing the loudness level, sharpness and roughness of the audio files, it was observed that the loudness of the audio files, both from tests and synthesised, influenced the

Cette thèse est accessible à l'adresse : https://theses.insa-lyon.fr/publication/2022ISAL0081/these.pdf
© [B. Anantharamaiah], [2022], INSA Lyon, tous droits réservés

perception of their corresponding unpleasantness in listening tests. This was the prime effect that led to inconsistent grading of unpleasantness. However, the effect of sharpness and roughness of the audio files could not lead to any concrete influence on the unpleasantness grading. It is important that the audio files must be synthesised taking into consideration relevant loudness of the audio files from the tyre rolling cases (speed and pressure) from tests. This is a must to achieve a fair comparison of audio files between tests and synthesis. This study is recommended for future work.

Cette thèse est accessible à l'adresse : https://theses.insa-lyon.fr/publication/2022ISAL0081/these.pdf
© [B. Anantharamaiah], [2022], INSA Lyon, tous droits réservés

Recommendations for future work

The objective of the current work to study the possibility of using a numerical tool to model tyre rolling noise and implement it for pyschoacoustical studies has been achieved successfully. Now, the course of this study has opened up a plethora of prospects, especially in terms of noise modelling and psychoacoustics. These are now mentioned along with possible methodologies to realise them.

Inclusion of exterior environmental noise

Perception of any audio file in silent environment is different than in a noisy one. This is especially true for tyre noise. In this work, the rolling tyre noise was measured for several cases considered in a hemi-anechoic chamber at IDIADA center. Hence, the listener in the psychoacoustic test is abstained from traffic noise or at least real-world noise in which a car plies. The perception of tyre noise can be affected, e.g. due to masking effects that might occur when the tyre rolling noise is heard in synchrony with traffic noise.
This challenge can be addressed in two ways. One of the ways is to introduce white noise with the existing tyre rolling audio files and conduct the same listening tests to grade the unpleasantness. Another alternative is to record a live traffic noise in a standard location of a city at a predefined time of a day and combine it with the tyre rolling noise as background noise. This method will give a real understanding about the perception of unpleasantness of tyre rolling noise files.

Inclusion of possible pedestrian spatial information using transfer path analysis or acoustic source quantification and addition of Doppler effect

For all the tyre noise files generated in this work, the position of the microphone was in the vicinity of the leading edge of the rolling tyre. The same audio files were directly subjected to unpleasantness analysis. However, if the pedestrian safety is the main locus, then the spatial information of the pedestrian is important. This implementation is recommended from this work.
Using transfer path analysis (TPA) or acoustic source quantification (ASQ) method, the transfer function between the current microphone position in the test and a sample microphone that corresponds to a pedestrian position must be calculated. This must then be convolved with the current tyre rolling noise files. Then the resulting audio must be subjected to listening tests. Additionally, to generate a realistic scenario, the Doppler effect can be introduced during the audio playback. This is a feature that can be supplemented in MATLAB®.

Rubber material influence on tyre modal behaviour and quality of tyre rolling noise

During the calibration of hyperelasticity of constituent rubbers of the tyre considered, it was proved using DoE that the Eigen modes were sensitive to rubber hardness, especially that of sidewall and carcass hardness. This is an important domain to explore especially in terms of perception of tyre noise. As an example, tyre rolling noise for the various combinations of the hardness of the sidewall and the carcass region are generated; a comparison of PSDs are shown in Figure 5.18a. Their corresponding RMS levels are compared in Figure 5.18b. For the illustration, these tyre rolling audio files are only generated for a tyre with an inflation pressure of 2.4 bar that is rolling at 50 kph. However, the same study can be performed for various tyre rolling speeds and inflation pressures. In Figure 5.18, the tyre modelled with variable material consists of combination of sectors of 30° each modelled with various values of constituent rubber hardness. In this illustration, the sequence of these sector follows the order Carcass 1x, Carcass 2x, Optimised, Sidewall 1x and Sidewall 2x.

Cette thèse est accessible à l'adresse : https://theses.insa-lyon.fr/publication/2022ISAL0081/these.pdf
© [B. Anantharamaiah], [2022], INSA Lyon, tous droits réservés

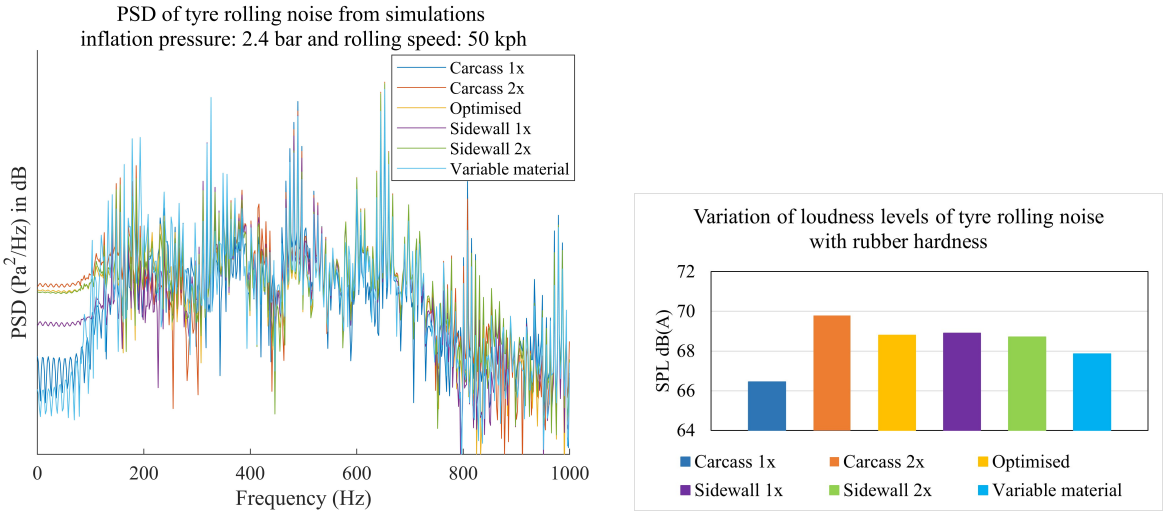

Figure 5.18: Contribution of the hardness values of the tyre constituent rubbers on to the tyre rolling noise. (a) PSDs of the tyre rolling noise for various combinations of the hardness values of the tyre rubber materials and (b) associated loudness levels of the audio files. Optimised tyre model bears a value of 1.5 times the hardness values (in shoreAs) for all the rubbers. Variable material model comprises of a combination of tyre sectors of 30° each modelled with various values of the hardness of constituent rubbers with the sequence - Carcass 1x, Carcass2x, Optimised, Sidewall 1x and Sidewall 2x.

From Figure 5.18a, it can be observed that the rolling noise of the tyre with variable material definition has higher dominance in the frequencies, approximately, 190 Hz, 350 Hz, 500 Hz, 650 Hz and 820 Hz. However, the Carcass 2x only influences 180 Hz, 500 Hz and 820 Hz. Similar observations can be made for other variants of rubbers hardness too. This is an indicator of the possible variations in perception of not only the unpleasantness of the rolling noise but also of its other attributes. Figure 5.18b is an evidence of such possibility since the loudness level of the rolling audio files is varying for the same speed and tyre inflation pressure. The corresponding variations in roughness and sharpness of the audio files is provided in Appendix B Figure B.10. Hence, material properties of a tyre, accompanied by environmental noise and Doppler effects as mentioned in this section, can be a definitive probe for the perception of tyre noise. However, in order to validate the results from such tests, the findings must be cross-verified with the rolling noise from a real tyre manufactured based on the suggested approach of material variations. Also, this study must also accompanied by checks on tyre rolling resistance, stiffness, wet and dry handling etc. to ensure that a tyre developed from variation of the hardness of selective rubber regions of the tyre still meets the necessary safety and operational standards.

Calculation of contact patch forces over irregular or real tarmac surfaces and tyre rolling noise generation

The tread pattern noise in a tyre is best captured when the tyre rolls over a smooth surface. In fact, the noise generated in this work also considers this condition. However, in order to excite the noise from the tyre sidewalls, it is necessary to make a tyre roll over an uneven surface. The corresponding forces acting on treads can be used for the convolution with respective tread IRs. Through this, the noise due to sidewall excitation can also be modelled.
Experimentally, it is very easy to generate such type of tyre noise. However, in order to capture the precise forces acting on the treads, several sensors that can be mounted on the inner torus of the tyre and which transfer the data using radio frequencies, are necessary. Alternatively, it

Cette thèse est accessible à l'adresse : https://theses.insa-lyon.fr/publication/2022ISAL0081/these.pdf
© [B. Anantharamaiah], [2022], INSA Lyon, tous droits réservés

is also possible to calculate these forces theoretically in COSIN Ftyre® software if the 3D topography of the road surface is available. These forces can then be employed in the simulations to generate tyre rolling noise due to various possible combinations of tread and sidewall excitations.

Study on the perception of other noise parameters

A tyre rolling noise has several attributes of which only unpleasantness was graded by the listeners in this work. Other attributes such as roughness, fluctuation strength, sharpness etc. could also provide an insight on the possibility of using a tyre noise for the detection of an approaching car. These attributes can be similarly graded as the unpleasantness was, in this work.

Monitoring the loudness levels during the synthesis of impact rolling noise from simulations

In the current work, it was also observed that the loudness levels of synthesised rolling noise files were not monitored, i.e. the level of tyre rolling noise measured in tests was not the same as that of the ones synthesised from simulations. This affected the grading of unpleasantness in audio files, especially with respect to variations in inflation pressure. It was also proved that the loudness of an audio file influences its other attributes that are related to perception. Hence, it is advised to monitor the loudness levels during the synthesis of the rolling noise from the concatenation and convolution of impact noises of the tyre. The levels of the synthesised audio files must be at par with that of the corresponding files measured in tests. This is an important task that is recommended to analyse and calibrate unpleasantness of tyre rolling noise, especially for the ones generated by synthesising impact noise at the tread contact patch, in future.

Cette thèse est accessible à l'adresse : https://theses.insa-lyon.fr/publication/2022ISAL0081/these.pdf
© [B. Anantharamaiah], [2022], INSA Lyon, tous droits réservés

Cette thèse est accessible à l'adresse : https://theses.insa-lyon.fr/publication/2022ISAL0081/these.pdf
© [B. Anantharamaiah], [2022], INSA Lyon, tous droits réservés

Cette thèse est accessible à l'adresse : https://theses.insa-lyon.fr/publication/2022ISAL0081/these.pdf
© [B. Anantharamaiah], [2022], INSA Lyon, tous droits réservés

Bibliography

[1] S. U. and E. J.A., *Tyre/road Noise Reference Book*. Informex, 2002.

[2] I. K. and Y. I., "A study on the mechanism of tire/road noise," *JSAE Review*, vol. 17, no. 2, pp. 139 – 144, 1996.

[3] J. G. Danijela M. and J. L., "Regulations on road vehicle noise – trends and future activities," *Project: Research of the safety of the vehicle as a part of cybernetic system "Driver-Vehicle-Environment"*, 2017.

[4] M. J.E. and E. B., *Science and Technology of Rubber (Third Edition)*. Academic Press, 2005.

[5] R. Jazar, *Vehicle Dynamics: Theory and Application*. SpringerLink : Bücher, Springer New York, 2013.

[6] M. Itskov, *Tensor Algebra and Tensor Analysis for Engineers: With Applications to Continuum Mechanics*. Mathematical Engineering, Springer International Publishing, 2015.

[7] H. Baaser, C. Hopmann, and A. Schobel, "Reformulation of strain invariants at incompressibility," *Archive of Applied Mechanics*, vol. 83, pp. 273–280, Feb 2013.

[8] J. Busfield and A. Muhr, *Constitutive Models for Rubber III: Proceedings of the Third European Conference on Constitutive Models for Rubber, London, UK, 15-17 September 2003*. Taylor & Francis, 2003.

[9] R. S. Rivlin and E. K. Rideal, "Large elastic deformations of isotropic materials iv. further developments of the general theory," *Philosophical Transactions of the Royal Society of London. Series A, Mathematical and Physical Sciences*, vol. 241, no. 835, pp. 379–397, 1948.

[10] M. Mooney, "A theory of large elastic deformation," *Journal of Applied Physics*, vol. 11, no. 9, pp. 582–592, 1940.

[11] O. H. Yeoh, "Some forms of the strain energy function for rubber," *Rubber Chemistry and Technology*, vol. 66, no. 5, pp. 754–771, 1993.

[12] . Abaqus documentation, "DSS Simulia, V 6.14."

[13] C. Tzikang, *Determining a Prony Series for a Viscoelastic Material From Time Varying Strain Data*. Original from NASA, 2000.

Cette thèse est accessible à l'adresse : https://theses.insa-lyon.fr/publication/2022ISAL0081/these.pdf
© [B. Anantharamaiah], [2022], INSA Lyon, tous droits réservés

[14] J. Ferry and J. Ferry, *Viscoelastic Properties of Polymers*. Wiley, 1980.

[15] V. Effinger, "Modelling of viscoelastic materials with ls-dyna.," 2012. 11th German LS-Dyna Forum, Ulm.
Available at: https://www.dynamore.de/de/download/papers/ls-dyna-forum-2012/documents/materials-4-1 [Accessed 3 Jul. 2018].

[16] Q. Xiding, L. Jude, and M. Yongxin, "A modified point contact tire model for the simulation of vehicle ride quality," *Journal of Terramechanics*, vol. 30, no. 3, pp. 133 – 141, 1993.

[17] IDIADA internal documentation.

[18] K. M. CAPTAIN, A. B. BOGHANI, and D. N. WORMLEY, "Analytical tire models for dynamic vehicle simulation," *Vehicle System Dynamics*, vol. 8, pp. 1–32, mar 1979.

[19] J. M. Badalamenti and G. R. Doyle, "Radial-interradial spring tire models," *Journal of Vibration Acoustics Stress and Reliability in Design*, vol. 110, no. 1, p. 70, 1988.

[20] T. Gillespie, *Fundamentals of Vehicle Dynamics*. Premiere Series Bks, Society of Automotive Engineers, 1992.

[21] H. B. Pacejka, "Chapter 9 - short wavelength intermediate frequency tire model," in *Tire and Vehicle Dynamics (Third Edition)* (H. B. Pacejka, ed.), pp. 403 – 474, Oxford: Butterworth-Heinemann, third edition ed., 2012.

[22] H. B. Pacejka, "Chapter 10 - dynamic tire response to short road unevennesses," in *Tire and Vehicle Dynamics (Third Edition)* (H. B. Pacejka, ed.), pp. 475 – 504, Oxford: Butterworth-Heinemann, third edition ed., 2012.

[23] S. T. H. Jansen, L. Verhoeff, R. Cremers, A. J. C. Schmeitz, and I. J. M. Besselink, "Mf-swift simulation study using benchmark data," *Vehicle System Dynamics*, vol. 43, no. sup1, pp. 92–101, 2005.

[24] C. Oertel and A. Fandre, "RMOD-k tyre model system," *ATZ worldwide*, vol. 103, pp. 23–25, nov 2001.

[25] H. B. Pacejka, "Chapter 13 - outlines of three advanced dynamic tire models," in *Tire and Vehicle Dynamics (Third Edition)* (H. B. Pacejka, ed.), pp. 577 – 591, Oxford: Butterworth-Heinemann, third edition ed., 2012.

[26] J. Reddy, *An Introduction to the Finite Element Method*. Asia Higher Education Engineering/Computer Science Mechanical Engineering, McGraw-Hill, 2006.

[27] H. Wang, I. L. Al-Qadi, and I. Stanciulescu, "Simulation of tyre-pavement interaction for predicting contact stresses at static and various rolling conditions," *International Journal of Pavement Engineering*, vol. 13, pp. 310–321, aug 2012.

[28] H. Li, *Analysis of Off-Road Tire-Soil Interaction through Analytical and Finite Element Methods*. PhD thesis, TU Kaiserslautern, 10 2013.

[29] M. Sabri, "Displacement of a free tyre in natural frequencies to determine noise structure," *IOP Conference Series: Materials Science and Engineering*, vol. 180, p. 012023, mar 2017.

[30] C. Suvanjumrat and R. Rugsaj, "Finite element modeling with embed rebar elements and steady state rolling analysis for rolling resistance test of pneumatic tire," in *Proc. of MATEC Web Conf.*, 2017.

Cette thèse est accessible à l'adresse : https://theses.insa-lyon.fr/publication/2022ISAL0081/these.pdf
© [B. Anantharamaiah], [2022], INSA Lyon, tous droits réservés

[31] F. Gauterin and C. Ropers, "Modal tyre models for road noise improvement," *Vehicle System Dynamics*, vol. 43, pp. 297–304, jan 2005.

[32] F. Yazdandoost and S. Taheri, "Finite element tyre model for antilock braking system study," *International Journal of Vehicle Design*, vol. 72, no. 3, p. 248, 2016.

[33] X. Yang, M. Behroozi, and O. A. Olatunbosun, "A neural network approach to predicting car tyre micro-scale and macro-scale behaviour," *Journal of Intelligent Learning Systems and Applications*, vol. 06, no. 01, pp. 11–20, 2014.

[34] N. Korunovic, M. Trajanovic, M. Stojkovic, N. Vitkovic, M. Trifunovic, and J. Milovanovic, "Detailed vs. simplified tread tire model for steady-state rolling analysis," *Strojarstvo: Journal for Theory and Application in Mechanical Engineering*, vol. 54, pp. 153–160, 04 2012.

[35] M. Heckl, "Tyre noise generation," *Wear*, vol. 113, no. 1, pp. 157 – 170, 1986.

[36] P. Kindt, *Structure-Borne Tyre/Road Noise due to Road Surface Discontinuities*. PhD thesis, KU Leuven, 06 2009.

[37] W. F. Reiter and F. D. Hart, "Experimental investigation of the vibrational characteristics of truck tires," *The Journal of the Acoustical Society of America*, vol. 51, no. 1A, pp. 88–88, 1972.

[38] A. Kuijpers and G. van Blokland, "Tyre/road noise models in the last two decades: A critical evaluation," *INTER-NOISE and NOISE-CON Congress and Conference Proceedings*, vol. 2001, no. 2, pp. 2494–2499, 2001.

[39] W. A. Leasure and E. K. Bender, "Tire–road interaction noise," *The Journal of the Acoustical Society of America*, vol. 58, no. 1, pp. 39–50, 1975.

[40] M. Brinkmeier, U. Nackenhorst, S. Petersen, and O. Estorff, "A finite element approach for the simulation of tire rolling noise," *Journal of Sound and Vibration*, vol. 309, pp. 20–39, 01 2008.

[41] M. Brinkmeier, U. Nackenhorst, J. Biermann, and O. Estorff, "Simulation and analysis of tire road noise, finite element results and validation," *The Journal of the Acoustical Society of America*, vol. 123, p. 3673, 06 2008.

[42] T. Lafont, R. Stelzer, R. D'amico, C. Bertolini, and W. Kropp, "Modeling tyre noise in FE simulations for pass-by noise predictions," in *NOVEM conference*, 05 2018.

[43] C. Nilsson, *Waveguide Finite Elements Applied on a Car Tyre*. PhD thesis, Royal Institute of Technology, Stockholm, 2004.

[44] J. Biermann, O. Estorff, S. Petersen, and H. Schmidt, "Computational model to investigate the sound radiation from rolling tires," *Tire Science and Technology*, vol. 35, 09 2007.

[45] W. Kropp, P. Sabiniarz, H. Brick, and T. Beckenbauer, "Sound radiation of a rolling tyre," *Journal of Sound and Vibration*, vol. 331, p. 1789–1805, 04 2012.

[46] C. Hoever, A. Tsotras, E.-U. Saemann, and W. Kropp, "A comparison between finite element and waveguide finite element methods for the simulation of tire/road interaction," *INTERNOISE and NOISE-CON Congress and Conference Proceedings*, 01 2013.

[47] C. Hoever and W. Kropp, "The simulation of truck tire rolling noise," in *INTERNOISE*, 08 2015.

Cette thèse est accessible à l'adresse : https://theses.insa-lyon.fr/publication/2022ISAL0081/these.pdf
© [B. Anantharamaiah], [2022], INSA Lyon, tous droits réservés

[48] P. Jean, N. Noe, and F. Gaudaire, "Calculation of tyre noise radiation with a mixed approach," *Acta Acustica united with Acustica*, vol. 94, pp. 91–103, 01 2008.

[49] Z. Zhang, N. Vlahopoulos, T. Allen, and K. Zhang, "Development and validation of a computational process for pass-by noise simulation," *International Journal of Vehicle Design - INT J VEH DES*, vol. 34, 01 2004.

[50] W. Yintao, X. Feng, D. Xiang, and Y. Gchen, "A simulation methodology for tire/road vibration noise analysis," in *INTERNOISE 2014 - 43rd International Congress on Noise Control Engineering: Improving the World Through Noise Control*, 11 2014.

[51] M. Clerc, A. Dervieux, R. Keriven, O. Faugeras, J. Kybic, and T. Papadopoulo, "Comparison of BEM and FEM methods for the e/meg problem," *Jr. of Image and Vision Computing*, 12 2002.

[52] S. Marburg and B. Nolte, *Computational Acoustics of Noise Propagation in Fluids - Finite and Boundary Element Methods*. Springer Verlag, 01 2008.

[53] Y. Liu and N. Nishimura, "The fast multipole boundary element method for potential problems: A tutorial," *Engineering Analysis with Boundary Elements*, vol. 30, pp. 371–381, 05 2006.

[54] H. Peters and D. Wilkes, "A comparison of numerical methods for the large-scale modelling of acoustic coupled fluid-structure interactions of double-walled cylindrical shells," in *INTERNOISE 2014 - 43rd International Congress on Noise Control Engineering: Improving the World Through Noise Control*, 11 2014.

[55] S. Marburg, "Six boundary elements per wavelength: Is that enough?," *Journal of Computational Acoustics*, vol. 10, pp. 25–51, 03 2002.

[56] C. Li and J. Lian, "Development and application of a pre-corrected fast fourier transform accelerated multi-layer boundary element method for the simulation of shallow water acoustic propagation," *Applied Sciences*, vol. 10, p. 2393, 04 2020.

[57] M. Ram and O. Estorff, "Fast algorithms applied to the acoustical energy boundary element method," in *International Congress on Acoustics, Aachen*, 09 2019.

[58] D. Panagiotopoulos, E. Deckers, and W. Desmet, "Krylov subspaces recycling based model order reduction for acoustic bem systems and an error estimator," *Computer Methods in Applied Mechanics and Engineering*, vol. 359, p. 112755, 2020.

[59] Y. Tang, A. Zhou, and K.-C. Hui, "Comparison between fem and bem for real-time simulation," *Computer-Aided Design and Applications*, vol. 2, pp. 421–430, 08 2005.

[60] T. Beckenbauer, P. Klein, J.-F. Hamet, and W. Kropp, "Tyre?road noise prediction: A comparison between the speron and hyrone models - part 1," *The Journal of the Acoustical Society of America*, vol. 123, p. 3388, 06 2008.

[61] P. Klein, T. Beckenbauer, J.-F. Hamet, and W. Kropp, "Tyre/road noise prediction: A comparison between the speron and hyrone models - part 2," *The Journal of the Acoustical Society of America*, vol. 123, p. 3389, 06 2008.

[62] P. Morse and K. Ingard, *Theoretical Acoustics*. International series in pure and applied physics, Princeton University Press, 1986.

[63] S. Marburg, *A Unified Approach to Finite and Boundary Element Discretization in Linear Time–Harmonic Acoustics*. Springer Verlag, 01 2008.

Cette thèse est accessible à l'adresse : https://theses.insa-lyon.fr/publication/2022ISAL0081/these.pdf
© [B. Anantharamaiah], [2022], INSA Lyon, tous droits réservés

[64] A. Bayliss and E. Turkel, "Radiation boundary conditions for wave-like equations," *Communications on Pure and Applied Mathematics*, vol. 33, no. 6, pp. 707–725, 1980.

[65] M. Israeli and S. A. Orszag, "Approximation of radiation boundary conditions," *Journal of Computational Physics*, vol. 41, no. 1, pp. 115–135, 1981.

[66] J.-P. Berenger, "A perfectly matched layer for the absorption of electromagnetic waves," *Journal of Computational Physics*, vol. 114, no. 2, pp. 185–200, 1994.

[67] J.-P. Berenger, "Perfectly matched layer for the fdtd solution of wave-structure interaction problems," *IEEE Transactions on Antennas and Propagation*, vol. 44, no. 1, pp. 110–117, 1996.

[68] L. Zhao and A. Cangellaris, "A general approach for the development of unsplit-field time-domain implementations of perfectly matched layers for fdtd grid truncation," *IEEE Microwave and Guided Wave Letters*, vol. 6, no. 5, pp. 209–211, 1996.

[69] R. J. Astley, *Infinite Elements*, pp. 197–230. Springer Berlin Heidelberg, 2008.

[70] B. Moore, *An Introduction to the Psychology of Hearing: Sixth Edition*. Leiden, The Netherlands: Brill, 2013.

[71] E. Freitas, F. Soares, and J. Lamas, "Exploring psychoacoustic indicators to assess close proximity tyre-road noise," in *EuroRegio 2016, Porto*, 2016.

[72] E. Freitas, J. Lamas, C. Silva, F. Soares, SandraMouta, and J. A. Santos, "Tyre/road noise annoyance assessment through virtual sounds," in *Jr. of Environmental Science*, 2016.

[73] R. Barti, "Psychoacoustics applied to tire noise," in *Forum Acusticum, Sevilla 2002: Technical Programme*, 2002.

[74] A. Hoffmann and W. Kropp, "Auralization of simulated tyre noise: Psychoacoustic validation of a combined model," *Applied Acoustics*, vol. 145, pp. 220–227, 02 2019.

[75] A. Hoffmann, P. Bergman, and W. Kropp, "Perception of tyre noise: Can tyre noise be differentiated and characterized by the perception of a listener outside the car?," *Acta Acustica united with Acustica*, vol. 102, pp. 992–998, 10 2016.

[76] J. Forssén, A. Hoffmann, and W. Kropp, "Auralization model for the perceptual evaluation of tyre–road noise," *Applied Acoustics*, vol. 132, pp. 232–240, 03 2018.

[77] H. Fastl and E. Zwicker, *Psychoacoustics*. Springer Berlin Heidelberg, 2007.

[78] BSI, "Iso 226:2003 acoustics—normal equal-loudness-level contours," standard, British Standards, 2003.

[79] E. Zwicker and H. Fastl, *Critical Bands and Excitation*, pp. 149–173. Berlin, Heidelberg: Springer Berlin Heidelberg, 2007.

[80] B. Berglund, U. Berglund, M. Goldstein, and T. Lindvall, "Loudness (or annoyance) summation of combined community noises," *The Journal of the Acoustical Society of America*, vol. 70, no. 6, pp. 1628–1634, 1981.

[81] A. Hoffmann, *Auralization,perception and detection of tyre-road noise*. PhD thesis, Chalmers University of Technology, Gothenburg, Sweden, 2004.

[82] A. P. and W. B., *Analyzing hyperelastic material with some practical considerations*. Academic Press, third edition ed., 2005.

Cette thèse est accessible à l'adresse : https://theses.insa-lyon.fr/publication/2022ISAL0081/these.pdf
© [B. Anantharamaiah], [2022], INSA Lyon, tous droits réservés

[83] *Introduction to iSight*, Section: I-Beam DoE, Dassault Systemes, 2017.

[84] B. Peeters, H. Van der Auweraer, P. Guillaume, and J. Leuridan, "The polymax frequency-domain method: A new standard for modal parameter estimation?," *Shock and Vibration*, vol. 11, pp. 395–409, 01 2004.

[85] J. Salencon, *Viscoelastic Modeling for Structural Analysis*. Wiley, 05 2019.

[86] S. Arrieta, J. Diani, and P. Gilormini, "Experimental characterization and thermoviscoelastic modeling of strain and stress recoveries of an amorphous polymer network," *Mechanics of Materials*, vol. 68, pp. 95 – 103, 2014.

[87] X. Wang, K. ZHAO, and H. ZHAO, "Finite element simulation of biofilm viscoelastic behavior under various loadings," *Journal of Mechanics in Medicine and Biology*, vol. 18, p. 1850056, 08 2018.

[88] C. Ganser, C. Czibula, D. Tscharnuter, T. Schöberl, C. Teichert, and U. Hirn, "Combining adhesive contact mechanics with a viscoelastic material model to probe local material properties by afm," *Soft matter*, vol. 14, p. 140—150, December 2017.

[89] J. Moacanin, J. J. Aklonis, and R. F. Landel, "A generalization of the boltzmann superposition principle to polymer networks undergoing scission," *The Journal of Chemical Physics*, vol. 64, no. 1, pp. 430–430, 1976.

[90] R. Christensen, "Chapter i - viscoelastic stress strain constitutive relations," in *Theory of Viscoelasticity (Second Edition)* (R. Christensen, ed.), pp. 1 – 34, Academic Press, second edition ed., 1982.

[91] K. Menard, *Dynamic Mechanical Analysis: A Practical Introduction, Second Edition*. CRC Press, 2008.

[92] M. Machado, U. D. Cakmak, I. Kallai, and Z. Major, "Thermomechanical viscoelastic analysis of woven-reinforced thermoplastic-matrix composites," *Composite Structures*, vol. 157, pp. 256–264, 2016.

[93] M. A. Tapia Romero, M. Gomez, and L. Lugo, "Prony series calculation for viscoelastic behavior modeling of structural adhesives from DMA data," *Ingeniería Investigación y Tecnología*, vol. 21, pp. 1–10, 04 2020.

[94] I. Lopez Arteaga, *Influence of material damping on the prediction of road texture and tread pattern related rolling resistance*. ISMA 2010 International Conference on Noise and Vibration Engineering, Katholieke Universiteit Leuven, September 2010.

[95] F. Orban, "Damping of materials and members in structures," *Journal of Physics: Conference Series*, vol. 268, p. 012022, jan 2011.

[96] A. Alipour and F. Zareian, "Study rayleigh damping in structures; uncertainties and treatments," in *The 14^{th} World Conference on Earthquake Engineering, Beijing*, December 2008.

[97] J. S. Bolton and K. Yum, "Sound radiation modes of a tire on a reflecting surface," *The Journal of the Acoustical Society of America*, vol. 123, no. 5, pp. 3672–3672, 2008.

[98] T. Denton, *Automotive Technician Training: Theory*. CRC Press, 2014.

[99] C. Goeury, T. David, R. Ata, Y. Audouin, N. Goutal, A.-L. Popelin, M. Couplet, M. Baudin, and R. Barate, "Uncertainty quantification on a real case with telemac-2d," in *Conf. of XXII Telemac User club, Daresbury*, 10 2015.

Cette thèse est accessible à l'adresse : https://theses.insa-lyon.fr/publication/2022ISAL0081/these.pdf
© [B. Anantharamaiah], [2022], INSA Lyon, tous droits réservés

[100] H. Garcia-Alfonso and D.-M. Córdova-Esparza, "Comparison of uncertainty analysis of the montecarlo and latin hypercube algorithms in a camera calibration model," in *2018 IEEE 2nd Colombian Conference on Robotics and Automation (CCRA)*, pp. 1–5, 2018.

[101] K. Kaewsuwan, C. Yuangyai, U. Janjarassuk, and K. Rienkhemaniyom, "A comparison of latin hypercube sampling techniques for a supply chain network design problem," *MATEC Web of Conferences*, vol. 192, p. 1023, 01 2018.

[102] M. Mckay, R. Beckman, and W. Conover, "A comparison of three methods for selecting vales of input variables in the analysis of output from a computer code," *Technometrics*, vol. 21, pp. 239–245, 05 1979.

[103] T. Hochkirchen, "Design and modeling for computer experiments by k.-t. fang, r. li and a. sudjianto," *Journal of the Royal Statistical Society Series A*, vol. 169, pp. 1007–1008, 02 2006.

[104] M. D. Shields and J. Zhang, "The generalization of latin hypercube sampling," *Reliability Engineering and System Safety*, vol. 148, pp. 96–108, 2016.

[105] K. Kaewsuwan, C. Yuangyai, U. Janjarassuk, and K. Rienkhemaniyom, "A comparison of latin hypercube sampling techniques for a supply chain network design problem," *MATEC Web of Conferences*, vol. 192, p. 01023, 01 2018.

[106] D. Bies, C. Hansen, and C. Howard, *Engineering Noise Control, Fifth Edition*. CRC Press, 11 2017.

Cette thèse est accessible à l'adresse : https://theses.insa-lyon.fr/publication/2022ISAL0081/these.pdf
© [B. Anantharamaiah], [2022], INSA Lyon, tous droits réservés

Cette thèse est accessible à l'adresse : https://theses.insa-lyon.fr/publication/2022ISAL0081/these.pdf
© [B. Anantharamaiah], [2022], INSA Lyon, tous droits réservés

Appendix A

A.1 Mode shapes

In this section mode shapes of the tyre are shown. These are identified from testing and simulation. The simulation model is setup using optimised rubber shoreA values as determined in section 3.

Figure A.1: Mode shape for Eigen mode 1 (66 Hz) – (left) from simulation and (right) from test.

Figure A.2: Mode shape for Eigen mode 2 (100 Hz) – (left) from simulation and (right) from test.

Cette thèse est accessible à l'adresse : https://theses.insa-lyon.fr/publication/2022ISAL0081/these.pdf
© [B. Anantharamaiah], [2022], INSA Lyon, tous droits réservés

Figure A.3: Mode shape for Eigen mode 3 (118 Hz) – (left) from simulation and (right) from test.

Figure A.4: Mode shape for Eigen mode 4 (146 Hz) – (left) from simulation and (right) from test.

Figure A.5: Mode shape for Eigen mode 5 (171 Hz) – (left) from simulation and (right) from test.

Cette thèse est accessible à l'adresse : https://theses.insa-lyon.fr/publication/2022ISAL0081/these.pdf
© [B. Anantharamaiah], [2022], INSA Lyon, tous droits réservés

A.2 Criteria for a good match in PI in test and simulation

During the tests for PIs of a free-free tyre in the vibroacoustic chamber, an interesting phenomena of shifting in amplitudes and frequencies were observed. A random example of three different PIs measured at various time instances of the test, for the impact point 16 (Refer Figure 3.7 for the location), is shown in Figure A.6 as an evidence. The instances here refer to the time points when the PIs were measured, for the same impact location, with an interval of 8 hours at least.

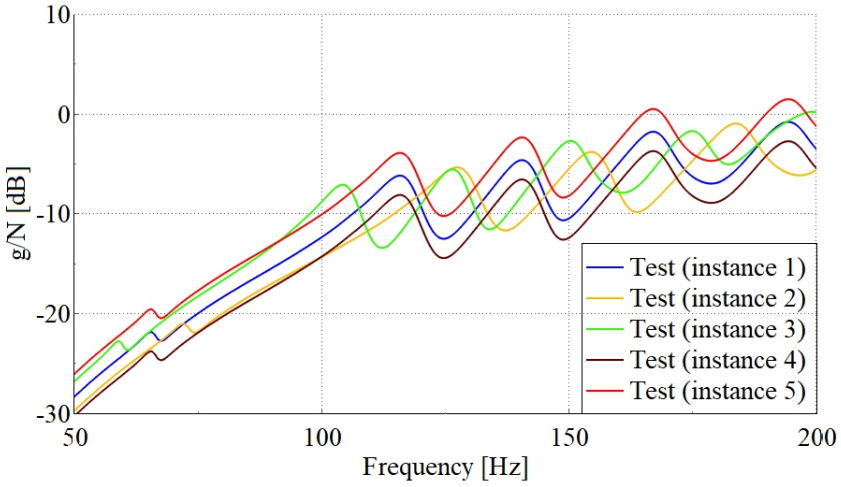

Figure A.6: Discrepancy in the PI behaviour of the free-free tyre for various instances. Instances here refer to several time points when the PIs of an impact location were measured. Instance 1 is considered for the current work since it appeared to be a median of the observed PIs.

From Figure A.6 it can be observed that the PI behaviour varied for various instances. On an average, there exists at least 3-5 dB of amplitude variations and a frequency variation of 20 Hz among the instances. As a reference to compare with the simulation, instance 1 was considered since it "appeared" to be the median of the observed PIs. It is to be noted that, for each instance, the room temperature and tyre internal pressure were measured and made sure that there exits no extreme differences in them. The cause for this discrepancy is still a mystery.

Cette thèse est accessible à l'adresse : https://theses.insa-lyon.fr/publication/2022ISAL0081/these.pdf
© [B. Anantharamaiah], [2022], INSA Lyon, tous droits réservés

A.3 Transfer inertances

The sample points considered for transfer inertance comparison between test and simulation is shown in Figure A.7. The impact is delivered on point 1 - N16 and transfer inertances for points 2 - 6 are compared. The location of these points along the tyre width is also shown in the section A-A and section B-B views in the same figure.

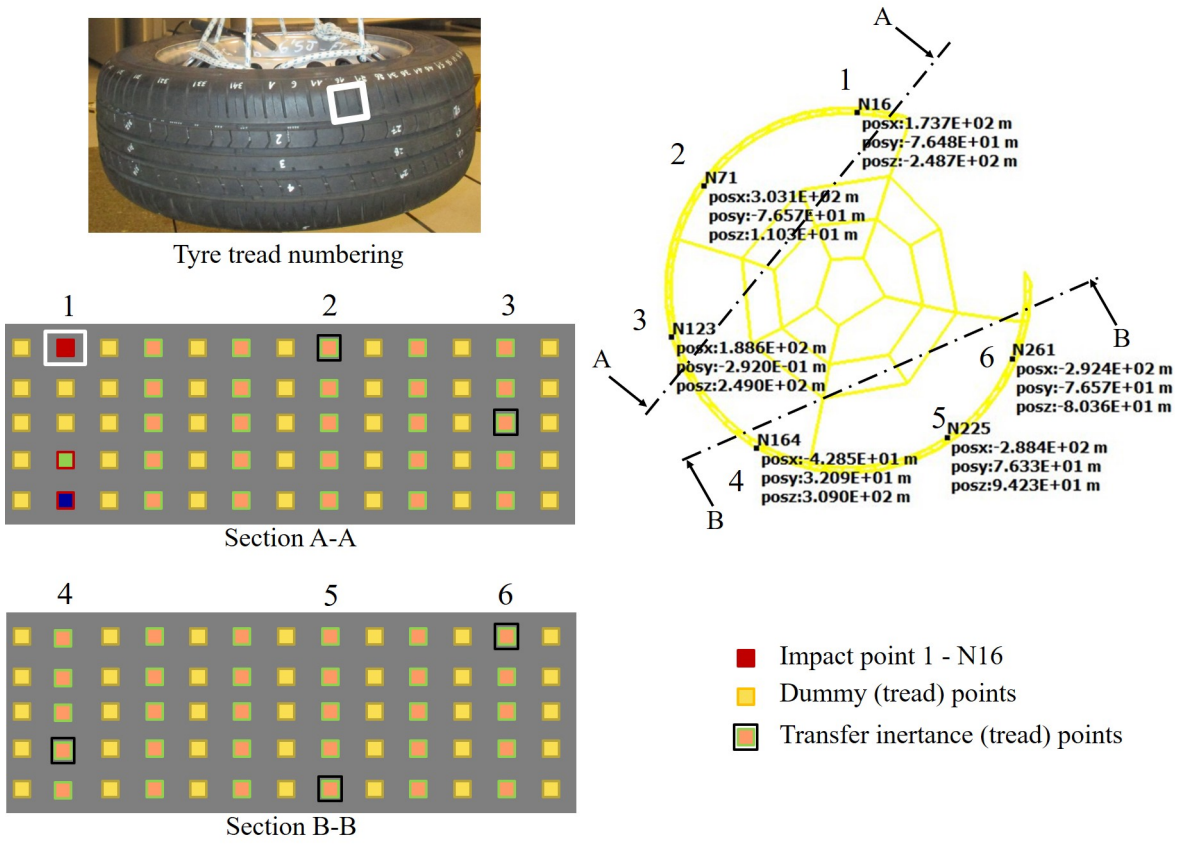

Figure A.7: Tyre points considered for transfer inertance comparison. Sections A-A and B-B showing the location of transfer intertance measurement points on the tyre.

The transfer inertances of the considered points is shown in Figure A.8. From these figures, it can be observed that although the twisting mode at 100 Hz (refer Figure A.2 for the mode shape) exists in the simulation, there are some discrepancies in its measurements in the test. In Figures A.8b-A.8d, the amplitude of this mode is underestimated in the test. Where as the same mode in Figures A.8a and A.8e is not detected in the test. Undoubtedly, this is credited to the incapability of the accelerometers to measure the axial displacement of the tyre when they are oriented in radial direction.

Cette thèse est accessible à l'adresse : https://theses.insa-lyon.fr/publication/2022ISAL0081/these.pdf
© [B. Anantharamaiah], [2022], INSA Lyon, tous droits réservés

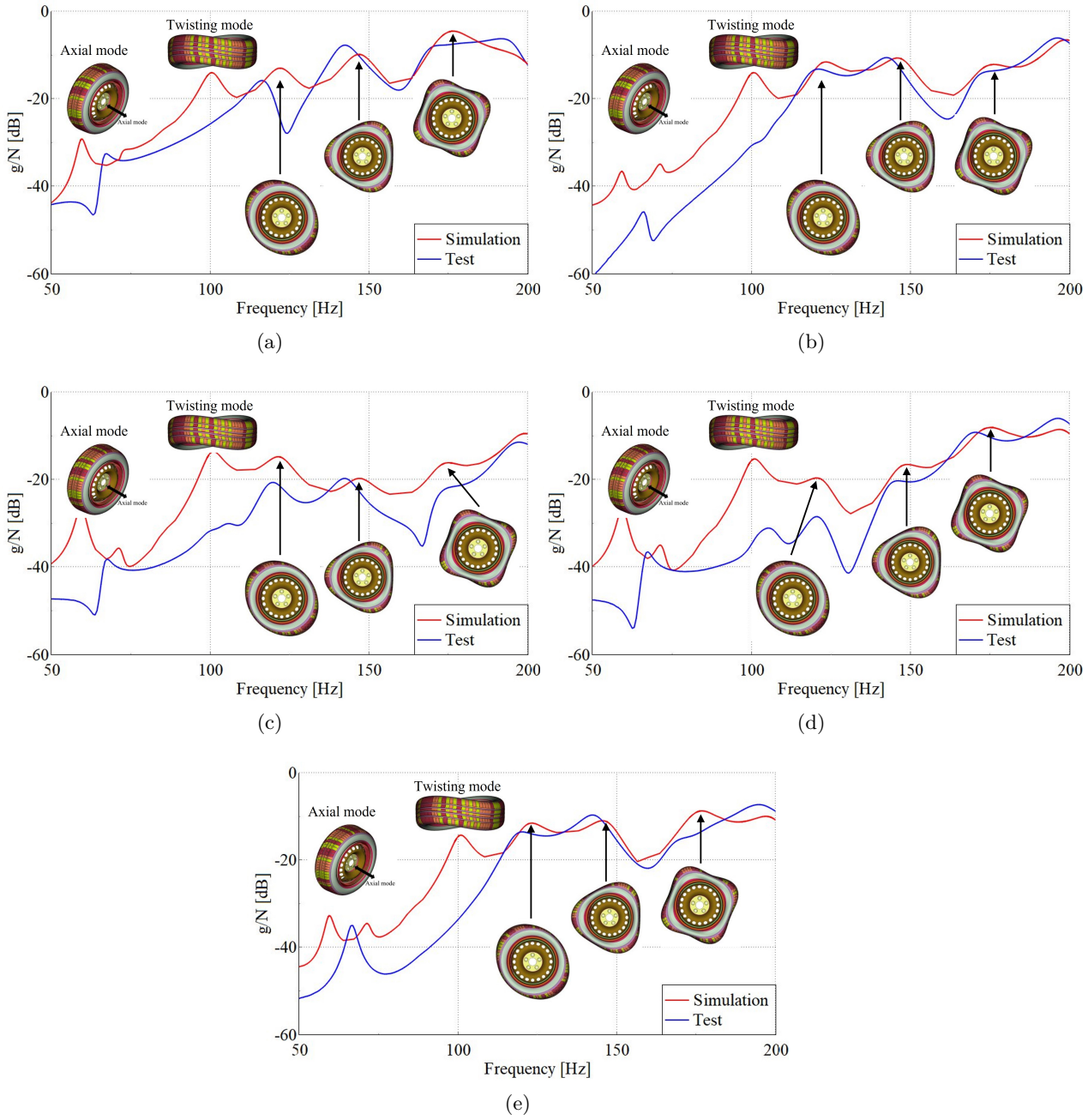

Figure A.8: Transfer inertance plots of radial response of the tyre for points 2-6 (refer Figure A.7 for these points) for an impact on point 1 on the tyre. For points information refer Figure A.7. Note: The capacity of measuring the radial responses of the tyre for axial modes by a monoaxial accelerometer in test is low. Hence, measuring the displacements only in the radial direction (of accelerometer) in the test is a limitation.

Cette thèse est accessible à l'adresse : https://theses.insa-lyon.fr/publication/2022ISAL0081/these.pdf
© [B. Anantharamaiah], [2022], INSA Lyon, tous droits réservés

A.4 Design of experiments

Design of experiments or DoE is a statistical analysis technique that enables to study the degree of variations in the output of a multi-variable/multi-dimensional system due to variations in the values of the input variables. This is particularly of importance in multidimensional systems, where the variables combinely contribute to the output of the system.
DoE involves generation of several simulation input files (with respect to the domain of current thesis), also known as *sampling*, with different input variable values. Once these simulations are computed, the dependency between the inputs and the outputs as well as the co-dependency between the outputs can be studied. Most important step in DoE is the choice of sample generation method and the selection of factors/variables to be sampled. With respect to the choice of sample generation method, there are several methods available in literature, such as polynomial method, Monte-Carlo sampling technique, Latin Hypercube technique (LHS) etc. Out of these LHS is chosen in this work due to recommendations from previous case studies [99, 100, 101]. These recommendations are in line with the computational efforts, accuracy in the result predictions and sample size necessities.

Latin Hypercube sampling technique

Latin Hypercube sampling was introduced by McKay et .al in 1979 [102]. In LHS technique a random input vector $\mathbf{x}$ of dimension $\mathbf{k}$ and input points (or sample space) defined by

$$\mathbf{x} = [\mathbf{x}_1, \mathbf{x}_2, \mathbf{x}_3, ..., \mathbf{x}_k]^T \tag{A.1}$$

are considered. This sample space is divided into n strata (S_{kn}) of equal marginal probability ($p_{kn} = 1/N$) so that only "one value per each strata/interval" is randomly chosen [102]. Thus, LHS partitions each input distribution into N intervals of equal probability. It shuffles the sample for each input so that there is no correlation between the inputs and no two input points are chosen from a common sample space [103]. A 4 $\times$4 sampling space with the LHS sampling points is depicted in Figure A.9.

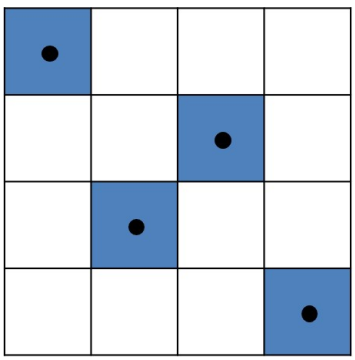

Figure A.9: Sampling pattern in LHS technique. According to [102].

Perhaps the only limitation with the usage of LHS technique is its incapability in variance reduction on variable/input parameter interactions [104]. This however has been addressed by updating the sampling algorithm using Improved Distributed Hypercube Sampling (IHS) [105]. Nevertheless, the sampling interface used does not offer the possibility of using IHS for sample generation and considering the non-complexity of the problem, LHS is opted in this work.

Cette thèse est accessible à l'adresse : https://theses.insa-lyon.fr/publication/2022ISAL0081/these.pdf
© [B. Anantharamaiah], [2022], INSA Lyon, tous droits réservés

A.5 Pareto plots

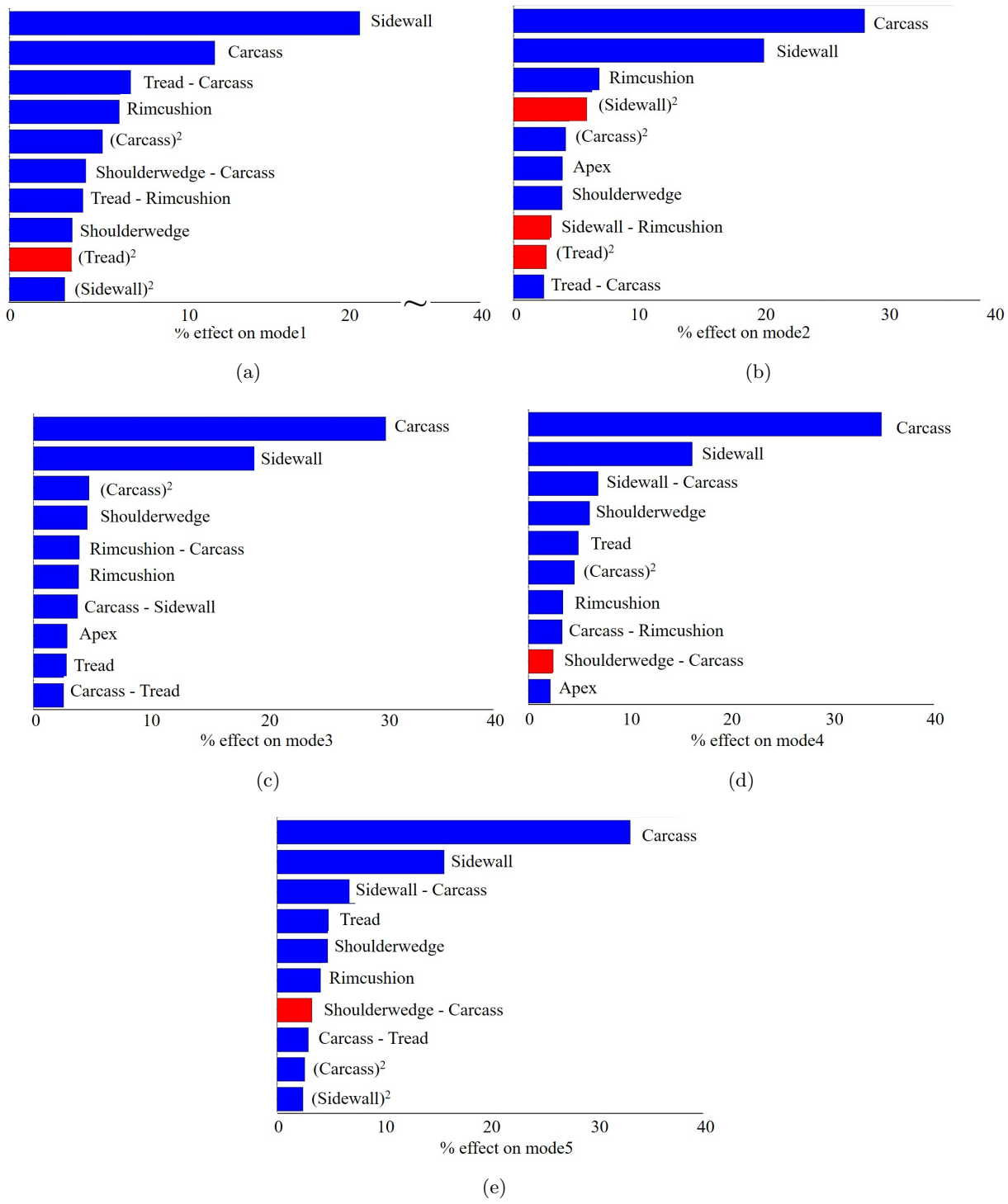

Figure A.10: Pareto plots for the first five modes of the tyre as obtained from the DoE tool. Red indicates the inverse effect of the variable over the system output.

Cette thèse est accessible à l'adresse : https://theses.insa-lyon.fr/publication/2022ISAL0081/these.pdf
© [B. Anantharamaiah], [2022], INSA Lyon, tous droits réservés

A.6 Modal damping factors

Table A.1: Modal damping values as obtained from tests.

Eigen freq. (Hz)	Damping value (%)
66.51	2.53
100.87	3.24
118.25	4.18
142.68	3.80
168.73	3.50
195.61	3.11

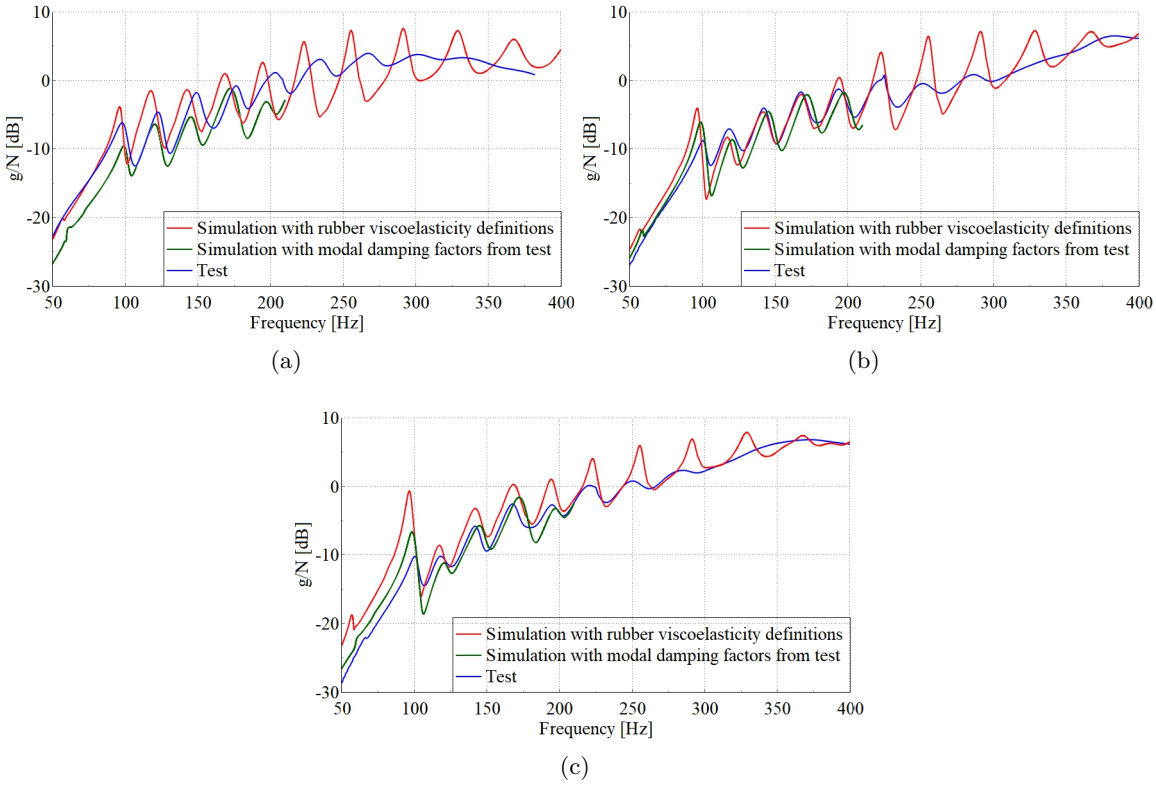

Figure A.11: Comparison of point inertances between test and simulation with the Prony viscoelasticity definition and modal damping factors that are determined from tyre modal tests - (a) for point 16, (b) for point 19 and (c) for point 20. Refer Figure 3.7 for the location of the points. The simulation model with modal damping factors is only up to 200 Hz since the determination of these damping factors from test is difficult due to high modal density beyond this frequency limit.

Cette thèse est accessible à l'adresse : https://theses.insa-lyon.fr/publication/2022ISAL0081/these.pdf
© [B. Anantharamaiah], [2022], INSA Lyon, tous droits réservés

Appendix B

B.1 Convolution theorem

Convolution of two functions is an operation that is equivalent to overlapping or multiplication of two *continuous* functions. Consider $x(t)$ and $h(t)$ that are in time domain. The corresponding mathematical formulation for the convolution of the functions considered is given by [106]

$$y(t) = x(t) \times h(t) = \int_{-\infty}^{\infty} x(\tau)h(t-\tau)d\tau. \tag{B.1}$$

However, the same operation in frequency domain is mere multiplication of the terms [106], i.e.

$$Y(f) = X(f) \times H(f). \tag{B.2}$$

Cette thèse est accessible à l'adresse : https://theses.insa-lyon.fr/publication/2022ISAL0081/these.pdf
© [B. Anantharamaiah], [2022], INSA Lyon, tous droits réservés

B.2 Loaded tyre NTFs, IRs, contact patch forces and PSDs

NTFs and IRs of medium tread pitch blocks due to impacts at contact patches.

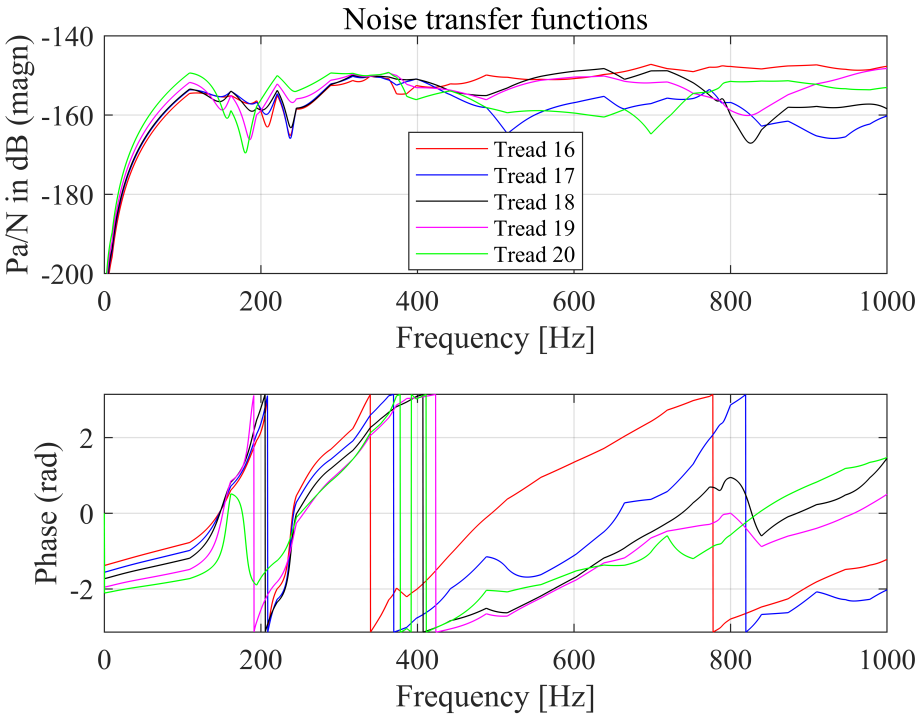

(a)

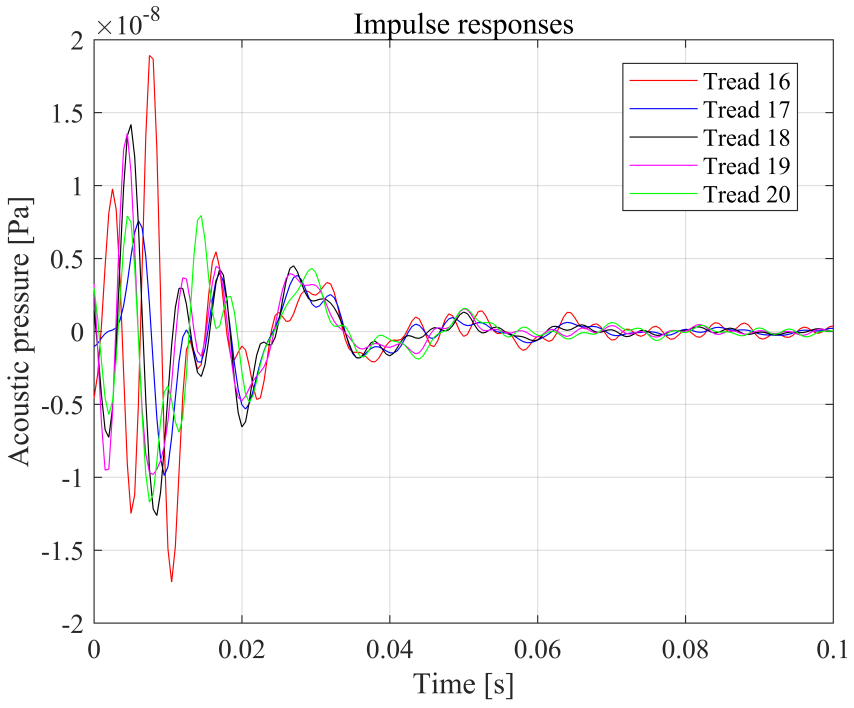

(b)

Figure B.1: Tyre tread noise behaviour study for a tyre inflated at 2.1 bar. (a) The NTF plot of tread block impacts considered and (b) IRs generated from IFFT of NTFs of the treads considered. Sampling frequency - 2 kHz. Refer Figure 5.1b for the tread blocks considered.

Cette thèse est accessible à l'adresse : https://theses.insa-lyon.fr/publication/2022ISAL0081/these.pdf
© [B. Anantharamaiah], [2022], INSA Lyon, tous droits réservés

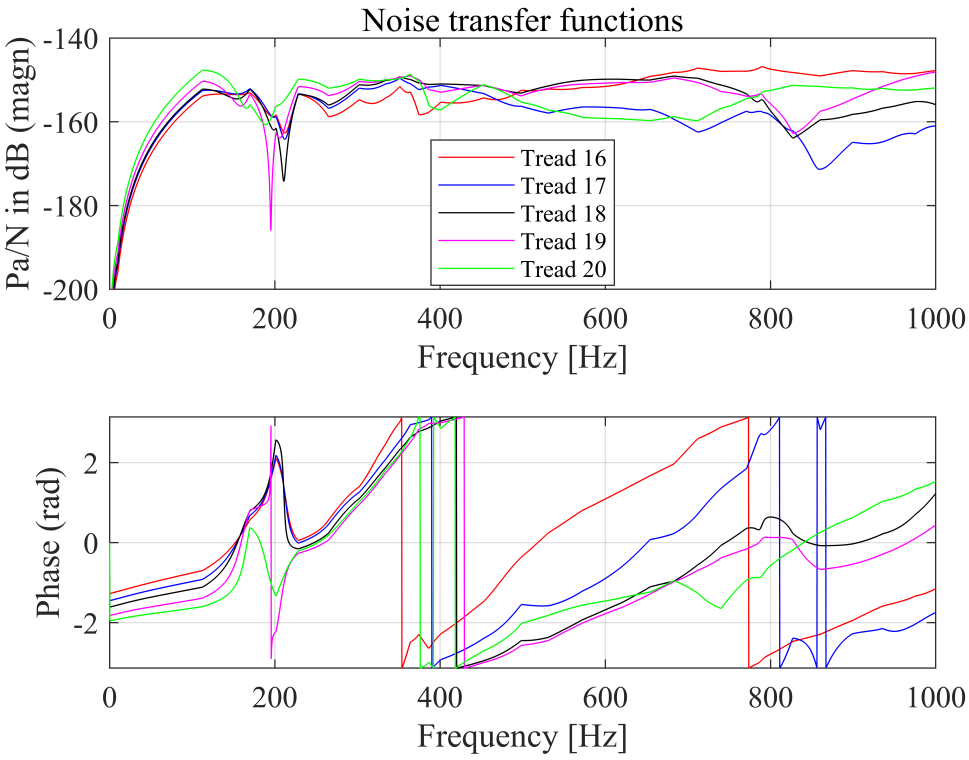

(a)

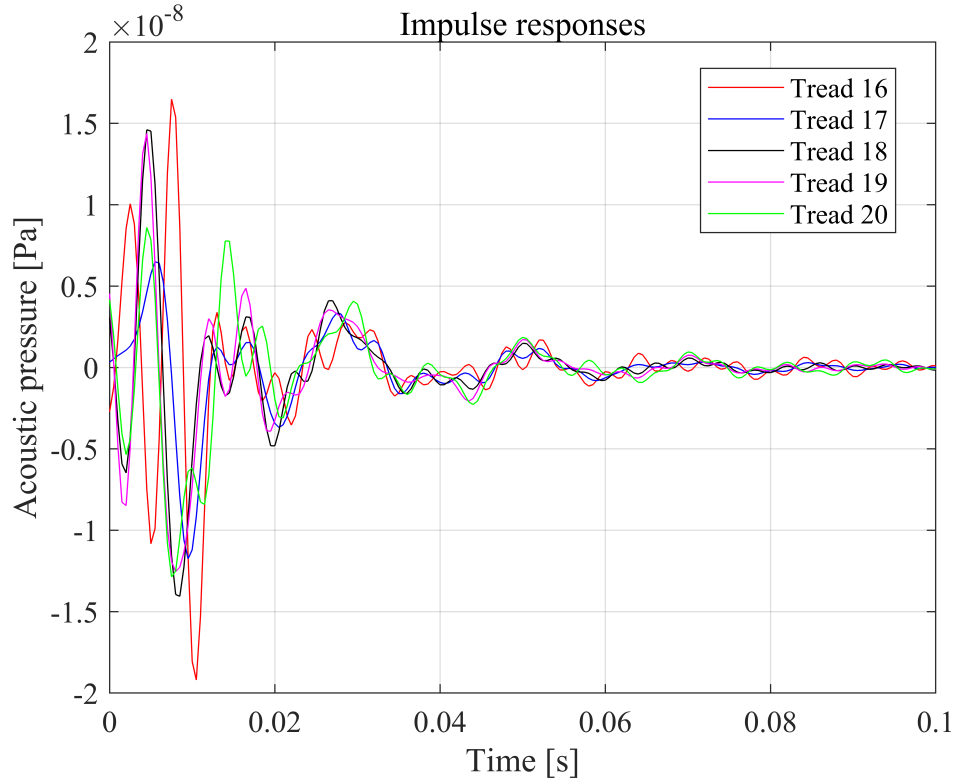

(b)

Figure B.2: Tyre tread noise behaviour study for a tyre inflated at 2.7 bar. (a) The NTF plot of tread block impacts considered and (b) IRs generated from IFFT of NTFs of the treads considered. Sampling frequency - 2 kHz. Refer Figure 5.1b for the tread blocks considered.

Cette thèse est accessible à l'adresse : https://theses.insa-lyon.fr/publication/2022ISAL0081/these.pdf
© [B. Anantharamaiah], [2022], INSA Lyon, tous droits réservés

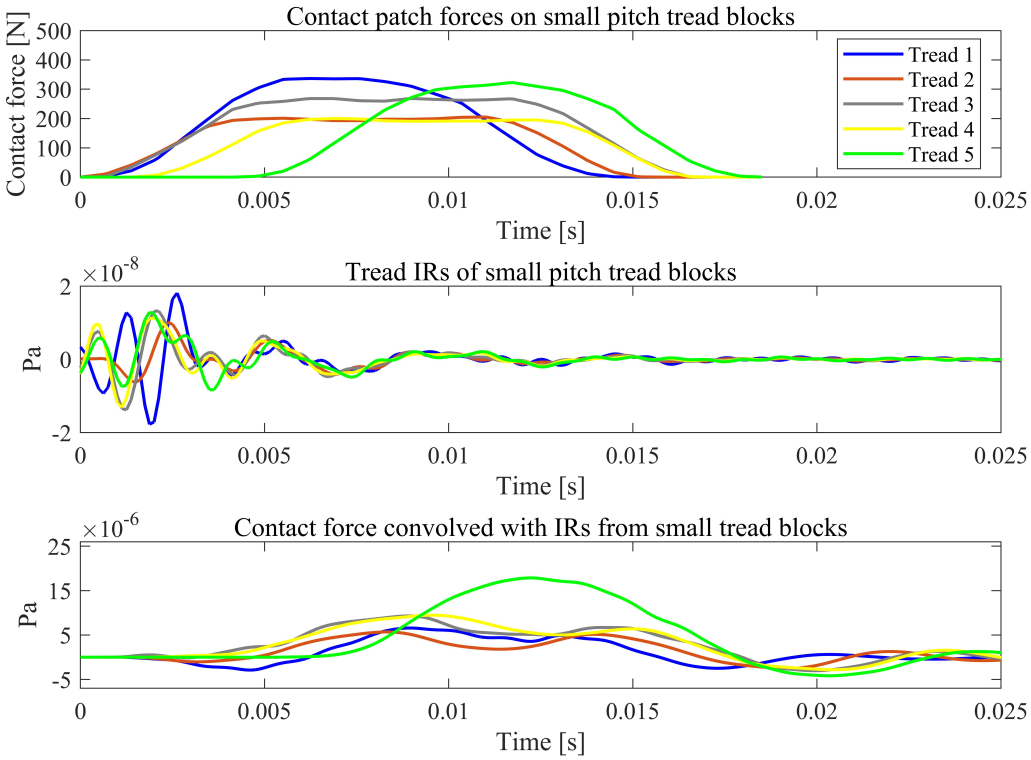

(a)

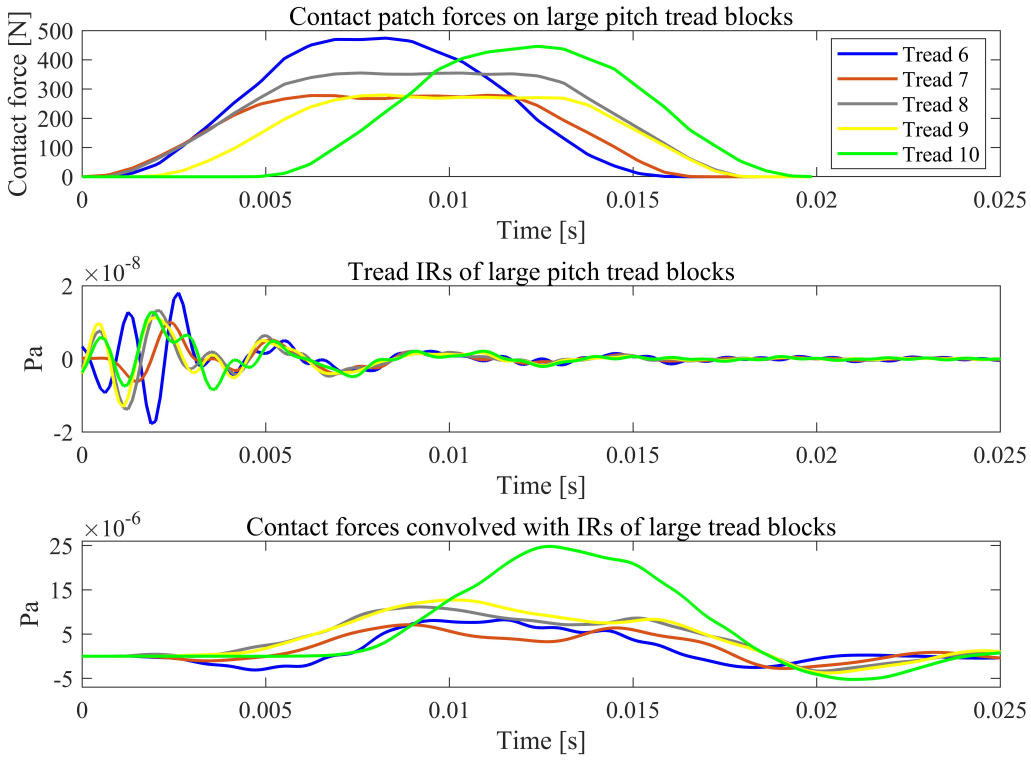

(b)

Figure B.3: Convolved response for (a) small pitch tread set and (b) large pitch tread set. Refer Figure 5.1b for various tread set pitch sizes.

Cette thèse est accessible à l'adresse : https://theses.insa-lyon.fr/publication/2022ISAL0081/these.pdf
© [B. Anantharamaiah], [2022], INSA Lyon, tous droits réservés

Table B.1: Considered tyre tread randomisation pattern as defined by the manufacturer. Pitch no. 1, 2 and 3 refers to small pitch tread block set, medium pitch tread block set and large pitch tread block set, respectively.

Tread set	1	2	3	4	5	6	7	8	9	10	11	12	13	14	15	16	17	18
Pitch no.	3	3	3	3	2	1	3	2	2	2	1	1	1	1	2	1	3	3
Tread set	19	20	21	22	23	24	25	26	27	28	29	30	31	32	33	34	35	36
Pitch no.	2	2	3	2	1	1	1	1	3	2	3	3	1	1	1	1	3	3
Tread set	37	38	39	40	41	42	43	44	45	46	47	48	49	50	51	52	53	54
Pitch no.	2	3	1	2	2	2	3	3	3	3	2	1	3	2	2	2	1	1
Tread set	55	56	57	58	59	60	61	62	63	64	65	66	67	68	69	70		
Pitch no.	1	1	2	1	3	3	2	2	3	2	1	2	3	2	1	1		

Refer Figure 5.1 for the pitch tread set information.

Cette thèse est accessible à l'adresse : https://theses.insa-lyon.fr/publication/2022ISAL0081/these.pdf
© [B. Anantharamaiah], [2022], INSA Lyon, tous droits réservés

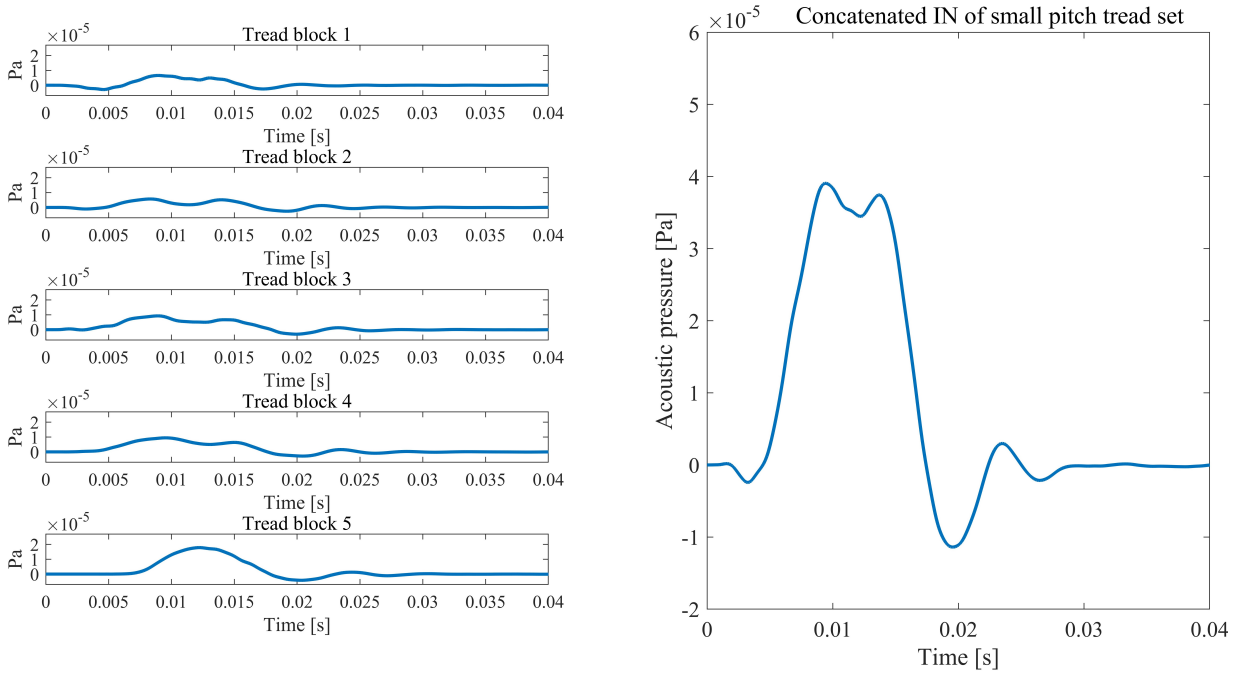

Figure B.4: Convolved IR for rubber blocks of small pitch tread set (left) and impact noise (IN) of the small pitch tread set as a result of concatenation of convolved IRs of individual rubber blocks of the same tread set (right).

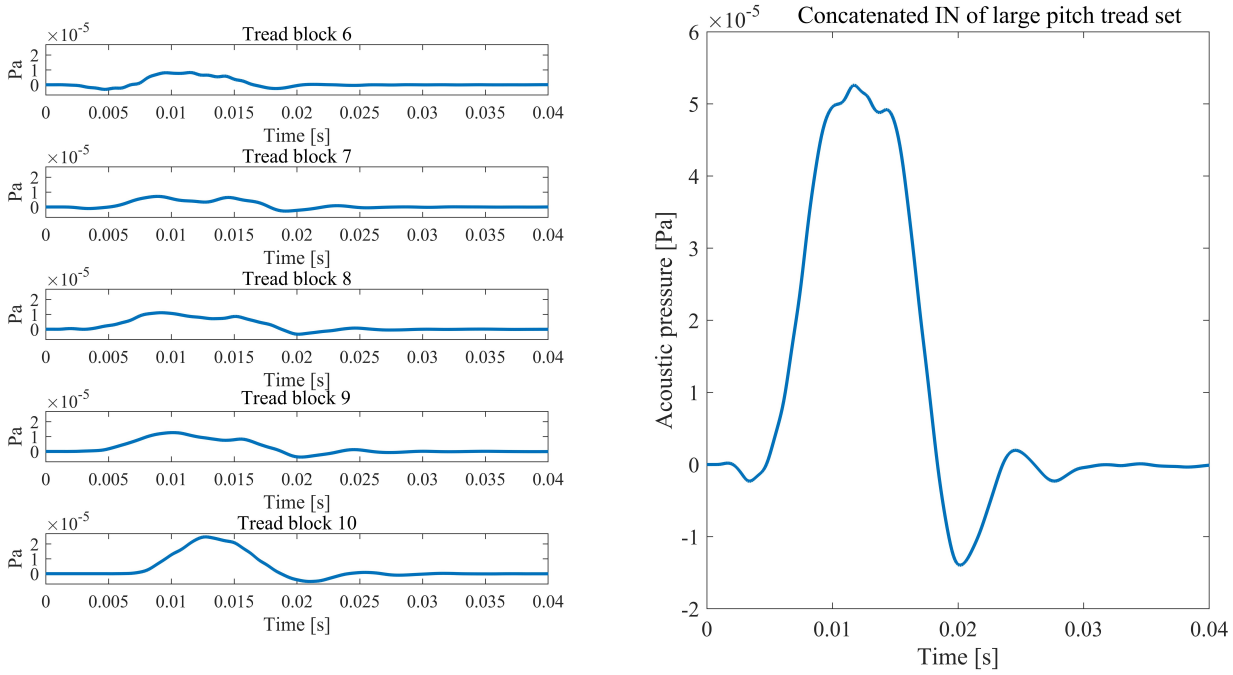

Figure B.5: Convolved IR for rubber blocks of large pitch tread set (left) and impact noise (IN) of the large pitch tread set as a result of concatenation of convolved IRs of individual rubber blocks of the same tread set (right).

Cette thèse est accessible à l'adresse : https://theses.insa-lyon.fr/publication/2022ISAL0081/these.pdf
© [B. Anantharamaiah], [2022], INSA Lyon, tous droits réservés

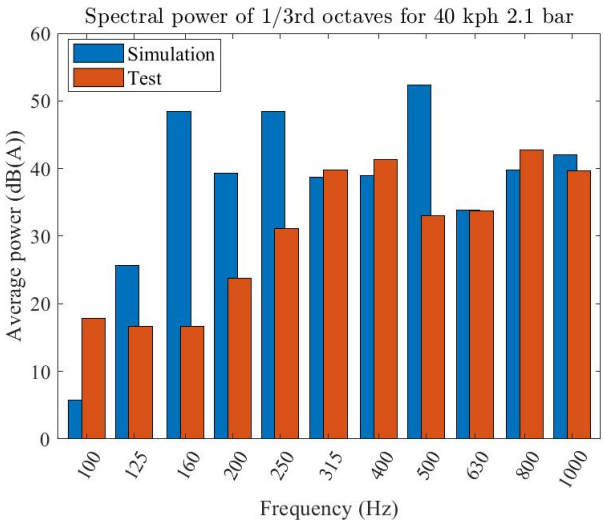

(a)

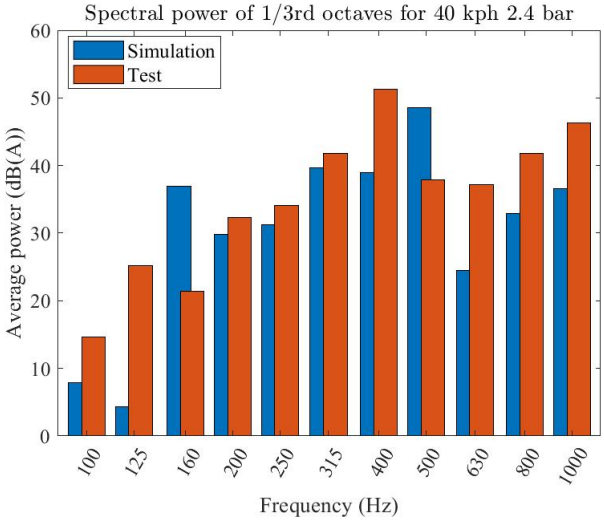

(b)

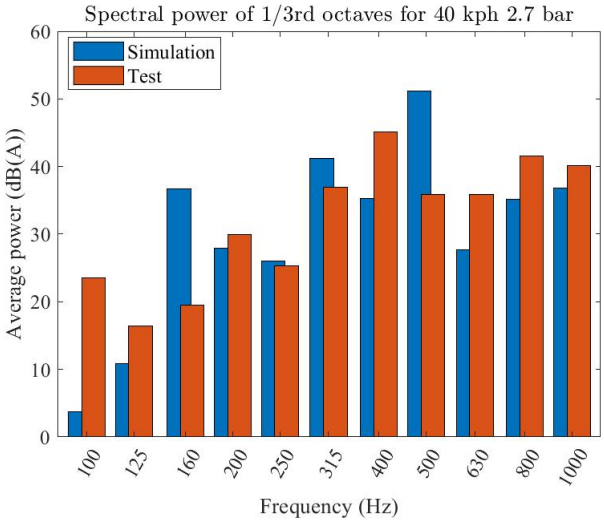

(c)

Figure B.6: Comparison of the average power of one-third octave bands between the synthesised and measured rolling noise for a tyre inflated at (a) 2.1 bar, (b) 2.4 bar and (c) 2.7 bar with a linear velocity of 40 kph. Vehicle load remains constant with 5000 N.

Cette thèse est accessible à l'adresse : https://theses.insa-lyon.fr/publication/2022ISAL0081/these.pdf
© [B. Anantharamaiah], [2022], INSA Lyon, tous droits réservés

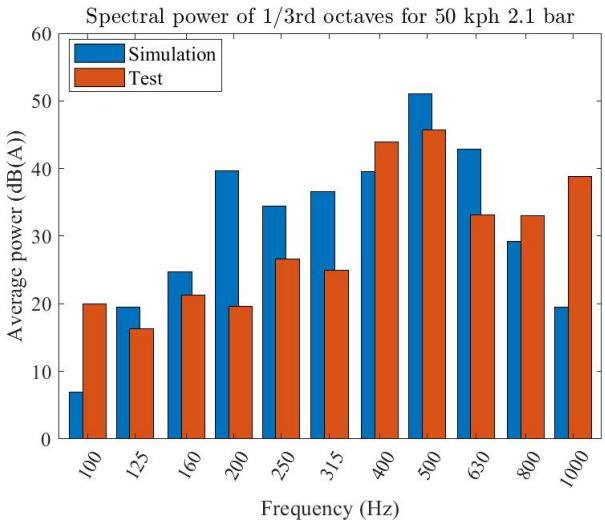

(a)

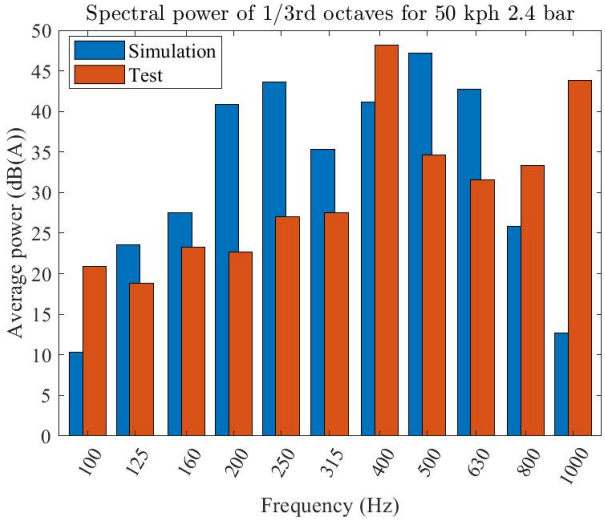

(b)

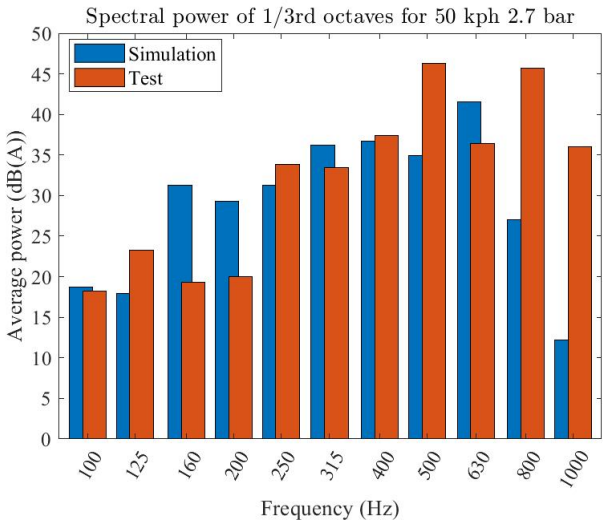

(c)

Figure B.7: Comparison of the average power of one-third octave bands between the synthesised and measured rolling noise for a tyre inflated at (a) 2.1 bar, (b) 2.4 bar and (c) 2.7 bar with a linear velocity of 50 kph. Vehicle load remains constant with 5000 N.

Cette thèse est accessible à l'adresse : https://theses.insa-lyon.fr/publication/2022ISAL0081/these.pdf
© [B. Anantharamaiah], [2022], INSA Lyon, tous droits réservés

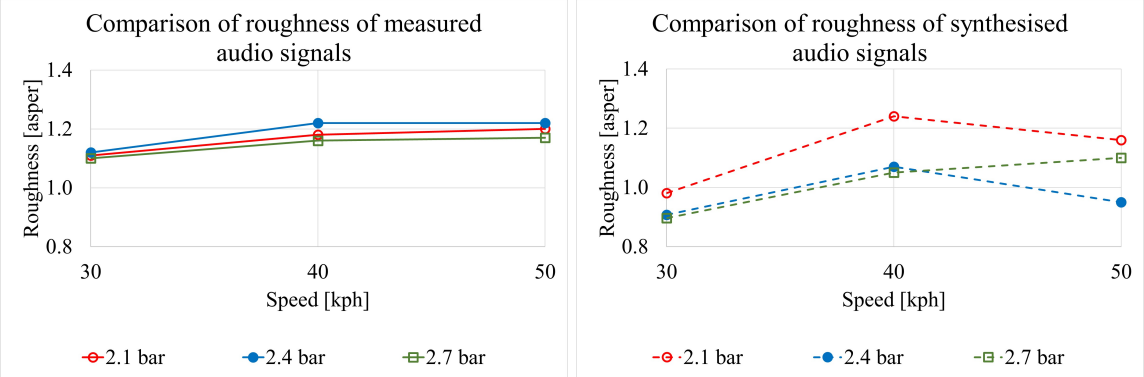

(a) (b)

Figure B.8: Comparison of roughness of (a) test and (b) synthesised audio files of rolling tyres.

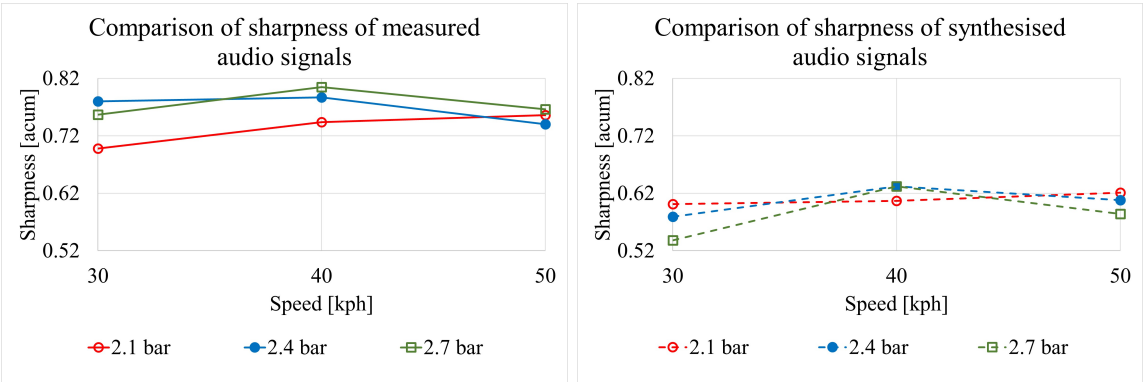

(a) (b)

Figure B.9: Comparison of sharpness of (a) test and (b) synthesised audio files of rolling tyres.

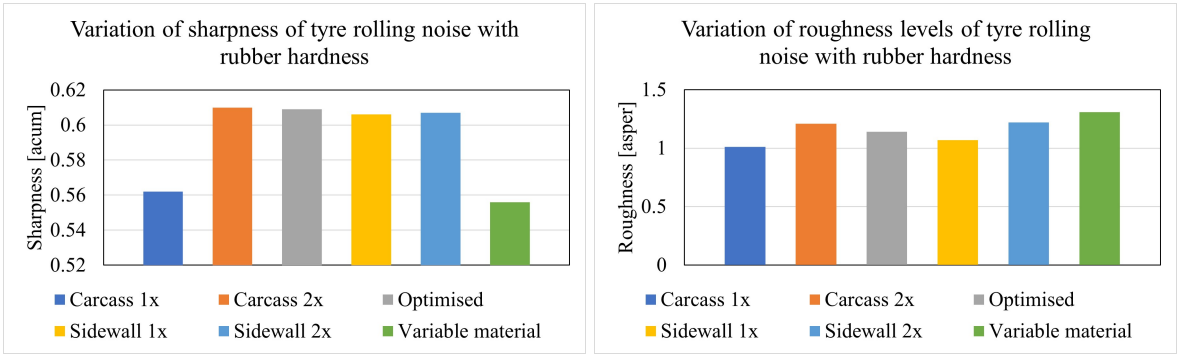

(a) (b)

Figure B.10: Comparison of (a) sharpness and (b) roughness in the audio files that are generated by varying tyre rubber properties as described in Section 5.4 (Figure 5.18).

Cette thèse est accessible à l'adresse : https://theses.insa-lyon.fr/publication/2022ISAL0081/these.pdf
© [B. Anantharamaiah], [2022], INSA Lyon, tous droits réservés

Cette thèse est accessible à l'adresse : https://theses.insa-lyon.fr/publication/2022ISAL0081/these.pdf
© [B. Anantharamaiah], [2022], INSA Lyon, tous droits réservés

FOLIO ADMINISTRATIF

THESE DE L'INSA LYON, MEMBRE DE L'UNIVERSITE DE LYON

NOM : ANANTHARAMAIAH — DATE de SOUTENANCE : 04/10/2022

Prénoms : Bharath

TITRE : Mr.

NATURE : Doctorat — Numéro d'ordre : 2022ISAL0081

Ecole doctorale : MEGA (Mécanique, Energétique, Génie Civil, Acoustique)

Spécialité : Acoustique

RESUME : Dans une automobile, le bruit est généré par divers composants tels que le moteur, la transmission, l'échappement, les pneus, l'aérodynamique, etc. Tous ces bruits contribuent collectivement au bruit de passage (PBN) et participent à la gêne sonore en milieu urbain.

Les véhicules électriques ont radicalement modifié la situation. Dans ces voitures, le bruit du moteur est presque inexistant. Le bruit aérodynamique étant très faible à basse vitesse (moins de 70 km/h), les pneus sont la principale source de désagrément en milieu urbain. Bien que plusieurs travaux aient été menés sur le bruit des pneus, il n'existe aucune étude déterministe sur sa conception efficace, en particulier sur sa perception acoustique en ce qui concerne son caractère désagréable.

Pour relever ce défi, l'objectif principal de ce travail est d'explorer les facteurs qui influencent le bruit généré par les pneus, en particulier son caractère désagréable, afin d'améliorer la perception acoustique d'une voiture à basse vitesse. Le principal résultat de ce travail est le développement d'un outil de simulation ou d'éléments finis (FE) qui permet de prédire le bruit généré par les pneus et la perception de son caractère désagréable. Cela permet de tirer parti du bruit des pneus pour améliorer la sécurité des piétons, en particulier lorsqu'il provient d'un véhicule qui passe à une vitesse relativement faible.

Le processus de développement du modèle FE du pneu présenté dans ce travail comprend la caractérisation du caoutchouc du pneu et des matériaux des couches. Ces propriétés sont utilisées dans les simulations pour modéliser le comportement statique et dynamique du pneu. Ces simulations permettent de déterminer les fonctions de transfert du bruit (NTF), et donc les réponses impulsionnelles (IR), dues à l'impact sur les bandes de roulement au niveau de l'aire de contact pneu/route. Les forces de roulement sur chaque bande de roulement d'un pneu roulant sont déterminées et convoluées avec les réponses impulsionnelles correspondantes. Celles-ci sont ensuite concaténées pour développer le bruit de roulement du pneu pour différentes pressions de gonflage et vitesses de roulement. Les densités spectrales de puissance des fichiers audio/bruit générés sont corrélées avec celles des tests. Enfin, les fichiers audios du bruit de roulement simulé et des tests sont soumis à des tests d'écoute pour évaluer leur caractère désagréable.

Les résultats ont confirmé la bonne fiabilité et sensibilité de l'outil FE développé dans ce travail pour le changement du caractère désagréable du bruit dû aux variations de la vitesse des pneus. Cependant, ils n'ont pas été concluants pour les différentes pressions de gonflage du pneu.

MOTS-CLÉS : bruit des pneumatiques, pass-by noise (PBN), psychoacoustique des bruits des pneumatiques, Simulation en éléments finis (FE) des bruits des pneumatiques, véhicules électriques (EVs).

Laboratoire (s) de recherche : Laboratoire Vibrations Acoustique (LVA) de l'INSA – Lyon

Directeur de thèse : PARIZET Etienne

Président de jury : TOTARO Nicolas

Composition du jury :

Garcia, Juan, Docteur, Applus IDIADA	Rapporteur
Lopez Arteaga, Ines, Professor, Eindhoven Univ. of Technology	Examinatrice
Kropp, Wolfgang, Professeur, Chalmers Univ. of Technology	Examinateur
Totaro, Nicolas, Professeur, INSA Lyon	Examinateur

Cette thèse est accessible à l'adresse : https://theses.insa-lyon.fr/publication/2022ISAL0081/these.pdf
© [B. Anantharamaiah], [2022], INSA Lyon, tous droits réservés